Static energy in (2 + 1 + 1)-flavor lattice QCD: Scale setting and charm effects

Nora Brambilla,[1,2,3,*] Rafael L. Delgado,[4,†] Andreas S. Kronfeld,[5,2,‡] Viljami Leino,[1,§] Peter Petreczky,[6,‖] Sebastian Steinbeißer,[1,7,¶] Antonio Vairo,[1,**] and Johannes H. Weber[1,8,††]

(TUMQCD Collaboration)

[1]*Physik Department, Technische Universität München, James-Franck-Straße 1, D-85748 Garching b. München, Germany*
[2]*Institute for Advanced Study, Technische Universität München, Lichtenbergstraße 2a, D-85748 Garching b. München, Germany*
[3]*Munich Data Science Institute, Technische Universität München, Walther-von-Dyck-Straße 10, D-85748 Garching b. München, Germany*
[4]*Universidad Politécnica de Madrid, Nikola Tesla, s/n, 28031-Madrid, Spain*
[5]*Particle Theory Department, Theory Division, Fermi National Accelerator Laboratory, Batavia, Illinois 60510-5011, USA*
[6]*Physics Department, Brookhaven National Laboratory, Upton, New York 11973-5000, USA*
[7]*Leibniz-Rechenzentrum der Bayerischen Akademie der Wissenschaften, Boltzmannstraße 1, D-85748 Garching b. München, Germany*
[8]*Institut für Physik and IRIS Adlershof, Humboldt-Universität zu Berlin, Zum Großen Windkanal 6, D-12489 Berlin, Germany*

(Received 9 June 2022; accepted 1 March 2023; published 11 April 2023)

We present results for the static energy in $(2+1+1)$-flavor QCD over a wide range of lattice spacings and several quark masses, including the physical quark mass, with ensembles of lattice-gauge-field configurations made available by the MILC Collaboration. We obtain results for the static energy out to distances of nearly 1 fm, allowing us to perform a simultaneous determination of the scales r_1 and r_0, as well as the string tension σ. For the smallest three lattice spacings we also determine the scale r_2. Our results for r_0/r_1 and $r_0\sqrt{\sigma}$ agree with published $(2+1)$-flavor results. However, our result for r_1/r_2 differs significantly from the value obtained in the $(2+1)$-flavor case, which is most likely due to the effect of the charm quark. We also report results for r_0, r_1, and r_2 in fm, with the former two being slightly lower than published $(2+1)$-flavor results. We study in detail the effect of the charm quark on the static energy by comparing our results on the finest two lattices with the previously published $(2+1)$-flavor QCD results at similar lattice spacing. We find that for $r > 0.2$ fm our results on the static energy agree with the $(2+1)$-flavor result, implying the decoupling of the charm quark for these distances. For smaller distances, on the other hand, we find that the effect of the dynamical charm quark is noticeable. The lattice results agree well with the two-loop perturbative expression of the static energy incorporating finite charm mass effects. This is the first time that the decoupling of the charm quark is observed and quantitatively analyzed on lattice data of the static energy.

DOI: 10.1103/PhysRevD.107.074503

*nora.brambilla@ph.tum.de
†rafael.delgado@upm.es
‡ask@fnal.gov
§viljami.leino@tum.de
‖petreczk@bnl.gov
¶sebastian.steinbeisser@tum.de
**antonio.vairo@ph.tum.de
††johannes.weber@physik.hu-berlin.de

I. INTRODUCTION

The energy of a static quark-antiquark pair separated by a distance r, $E_0(r)$ has played an important role in QCD since early days [1]. Nonperturbative calculations with lattice gauge theory [2] were important in establishing confinement in QCD and in understanding its interplay with asymptotic freedom. Confinement manifests itself in the linear rise of $E_0(r)$ at large r; the corresponding slope is known as the string tension. In the literature, $E_0(r)$ is sometimes also called the static potential. The term "static energy" is, however, preferable because in the context of

nonrelativistic effective field theories of QCD the term "static potential" is understood to be the contribution to $E_0(r)$ coming solely from soft gluons, i.e., gluons of energy or momentum of order $1/r$. The static potential is infrared divergent [3]. Up to a constant shift, the energy is a physical quantity not affected by infrared divergences. In particular, the infrared divergence of the static potential cancels in the static energy against an ultraviolet divergence coming from ultrasoft gluons, i.e., gluons of energy and momentum of order α_s/r [4,5].

In lattice QCD, the static energy plays also an important role in setting the lattice scale, i.e., in the conversion from lattice to physical units. In quenched lattice QCD calculations, the scale has been set using the string tension, but in full QCD the string breaks at the pair-production threshold, making a precise definition difficult. Instead of the static energy, one can also use the force

$$F(r) \equiv \frac{\mathrm{d}E_0(r)}{\mathrm{d}r}, \tag{1.1}$$

which is easier to manage in dimensional regularization as it is free of the order Λ_{QCD} renormalon [6–8] and in lattice gauge theory because it is free of the self-energy linear divergence. The dimensionless product $r^2F(r)$ can be used to set the scale [9], especially at distances where statistical and systematic uncertainties are under good control. Examples of such a scale setting are the scales r_0, r_1, and r_2 defined by

$$r_i^2 F(r_i) = c_i, \quad i = 0, 1, 2, \tag{1.2}$$

with $c_0 = 1.65$ [9], $c_1 = 1$ [10], and $c_2 = 1/2$ [11].

The static energy has been extensively studied in QCD with two light quarks and a (physical) strange quark, referred to as $(2+1)$-flavor QCD [10–17], and the scales r_0 and r_1 have been determined for a wide range of lattice spacing. The study of the static energy in $(2+1+1)$-flavor QCD, i.e., in QCD with two light quarks, a (physical) strange quark, and a (physical) charm quark, is less established. The MILC Collaboration [18,19] calculated the static energy in a narrow region of distances and obtained the r_1 scale using the highly improved staggered quark (HISQ) action [20] for sea quarks and one-loop tadpole-improved Symanzik gauge action [21–24]. In MILC's work, four lattice spacings were used, $a \approx 0.06$, 0.09, 0.12, and 0.15 fm, and the three light quark masses, $m_l = m_s/27$, $m_s/10$, and $m_s/5$, the first corresponding to the physical light quark mass. Here, m_s is the physical strange quark mass. The ETM Collaboration studied the static energy using the twisted-mass formulation in the quark sector and tree-level Symanzik gauge action [25]. The calculations were performed at three lattice spacings, $a \approx 0.065$, 0.082, and 0.089 fm, and several values of the light quark masses corresponding to pion mass in the range 210–450 MeV [25]. In that work, the static energy was calculated in a narrow distance range around $r \sim r_0$ and the scale r_0 was determined.

In this paper, our aim is to extend the studies of the static energy in $(2+1+1)$-flavor QCD to smaller lattice spacing, namely $a \approx 0.032$ fm and 0.043 fm, and a large range of distances on MILC's $(2+1+1)$-flavor HISQ ensembles. We perform a simultaneous determination of the scales r_0/a, r_1/a and the string tension on 11–12 ensembles. We proceed to take the continuum limit of these scales and the combinations r_0/r_1 and $\sqrt{\sigma r_0^2}$. In addition, we also determine the scale r_2/a and the ratio r_1/r_2 on the six ensembles at the three smallest lattice spacings. Finally, we determine the continuum limits in fm of r_0, r_1, and r_2 as well.

The $(2+1+1)$-flavor HISQ ensembles are described in Refs. [18,19,26]. Taken together these ensembles have yielded impressive results for a wide range of observables. The observables cover spectroscopy [27–32], the decay constant ratio f_{K^+}/f_{π^+} [33,34], the B-, D-, and J/ψ-meson decay constants [26,35–39], quark condensates [40], the hadronic vacuum polarization for the anomalous magnetic moment of the muon [41–44], quark masses and α_s [45–47], the hindered M1 transition $\Upsilon(2S) \to \eta_b(1S)\gamma$ [48], the electromagnetic form factor of the pion [49,50], the Cabibbo–Kobayashi–Maskawa (CKM) element $|V_{us}|$ from $K \to \pi l \nu$ [51,52], $B_s \to D_s^{(*)}$ form factors [53–55], neutral $B^0_{d,s}$ mixing matrix elements [56,57], and $B_c \to B_{d,s}$, J/ψ form factors [58,59]. Significant, though less extensive work has been carried out on ensembles with $(2+1+1)$-flavor of twisted-mass Wilson fermions [60–62], for example, quark masses [25].

The static energy is also an important way to determine the strong coupling α_s or, equivalently, $\Lambda_{\overline{\mathrm{MS}}}$; see Ref. [63] for a recent review. Such studies started with quenched QCD [64–66]. Thereafter, the static energy in $(2+1)$-flavor QCD has been used to determine α_s in several lattice setups [17,67–70]. These works have showed that perturbative QCD describes well the lattice results up to distances $r \approx 0.15$–0.2 fm. These distances include the inverse charm quark mass, so the charm quark can neither be considered massless nor infinitely heavy. It is important to account for finite charm quark mass effects when analyzing the static energy in $(2+1+1)$-flavor QCD, particularly when determining α_s. In this paper, we show the impact of finite charm quark mass effects on the static energy by comparing our new lattice QCD results for the static energy in $(2+1+1)$-flavor QCD with published results in $(2+1)$-flavor QCD at similar lattice spacings. The comparison also demonstrates for the first time how the charm quark decouples from the static energy when going from short to large distances.[1]

[1]Decoupling of $N_f = 2$ charmlike heavy quarks at very large distances has already been observed for the force and was published in conference proceedings [71]. Decoupling of heavy quarks in a similar setup has been proposed as a scheme for determining α_s [63,72].

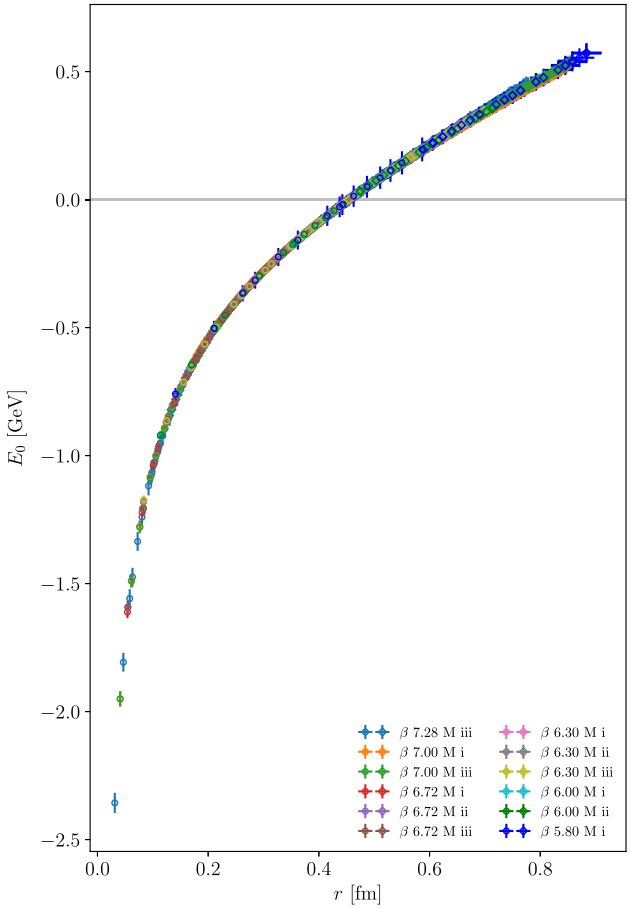

FIG. 1. Results for the static energy in physical units from the calculations described in this paper. The data are from twelve ensembles of varying lattice spacing (keyed by β) and three choices of light quark mass (denoted "M i," "M ii," "M iii"). Lattice units are eliminated via r_0/a, and the unphysical constant is eliminated by setting $E_0(r_0) = 0$. See Sec. IV C for details.

Further, we compare the $(2+1+1)$-flavor lattice data with the two-loop expression of the static energy, including charm mass effects.

The rest of the paper is organized as follows. Our numerical calculation of the static energy on the HISQ ensembles is described in Sec. II. We then take these results and analyze them in Sec. III to obtain the scales r_i/a and string tension $a^2\sigma$. Section IV forms several universal ratios or products of these quantities among each other and combined with $a_{f_{p4s}}$ (the lattice spacing defined via the decay constant of a fictitious meson with quark and antiquark having mass $0.4m_s$) from Ref. [26]. We then turn in Sec. V to the comparison of the static energy with perturbation theory, in particular, studying the effect of the massive charm quark sea. Section VI offers some outlook and conclusions. Several technical appendices follow. We found some inconsistencies in the gauge fixing of the publicly available and widely used HISQ ensembles, which we document in Appendix A. Additional plots and tables in support of Secs. II–IV can be found in Appendix B. Formulas from perturbative QCD needed for our study of charm quark loops are collected in Appendix C. Preliminary results based on these data have been published in conference proceedings [73]; we have refined that analysis to permit quantitative studies of the impact on the various uncertainties.

To conclude this introduction, Fig. 1 shows the $(2+1+1)$-flavor QCD static energy obtained from our calculations for all ensembles in this work. As detailed below, we compute the static energy with both "bare" and "smeared" links, and in the figure we show only the bare (smeared) data for $r/a \leq 4$ ($r/a > 4$). (For details, see Sec. II). On the scale of Fig. 1, it is possible to see light quark mass dependence only at the larger r, but it is very difficult to spot lattice-spacing dependence. The data are, however, precise enough for both to be (statistically) significant, requiring the painstaking analysis of the rest of the paper. Figure 1 demonstrates for the first time the progression of the static energy in $(2+1+1)$-flavor QCD from the Coulombic to the confining region.

II. SIMULATIONS

In this section we give an overview of the simulation details, i.e., the gauge and fermion action, and further ensemble details. After that, we describe the operators used and how we extract the static energy, i.e., the ground state of the underlying correlation function.

A. HISQ ensembles and lattice setup

We employ ensembles of lattice gauge fields with $(2+1+1)$-flavors of sea quark, generated by the MILC Collaboration [18,19,26]. The subset used in this paper is listed in Table I.[2] The sea quarks, namely two isospin-symmetric light quarks and physical strange and charm quarks, are simulated with the (rooted) determinant of the HISQ action [20]. In most figures, we denote the ensembles by their respective β values and their light quark mass labeled with roman numerals i, ii, or iii, indicating m_l/m_s at the physical value $1/10$ or $1/5$, respectively. The gluon action is the on-shell Symanzik-improved action [21,22] with the couplings determined at the one-loop level [23,24] with tadpole improvement [75]. Thus, the gluon action has leading discretization effects of order $\alpha_s^2 a^2$ and a^4. The sea quark action eliminates discretization effects of order $\alpha_s^0 a^2$, as well as those from staggered taste-symmetry violation of

[2]While the β `7.00 M i,iii` or β `7.28 M iii` ensembles are affected by insufficient sampling of topological sectors, this does not lead to statistically significant effects for heavy-light mesons [26]. There are indications in $(2+1)$-flavor QCD that insufficient sampling of topological sectors does not affect the static energy at a statistically significant level either [74]. Hence, we have disregarded quantitative effects of topological freezing in our calculations.

TABLE I. MILC gauge ensembles used in this study. The ensembles in the four upper rows have successive configurations separated by 5 time units (TU); the other ensembles use a separation of 6 TU.[a]

Our naming	$N_\sigma^3 \times N_\tau$	β	$a_{f_{p4s}}$ (fm) [26]	u_0 [78]	am_l	am_s	am_c	m_l/m_s	$(am_s)_{\text{tuned}}$ [26]	M_π (MeV) [26]	N_{conf} [26]
β 5.80 M i	$32^3 \times 48$	5.80	0.15294	0.85535	0.00235	0.0647	0.831	Physical	0.06852	131	1041
β 6.00 M ii	$32^3 \times 64$	6.00	0.12224	0.86372	0.00507	0.0507	0.628	1/10	0.05296	217	1000
β 6.00 M i	$48^3 \times 64$				0.00184			Physical		132	709
β 6.30 M iii	$32^3 \times 96$				0.0074	0.037	0.44	1/5		316	1008
β 6.30 M ii	$48^3 \times 96$	6.30	0.08786	0.874164	0.00363	0.0363	0.43	1/10	0.03627	221	1031
β 6.30 M i	$64^3 \times 96$				0.0012		0.432	Physical		129	1074
β 6.72 M iii	$48^3 \times 144$				0.0048	0.024	0.286	1/5		329	1017
β 6.72 M ii	$64^3 \times 144$	6.72	0.05662	0.885773	0.0024			1/10	0.02176	234	1103
β 6.72 M i	$96^3 \times 192$				0.0008	0.022	0.26	Physical		135	1268
β 7.00 M iii	$64^3 \times 192$	7.00	0.0426	0.892186	0.00316	0.0158	0.188	1/5	0.01564	315	1165
β 7.00 M i	$144^3 \times 288$				0.000569	0.01555	0.1827	Physical		134	478
β 7.28 M iii	$96^3 \times 288$	7.28	0.03216	0.89779	0.00223	0.01115	0.1316	1/5	0.01129	309	821

[a]There are two exceptions from this rule, one stream of β 6.30 M i with a separation of 4 TU and one stream of β 6.72 M i with a separation of 8 TU.

order $\alpha_s^1 a^2$, but does not realize full $O(\alpha_s a^2)$ improvement. In short-distance quantities, the sea quarks contribute in loops, so the quark-action discretization artifacts in the static energy are of order $\alpha_s^2 a^2$ and $\alpha_s a^4$. The three-link improvement term for the charm quark is adjusted to eliminate higher-dimension discretization effects with powers of $(am_c)^2$ at the tree level. In the characterization of these ensembles, we use the lattice scale $a_{f_{p4s}}$, which was introduced in [19] as an extension of the f_{ps} scale [76], determined via the decay constant of a pseudoscalar meson made up from two quarks at the mass of $0.4m_s$ [19,77], which is a compromise between good chiral behavior and only modest staggered taste-symmetry violation.

For reference, we also employ $(2+1)$-flavor ensembles from the HotQCD Collaboration [11,16], again with the (rooted) HISQ determinant for the sea quarks but now with a *tree*-level Symanzik-improved gauge action. These ensembles correspond to continuum pion masses of $M_\pi \approx$ 160 or 320 MeV, respectively, while the strange quark is physical; in their characterization we use the lattice scale a_{r_1} determined from the static energy [10], which had been obtained through, e.g., continuum extrapolation of r_0/r_1 [12], or chiral-continuum extrapolation of Υ-splittings [76], or of $r_1 f_\pi$ [77]. Since r_1 is derived from a gluonic operator, it is rather insensitive to the light quark masses in the sea or to staggered taste-symmetry violation; our analysis confirms this well-known fact, see Sec. III C.

The gauge configurations have been fixed to Coulomb gauge. Due to miscommunication, we accidentally employed two different schemes, fixed tolerance and fixed iteration count. Subsets of the β 6.72 M i ensemble had each in turn; for details, see Appendix A. As a consequence, we analyzed the two subsets with different gauge-fixing schemes separately and confirmed the independence of the energy levels; see Figs. 22 and 23 in Appendix A. In the further analysis, we restricted ourselves to the subset with the fixed-tolerance scheme due to having better statistics.

B. Correlation functions and fitting

The static energy is obtained from the time dependence of the Wilson-line correlation function $C(\boldsymbol{r},\tau,a)$ at separation $\boldsymbol{r}/a \in \mathbb{Z}^3$ computed after fixing to a Coulomb gauge (see Sec. II A):

$$W(\boldsymbol{r},\tau,a) = \prod_{u=0}^{\tau/a-1} U_4(\boldsymbol{r},ua,a), \tag{2.1}$$

$$C(\boldsymbol{r},\tau,a) = \left\langle \frac{1}{N_\sigma^3} \sum_{\boldsymbol{x}} \sum_{\boldsymbol{y}=R(\boldsymbol{r})} \frac{1}{N_c N_{\boldsymbol{r}}} \mathrm{tr}[W^\dagger(\boldsymbol{x}+\boldsymbol{y},\tau,a) W(\boldsymbol{x},\tau,a)] \right\rangle, \tag{2.2}$$

$$= \sum_{n=0}^{\infty} C_n(\boldsymbol{r},a)\left(\mathrm{e}^{-\tau E_n(\boldsymbol{r},a)} + \mathrm{e}^{-(aN_\tau-\tau)E_n(\boldsymbol{r},a)}\right), \tag{2.3}$$

where, on the first line, U_4 is a temporal link. On the second line, one sum is over all spatial sites $\boldsymbol{x}$ with N_σ the isotropic spatial extent of the lattice in each direction, and $\langle\ldots\rangle$ denotes the average over all dynamical quark and gauge field configurations. The other sum is over all distances $\boldsymbol{y}$ that are either a cubic rotation reflection of $\boldsymbol{r}$, or that correspond to the same geometric distance $|\boldsymbol{r}|$ with large

TABLE II. Time and distance intervals in the full data set. The minimum distance is always (1,0,0).

$a_{f_{p4s}}$ (fm)	β	$T_{\min}/a$	$T_{\max}/a$	$T_{\max}$ (fm)	$r_{\max}/a$	$r_{\max}$ (fm)
0.15294	5.8	1	9	1.35	6	0.92
0.12224	6.0	1	6	0.73	6	0.73
0.08786	6.3	1	8	0.70	8	0.70
0.05662	6.72	1	10	0.57	12	0.68
0.0426	7.0	1	20	0.85	20	0.85
0.03216	7.28	1	28	0.91	24	0.78

enough $|\boldsymbol{r}|/a^3$; $N_{\boldsymbol{r}}$ is the total number of distances included in this sum. On the same line, $N_c = 3$ is the number of colors. Finally, on the last line, N_τ is the temporal extent of the lattice, and this spectral decomposition holds—with improved gauge action—only for $\tau/a \geq 2$. Because, in our notation, τ/a are dimensionless integers, fits to the τ/a dependence yield dimensionless energies aE_n. For each ensemble, we have also constructed a Wilson-line correlation function replacing the bare links U_4 with links after one iteration of four-dimensional hypercubic (HYP) smearing [79] with standard smearing parameters ($\alpha_1 = 0.75$, $\alpha_2 = 0.6$, $\alpha_3 = 0.3$). Smearing improves greatly the signal-to-noise ratio even at large distances, as discussed in Secs. III A and III C, but the exponents in Eq. (2.3) can be interpreted as static energies only when at least one component of $\boldsymbol{r}/a$ is greater than 2.

In this work, we are interested only in the lowest-lying state, namely $aE_0(\boldsymbol{r}, a)$. We want to combine data for a huge range of $\boldsymbol{r}$ from $\boldsymbol{r}/a = (1, 0, 0)$ out to $|\boldsymbol{r}| \approx 1$ fm and from a wide range of lattice spacing a from 0.03 fm up to 0.15 fm. The former (short distances, fine lattices) are indispensable for the comparison to weak-coupling calculations in Sec. V, while the latter (large distances, coarser lattices) are indispensable for a determination of some lattice scales and the string tension in Sec. III. The data written to disk are limited to within a sphere $|\boldsymbol{r}| \leq R_{\max}$ and to a maximum time $\tau \leq T_{\max}$, which are collected in Table II. In particular, our data are restricted to distances smaller than those where string breaking occurs.[4]

Because of the limited time range, and because of the exponential degradation of the signal-to-noise ratio,[5] we can safely neglect the backwards-propagating states in Eq. (2.3) and are, in practice, limited to extractions of the ground state energy from multiexponential fits with a finite number of states. We reparametrize $C(\boldsymbol{r}, \tau, a)$ using energy differences $a\Delta_n(\boldsymbol{r}, a) = aE_n(\boldsymbol{r}, a) - aE_{(n-1)}(\boldsymbol{r}, a) > 0$, $n \geq 1$ instead of the equivalent[6] full excited state energies $aE_n(\boldsymbol{r}, a)$, $n \geq 1$,

$$C(\boldsymbol{r},\tau,a) = \mathrm{e}^{-\tau E_0(\boldsymbol{r},a)}\left(C_0(\boldsymbol{r},a) + \sum_{n=1}^{N_{\mathrm{st}}-1} C_n(\boldsymbol{r},a)\prod_{m=1}^{n}\mathrm{e}^{-\tau\Delta_m(\boldsymbol{r},a)}\right) + \ldots, \tag{2.4}$$

and choose $N_{\mathrm{st}} = 1$, 2, or 3, such that the highest state is labeled by $(N_{\mathrm{st}} - 1)$. The spectrum depends strongly on $|\boldsymbol{r}|$, so the time interval $\tau \in [\tau_{\min}, \tau_{\max}]$ in the fit must be chosen to depend on $|\boldsymbol{r}|$. Whereas, the ground state energy is essentially an attractive Coulomb interaction for small $\boldsymbol{r}$, the low-lying excited states correspond to a repulsive Coulomb interaction instead. At larger distances, all energy levels are controlled by the QCD string tension, with much smaller energy differences of order Λ_{QCD}. Hence, as the excited states survive longer at larger $\boldsymbol{r}$, we choose standard values of $\tau_{\min}$ for each N_{st}, depending on the distance $|\boldsymbol{r}|$, i.e.,

$$\begin{aligned} &|\boldsymbol{r}| + 0.2\ \mathrm{fm} \leq \tau_{\min,1} \leq 0.3\ \mathrm{fm} \quad \text{for } N_{\mathrm{st}} = 1, \\ &\frac{2}{3}|\boldsymbol{r}| + 0.1\ \mathrm{fm} \leq \tau_{\min,2} \leq \tau_{\min,1} - 2a \quad \text{for } N_{\mathrm{st}} = 2, \\ &\frac{1}{3}|\boldsymbol{r}| \leq \tau_{\min,3} \leq \tau_{\min,2} - 2a \quad \text{for } N_{\mathrm{st}} = 3, \end{aligned} \tag{2.5}$$

and round it to the next larger integer multiple of the lattice spacing $a_{f_{p4s}}$. Since we cannot always follow these criteria, we amend the fit ranges as necessary. The two main reasons for doing so are the limited number of available data due to finite $T_{\max}/a$ (see Table II) and the inability to constrain the two extra parameters for each further state, if less than two data could be added. We test the robustness of the fits by varying $\tau_{\min}/a$ by ± 1 wherever possible. Occasionally, the reduction by -1 sets $\tau_{\min}/a = 1$, which with the Symanzik-improved action is marred by a contact term, so we do not use such fits further. Hence, we arrive at a two-dimensional table, labeled by $(\tau_{\min}/a, N_{\mathrm{st}})$, of results $\{C_n, E_n\}$ for each $(\boldsymbol{r}, a)$. A complete account of the time ranges is given in Table III in Appendix B 1.

For a few representative pairs of $(\boldsymbol{r}, \tau)$, we find autocorrelation times of $C(\boldsymbol{r}, \tau, a)$ in the range of 1 or 2 separations of successive configurations on the β `7.00 M i` ensemble, which is the worst case due to the interplay of small ensemble size, fine lattice spacing, and physical light-quark mass, see Table I. Hence, in this case a block

[3]For paths of length $|\boldsymbol{r}|/a > 6$ that are inequivalent under the hypercubic group, we average over the path-dependent correlation function and neglect nonsmooth discretization artifacts; see Sec. III A.

[4]Since Wilson-line correlators in Eq. (2.2) do not overlap with two static-light mesons, our correlators are expected to be insensitive to string breaking.

[5]This degradation is much alleviated in correlation functions obtained with smeared links since the ultraviolet noise, due to short-distance fluctuations, is diminished and since the divergent contribution to static energy is decreased dramatically.

[6]We denote the collective set of fit parameters as $\{C_n, E_n\}$, $n \geq 0$, even though it means, in practice, $\{C_0, \{C_n\}, E_0, \{\Delta_n\}\}$, $n \geq 1$, which contains the same information.

size of $2\tau_{\rm int} \approx 4$ is justifiable, which permits up to 100 blocks. Autocorrelation times on other ensembles are, if anything, smaller than this. Hence, we assemble for each ensemble $N_J = 100$ jackknife pseudoensembles of the correlation function data for each $(\boldsymbol{r}, \tau)$. From these $N_J = 100$ jackknife pseudoensembles, we estimate the correlation matrix, which obviously has nonzero off-diagonal entries in both directions of the $(\boldsymbol{r}, \tau)$ space. The available data span an $(\boldsymbol{r}, \tau)$-space of $\mathrm{O}(10^2)$ to $\mathrm{O}(10^4)$ points. While proximity in the τ-direction certainly provides a hint on the actual strength of the correlations, such a naive expectation is not justified at all towards proximity in $|\boldsymbol{r}|$. Given $N_J = 100$ jackknife pseudoensembles, we may expect to be able to obtain good estimates for $\sqrt{N_J} = 10$ eigenvalues. In order to avoid or reduce eigenvalue smoothing[7] as much as possible, we have to slice the data and reduce them to a subset of about $\sqrt{N_J} = 10$ points in $(\boldsymbol{r}, \tau)$-space and estimate the correlation matrix for that subset. In order to propagate the statistical correlations of the correlation function into the analysis of $\boldsymbol{r}$-dependence of the static energy $E_0(\boldsymbol{r}, a)$, we repeat the analysis on the original sample and on all $N_J = 100$ jackknife pseudoensembles.

In the correlation function fits discussed in this section, we slice $(\boldsymbol{r}, \tau)$-space in the $\boldsymbol{r}$ direction, i.e., we consider the correlation matrix only between data at different τ for the same $\boldsymbol{r}$. If the correlated fit[8] (on the original sample) does not converge, then we thin out the set of τ values—potentially going down to zero degrees of freedom—by iteratively eliminating one datum in a randomized manner (keeping at least two data in each of the first $2/3$ and last $1/3$ of the fit interval) and repeating the fit attempt. If we include $N_D \leq \sqrt{N_J} = 10$ data, we do not smooth eigenvalues of the correlation matrix. Otherwise, if we include $N_D > 2\sqrt{N_J} = 20$ data, we smooth the $N_D - \sqrt{N_J}$ lowest eigenvalues; or else, we apply smoothing to the $N_D/2$ lowest eigenvalues. In some cases we have one large and copiously many very small eigenvalues[9] leading to a condition number of $\mathrm{O}(10^6)$ even after the smoothing; correlated fits for these cases could only succeed by means of the randomized thinning out of the fit interval. We also perform uncorrelated fits by neglecting the off-diagonal elements of the correlation matrix, which never require the randomized thinning out of the fit interval, and thus provide additional cross-checks on the results. Below, in the study of the $\boldsymbol{r}$ dependence, τ is not a variable anymore, and we consider the correlation matrix between data at different $|\boldsymbol{r}|/a$; see Sec. III B.

[7]We follow standard procedures [80] with adaptations spelled out in the text.

[8]We use R statistical package [81] with the NLME library [82] for these fits.

[9]Such cases occur typically at small $\boldsymbol{r}/a$ and even more so with smeared links. As some of these fits failed altogether, we have missing entries in the $(\tau_{\rm min}/a, N_{\rm st})$-table of results for some $aE_0(\boldsymbol{r}, a)$.

For $0 < n \leq N_{\rm st}$, we use Bayesian priors for $C_n(\boldsymbol{r}, a)$, $aE_0(\boldsymbol{r}, a)$, and $a\Delta_n(\boldsymbol{r}, a)$. The prior distributions in $\chi^2_{\rm prior}(\{C_n, aE_n\})$ are of Gaussian form for each parameter, i.e.,

$$\chi^2_{\rm prior}(\{C_n, aE_n\}) = \frac{(aE_0 - a\tilde{E}_0)^2}{\sigma^2_{a\tilde{E}_0}} + \sum_{n=0}^{N_{\rm st}-1} \frac{(C_n - \tilde{C}_n)^2}{\sigma^2_{\tilde{C}_n}} + \sum_{n=1}^{N_{\rm st}-1} \frac{[a\Delta_n - a\tilde{\Delta}_n]^2}{\sigma^2_{a\tilde{\Delta}_n}}, \tag{2.6}$$

where the reasoning behind central values and width is spelled out in detail in the following. Since we are interested only in the ground state energy, $aE_0(\boldsymbol{r}, a)$, we marginalize over the parameters related to the excited states; therefore, priors may be chosen to aid the stability of the fits, particularly during resampling. To set the prior central values and widths for fits with $N_{\rm st} = 1$, we automate procedures based on the effective mass and scaled correlator. Automation is necessary because of the large (1000 s) of Wilson-line correlators in this work.

In practice, we use the results of the $N_{\rm st} = 1$ fits as the starting guess for the $N_{\rm st} = 2$ fits and similarly for the $N_{\rm st} = 3$ fits. On each resample we follow the exact same procedure that was used on the mean to choose the Bayesian priors to determine starting values for the fit parameters.

For fits with $N_{\rm st} > 1$, the choice of priors faces several challenges. Since the values of the overlap factors $C_n(\boldsymbol{r}, a)$ change by an order of magnitude across the available $\boldsymbol{r}$ range, we cannot use a simple functional form that works over a wide $\boldsymbol{r}$ range. A further challenge is the decrease of the ground state overlap factor $C_0(\boldsymbol{r}, a)$ and the increase of the ground state energy $aE_0(\boldsymbol{r}, a)$ for larger $|\boldsymbol{r}|$, which gets compounded with an increase of the excited state overlap factors $C_n(\boldsymbol{r}, a)$ and the decrease of the excited state energy differences $a\Delta_n(\boldsymbol{r}, a)$. These features require the priors to become narrower for larger $|\boldsymbol{r}|$. Further, we require priors on the ground state parameters to avoid an outcome where the parameter $C_0(\boldsymbol{r}, a)$ approaches zero with poorly constrained $aE_0(\boldsymbol{r}, a)$, while $aE_1(\boldsymbol{r}, a)$ approaches the true ground state energy. Thus, we use multiple stages of simpler fits for each $\boldsymbol{r}$ to gain information for use as prior knowledge in fits with larger $N_{\rm st}$. We ensure for all ground state parameters, i.e., $(aE_0(\boldsymbol{r}, a), C_0(\boldsymbol{r}, a))$, loose priors with a width of at least 10%, which is orders of magnitude wider than the respective statistical uncertainties. For the excited state energy differences $(a\Delta_1(\boldsymbol{r}, a), a\Delta_2(\boldsymbol{r}, a))$, we use loose priors with widths of 10% or more. Lastly, for the excited state overlap factors $(C_1(\boldsymbol{r}, a), C_2(\boldsymbol{r}, a))$, we determine very loose priors in terms of small positive values with widths of at least 100%. Due to their large widths, the individual priors do not rely on unacceptable examination

of the data and could be modified without significant changes of the fit results.

In more detail, our procedures are as follows:

(i) For fits with $N_{\rm st}=1$, we estimate the initial parameters, central values, and widths of the priors via linear regression. For fits with any $N_{\rm st}$, we assign 10% of the respective central value or 100% of the previous error (estimate)—whichever is larger—to the widths of the two priors related to the ground state. The main purpose of the fits with $N_{\rm st}=1$ in our analysis is to suggest suitable central values of the priors for the ground state parameters $C_0(\boldsymbol{r},a)$ and $aE_0(\boldsymbol{r},a)$ in the ensuing fits with $N_{\rm st}=2$.

(ii) The fits with $N_{\rm st}=2$ serve as our main result, as we are interested only in the ground state energy, i.e., $aE_0(\boldsymbol{r},a)$. We use the (uncorrelated) fits with $N_{\rm st}=1$ to obtain prior central values for the ground-state parameters. We assign 10% of this central value or 100% or the $N_{\rm st}=1$ error (estimate)—whichever is larger—to the widths of the two priors related to the ground state. For the energy difference $a\Delta_1=aE_1-aE_0$, we take a calculation in SU(3) pure gauge theory [83] fit to a Cornell parametrization,

$$a\Delta_1=-\frac{A}{R}+a_{f_{p4s}}B+a_{f_{p4s}}^2\sigma R, \tag{2.7}$$

with $A=-0.09364$ GeV fm, $B=1.11218$ GeV, and $\sigma=-0.309585$ GeV fm^{-1}; here R is a dimensionless measure of distance defined in Sec. III, and we employ $a_{f_{p4s}}$ from Table I to convert the right-hand side to lattice units. As we do not have robust prior information about the overlap factor $C_1(\boldsymbol{r},a)$ in $(2+1+1)$-flavor QCD, we choose a fairly loose prior $C_1(\boldsymbol{r},a)=0.10(0.10)$, which coincides with the usual sign and order of magnitude seen in earlier stages of the analysis. To err on the side of caution, we assign 20% of the respective central value to the width of the prior related to $a\Delta_1$.

(iii) For fits with $N_{\rm st}=3$, we use the (uncorrelated) fits with $N_{\rm st}=2$ to obtain prior central values for the ground-state and first excited-state parameters. We retain the assignment of 10% of the respective central value or 100% of the previous error (estimate)—whichever is larger—to the widths of the priors related to these states. However, we choose a width of 0.10 or 100%—whichever is larger—for the overlap factor $C_1(\boldsymbol{r},a)$ of the first excited state since we anticipate that we may have been incapable of separating it from the second excited state in the fit with $N_{\rm st}=2$. For $a\Delta_2$, we choose $2a\Delta_1$ and $a\Delta_1/2$ as the prior central value and width, respectively. As we have even less prior information about the overlap factor $C_2(\boldsymbol{r},a)$, and since it is known that the correlation functions with Symanzik action contain negative spectral weights for small $|\boldsymbol{r}|/a$, see, e.g., Refs. [17,84], we choose a very loose prior $C_2(\boldsymbol{r},a)=0.02(0.20)$ since this coincides with magnitude seen in earlier stages of the analysis. The main purpose of the fits with $N_{\rm st}=3$ in our analysis is to serve as cross-checks that confirm that neither of the two lowest states would be modified significantly if another state were added.

With these priors in hand, we define an augmented χ^2 function for each $(\boldsymbol{r},a)$[10]:

$$\chi^2_{\rm aug}(\{C_n,aE_n\})=\chi^2_{\rm data}(\{C_n,aE_n\})+\chi^2_{\rm prior}(\{C_n,aE_n\}), \tag{2.8}$$

$$\chi^2_{\rm data}(\{C_n,aE_n\}) = \sum_{u,w\in[\tau_{\rm min},\tau_{\rm max}]/a}\Delta(u;N_{\rm st}|\{C_n,aE_n\})[\sigma^{-2}]_{uw} \times\Delta(w;N_{\rm st}|\{C_n,aE_n\}), \tag{2.9}$$

$$\Delta(u;N_{\rm st}|\{C_n,aE_n\})=C(u)-F(u;N_{\rm st}|\{C_n,aE_n\}), \tag{2.10}$$

where $C(u)$ denotes a Monte Carlo estimate of the correlator $C(\boldsymbol{r},ua,a)$, σ^2 their covariance in the sample, and F the right-hand side of Eq. (2.3) truncated to $N_{\rm st}$ states and considered to be a function of the C_n and aE_n and parametrized by the lattice time u (or w). The prior term $\chi^2_{\rm prior}$ is given in Eq. (2.6) above. For each $(\boldsymbol{r},a)$, we minimize $\chi^2_{\rm aug}$ to obtain the best-fit values of $(\{C_n,aE_n\})$, $0\le n<N_{\rm st}$.

We show representative plots of p-value distribution (across the $N_J=100$ jackknife pseudoensembles) for the physical β `7.00 M i` ensemble in Fig. 24 in the Appendix B 1. Here, p is defined as described in Appendix B of Ref. [85]. The energy levels and overlap factors in Fig. 23 (concerning another ensemble, namely the physical β `6.72 M i` ensemble), suggest that constraining excited states is challenging at small distances, hence the presence of a few outliers for small $|\boldsymbol{r}|/a$. At large enough $|\boldsymbol{r}|/a$ the distribution is quite flat and close to the ideal case, suggesting that the fit functions are good descriptions of the data.

We estimate the statistical errors of the fit parameters from either the Hessian matrix of the fit or from the distribution of the jackknife resamples. We find these two estimates to be similar in magnitude without obvious trends of one being usually larger or smaller than the other. In practice, we keep the jackknife error estimate and propagate statistical correlations in terms of the resamples. Moreover, given the stability analysis for the physical β `7.0 M i` ensemble—see Fig. 25 in Appendix B 1—we find that the influence of reasonable variation of $N_{\rm st}$ or $\tau_{\rm min}/a$

[10]The label $(\boldsymbol{r},a)$ for various quantities is suppressed to reduce clutter.

is covered by this statistical error estimate, so we do not modify the error of the ground state energy $aE_0(\boldsymbol{r}, a)$ further. Similarly, including or neglecting the off-diagonal entries of the correlation matrix does not lead to a statistically significant or systematic trend in the results. Because the uncorrelated fits do not require the randomized thinning in τ, described above, we carry these results to the next step as a cross-check. The final result of this analysis consists of the $(\tau_{\min}/a, N_{\rm st})$ table of $aE_0(\boldsymbol{r}, a)$ and the respective (statistical) error estimate, each on the mean and on the $N_J = 100$ jackknife pseudoensembles, and each with or without including the off-diagonal elements of the correlation matrix. This analysis permits quantitative studies of the impact of the various uncertainties on the physical results obtained in Secs. III–V. The results for aE_0 for the $N_{\rm st} = 2$ fits are contained in Supplemental Material [86].

III. FITS OF THE STATIC ENERGY

In this section, we take the results from the $N_{\rm st} = 2$ fits described in Sec. II to determine the "potential" scales r_i/a, $i = 0$, 1, 2 and the string tension $a^2\sigma$. The scales r_i are defined in Eq. (1.2) via the force in Eq. (1.1). Earlier calculations in $(2+1)$-flavor QCD [11,16,87] find the scales to be

$$r_0 \approx 0.475 \text{ fm}, \quad r_1 \approx 0.3106 \text{ fm}, \quad r_2 \approx 0.145 \text{ fm}, \tag{3.1}$$

corresponding to distinct physical regimes. On the one hand, $r_2 \sim 1/m_{\rm c}$ is similar to the inverse charm quark mass and, being right at the edge of the perturbative regime, expected to be insensitive to the light sea quarks. On the other hand, $r_0 \sim 1/\Lambda_{\rm QCD}$ is in the nonperturbative regime and, hence, is known to be sensitive to the pion mass, but is expected to be insensitive to charm sea quarks. As r_1 is in between these two, it might be sensitive to both the light and the charm quarks in the sea. At distances beyond r_0, but before string breaking, the force is a constant, namely the "string tension" $\sigma = -F(r)$, $r_0 \lesssim r \lesssim 1$ fm. As discussed in Sec. II, our data set is intended to obtain accurate results for the scales r_i (and $\alpha_{\rm s}$), rather than the string tension, which we obtain from data with $r \geq 0.58$ fm.

At nonzero lattice spacing, the static energy is available only at discrete distances, requiring some sort of numerical derivative in place of Eq. (1.2). Moreover, $aE_0(\boldsymbol{r}, a)$ depends on the direction of $\boldsymbol{r}$, so it is not a smooth function of the usual spatial Euclidean distance $r = |\boldsymbol{r}| = \sqrt{x_1^2 + x_2^2 + x_3^2}$. A good alternative is a measure of distance defined via the tree-level gluon propagator, known as the tree-level corrected distance [17].

In the following, we begin with the explicit definition of the tree-level corrected distance in Sec. III A. We then proceed in Sec. III B to the fits of the static energy, which yield the force and, thus, values for the scales r_i/a and string tension $a^2\sigma$ in lattice units and at fixed lattice spacing. This subsection includes discussion of the results, including the quark mass dependence and a comparison to earlier work. For relative scale setting in future work, it is convenient to combine the data in a fit to a smooth curve [88,89], which we do in Sec. III C.

A. Discretization artifacts and tree-level correction

On the lattice, the static energy is given at the tree level of perturbation theory by one-gluon exchange, just like in the continuum. In Coulomb gauge, its temporal component reads

$$D_{44}(k) = a^2\left[4\sum_{j=1}^{3}\sin^2\left(\frac{1}{2}ak_j\right) + c_w\sin^4\left(\frac{1}{2}ak_j\right)\right]^{-1}, \tag{3.2}$$

where $c_w = 0$ for the (unimproved) Wilson gauge action and $c_w = 1/3$ for the (improved) Lüscher-Weisz action [23]. As in the continuum, this component is independent of k_4 (in Coulomb gauge). For bare links, one simply takes the Fourier transform,

$$E_0^{\rm tree}(\boldsymbol{r}, a) = -C_{\rm F}g_0^2\int\frac{{\rm d}^3k}{(2\pi)^3}{\rm e}^{{\rm i}\boldsymbol{k}\cdot\boldsymbol{r}}D_{44}(k) \equiv -\frac{C_{\rm F}g_0^2}{4\pi}\frac{1}{r_I}, \tag{3.3}$$

where g_0 is the bare gauge coupling, $C_{\rm F} = (N_{\rm c}^2 - 1)/(2N_{\rm c})$ is a color factor, and the last expression defines r_I, which is discussed further below. Because the gluon propagator is a direction-dependent function of $\boldsymbol{k}$, the static energy $E_0(\boldsymbol{r}, a)$ is a nonsmooth function of the Euclidean distance r. Even beyond the tree level, one finds that the static energy is much smoother in r_I, which we refer to below as the tree-level improved or tree-level corrected distance. For example, $r = 3a$ for both $\boldsymbol{r} = (3,0,0)a$ and $(2,2,1)a$, but $r_I(3,0,0) = 2.979a$ while $r_I(2,2,1) = 3.013a$. Even beyond the tree level, $E_0(3,0,0) < E_0(2,2,1)$. We have computed the tree-level corrected distances r_I/a in the infinite-volume limit for each vector $\boldsymbol{r}/a$ with $|\boldsymbol{r}|/a \leq 6$ both for bare links or for links after one step of HYP smearing [79] using the HiPPy software package and the HPsrc software framework [90,91]. HYP smearing introduces a nontrivial vertex on either side of D_{44} in Eq. (3.3), thus modifying r_I. For example, in this case $r_I(3,0,0) = 3.020a$ while $r_I(2,2,1) = 2.997a$. The results are in Table IV in Appendix B 2 for bare and HYP-smeared links.[11] The former are consistent with previous results [68,93] up to very small finite-volume effects.

[11]These results are part of an ongoing project aiming at a full one-loop calculation in lattice perturbation theory [92]. To our knowledge, the improved distance with HYP smearing appears in Table IV for the first time.

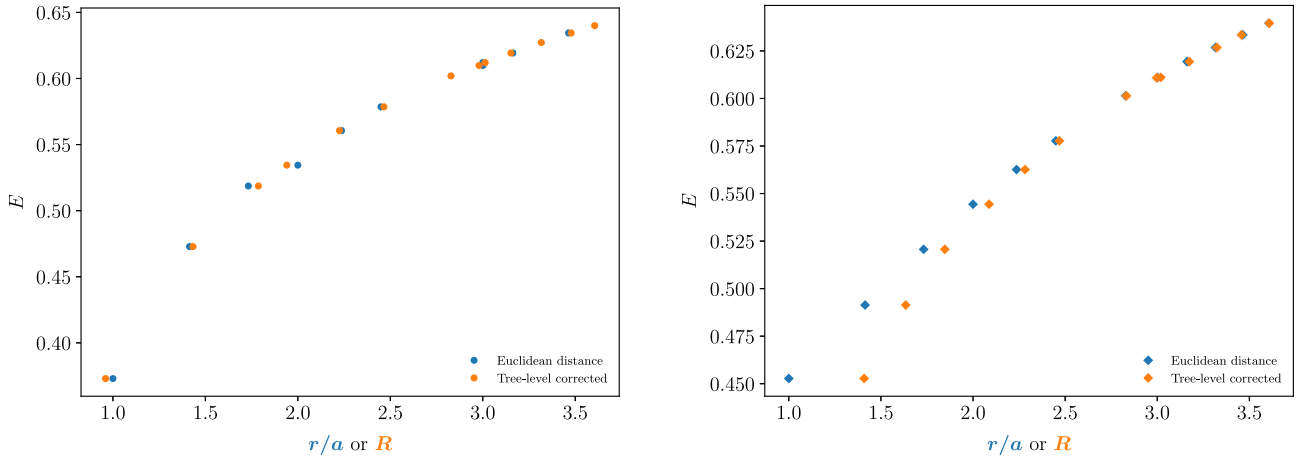

FIG. 2. The static energy $E(R,a)$ from the fits with $N_{\rm st}=2$ with preferred $\tau_{\rm min}/a$ for the physical β 7.00 M i ensemble, vs two measures of the distance. Left: data from bare links (right: HYP smeared). The static energies plotted against the tree-level improved distance R (Euclidean distance r/a) are colored orange (blue). The static energies with bare links roughly follow a $1/r$ in terms of both distances measures up to small nonsmooth discretization artifacts; cf., Fig. 3. The static energy with HYP-smeared links is far from Coulomb-like when plotted against the Euclidean distance r/a, when $r/a \lesssim 2.5$, but using the improved distance R removes this distortion. Serious nonsmooth discretization artifacts remain; cf., Fig. 3.

For the rest of this section, it is convenient to switch to lattice units. We introduce $E(R,a)=aE_0(\boldsymbol{r},a)$ and $R=r_I/a$. The tree-level correction reduces the size of nonsmooth discretization artifacts considerably but not completely. Figure 2 shows how the results on the β 7.00 M i ensemble change (apparent) shape when switching from the Euclidean distance r/a to the improved distance R. The behavior is similar to previous calculations in $(2+1)$-flavor QCD [17]; see the side-by-side comparison of Figs. 12 and 13 of Ref. [17]. The improvement, especially for HYP-smeared data, is readily apparent. That said, a closer look—dividing the data by a Cornell fit over the range $2.7 \le R \le 4.7$ as in Fig. 3—shows the tree-level correction is insufficient to produce a result for $E(R,a)$ that is smooth at the level of its statistical errors. In previous calculations in $(2+1)$-flavor QCD with a much denser set of lattice spacings [17,68], the residual discretization artifacts were taken care of through a heuristic nonperturbative correction procedure [17,68,94], but here we do not pursue such an approach.

Correlation functions are distorted at small $|\boldsymbol{r}|/a$ by contact-term interactions between overlapping "fat links" from which the temporal Wilson lines are constructed. With one iteration of HYP smearing applied to each temporal Wilson line, the distance vectors up to $\boldsymbol{r}/a \le (2,2,2)$ are, in principle, affected by such contact terms. The contribution along the cubic diagonal is suppressed (for the standard choice of parameters, $\alpha_1=0.75$, $\alpha_2=0.6$, and $\alpha_3=0.3$ [79]) by $(0.135)^2 \approx 2\%$ against a corresponding "thin link" contribution, giving rise to effects commensurate with the differences between Euclidean or improved distances with bare links. The contact-term contributions remain quantitatively significant even at the maximal range $\boldsymbol{r}/a \le (2,2,2)$. The intermittent ordering of r/a for vectors with largest component $2a$ or $3a$ leads to discontinuous changes in the HYP-smeared result much larger than the tiny statistical errors, see Fig. 3, in particular, between $\boldsymbol{r}/a=(3,0,0)$ and $\boldsymbol{r}/a=(2,2,1)$ or between $\boldsymbol{r}/a=(2,2,2)$ and its neighbors. To reduce the impact of these discontinuities, we omit $\boldsymbol{r}/a=(3,0,0)$ and $\boldsymbol{r}/a=(2,2,2)$ from our data set with smeared links.

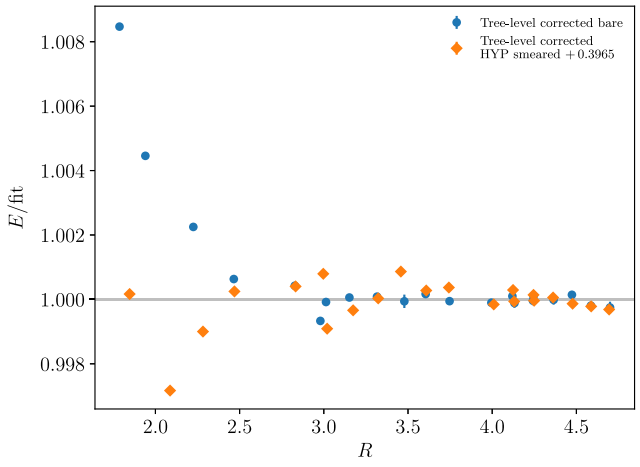

FIG. 3. The static energy $E(R,a)$ again on the β7.00 M i ensemble, divided by a Cornell-fit performed in the range $2.7 \le R \le 4.7$, for bare-link (blue circles) and HYP-smeared (orange diamonds) data. Even after using the tree-level improved distance R, residual nonsmooth discretization artifacts remain: the bare-link data are not smooth at $R=3$ and $R=\sqrt{17}$, for example, while the HYP-smeared data are not smooth until (at least) $R>4.5$.

B. Determination of the scales and the string tension from the static energy

Even as a function of R, the lattice result for the static energy $E(R,a)$ contains nonsmooth residual discretization artifacts larger than its statistical errors, yet we require a smooth interpolation to define its derivative. We choose the Cornell potential,

$$E(R, r/a, a) = -\frac{A}{R} + B + \Sigma R, \tag{3.4}$$

as a functional form because it encodes the main features of the static energy. In practice, we adjust the constant term B by adding a shift such that $E((3,0,0),a) + E((2,2,1),a) = 0$, i.e., $B = A/R_* - \Sigma R_*$, where $R_* \equiv \frac{1}{2}[R(3,0,0) + R(2,2,1)]$. We consider $RE(R,a)$ in order to get rid of the leading Coulomb behavior, which results in the functional form

$$\begin{aligned} RE(R,a) &= -A + BR + \Sigma R^2 \\ &= -A\left(1 - \frac{R}{R_*}\right) + \Sigma(R^2 - RR_*). \end{aligned} \tag{3.5}$$

On each ensemble, we fit the data to the right-hand side of Eq. (3.5) to obtain A and Σ, from which we solve $c_i = A + \Sigma(r_i/a)^2$ to obtain the scale r_i/a (for each $i = 0, 1, 2$). For fits at large distances, we identify Σ with the string tension (in lattice units, i.e., $\Sigma = a^2\sigma$).

For tests, we try adding to the right-hand side of Eq. (3.4) direction-dependent terms $\kappa_{\rm p}\Delta_{\rm p}(r/a)$ or $\kappa_{\rm LW}\Delta_{\rm LW}(r/a)$, which are defined via Eq. (3.3) in terms of the gluon propagator for the plaquette or Lüscher-Weisz action:

$$\begin{aligned} \Delta_{\rm p}(r/a) &\equiv \left(\frac{1}{R_{\rm p}} - \frac{a}{r}\right) = {\rm O}(a^2), \\ \Delta_{\rm LW}(r/a) &\equiv \left(\frac{1}{R} - \frac{a}{r}\right) = {\rm O}(a^4). \end{aligned} \tag{3.6}$$

Here, $R_{\rm p}$ is the same as R but for the plaquette-action gluon propagator. The coefficients $\kappa_{\rm P}$ or $\kappa_{\rm LW}$ are expected to be numbers of order 1 times leading powers of $\alpha_{\rm s}^3$ or $\alpha_{\rm s}^2$, respectively, expected from power counting arguments in the Symanzik effective theory. The nonsmooth contributions from both terms of Eq. (3.6) are dropped in the determination of the force as the derivative of a smooth function.

These fits entail several challenges. The Cornell potential is too simple to describe the full range of distances, so for each scale r_i we fit to a narrow interval around $r_i/a_{f_{p4s}}$ with r_i as in Eq. (3.1) and $a_{f_{p4s}}$ as in Table I. For the ensemble β `7.28 M iii`, we choose the interval to be $\pm 35\%$ and $\pm 30\%$, otherwise. We also require six (fourteen) or more points below (above) $r_i/a_{f_{p4s}}$ and expand the interval towards smaller (larger) r/a if needed (as happens on the coarser ensembles). If the latter criterion cannot be met, then we relax it to five (eleven) instead. The coarsest ensembles cannot provide enough points, particularly below $r_i/a_{f_{p4s}}$, so then we do not attempt fits. In practice, this means we quote results for r_1/a (r_2/a) only for $\beta > 5.80$ ($\beta > 6.30$). For the string tension, we fit the range $0.58\ {\rm fm} \le r_I < r_{\rm max}$, with $r_{\rm max}$ from Table II.

The next challenge is the correlations among the aE_0 data in each fit. As discussed in Sec. II, we use $N_J = 100$ jackknife pseudoensembles to estimate the covariance matrix, permitting good control of up to $\sim\sqrt{N_J} = 10$ eigenvalues (in practice, of the correlation matrix). Unless we restrict the fit to only ~ 10 distinct R, we encounter many unphysically small eigenvalues. We address this issue by thinning the data, choosing ten (fifteen) points at random in the intervals specified above for the scales r_i (string tension). We pick three R values in the lower half of the interval and seven R values in the upper half for fits of the scales as illustrated in Fig. 4. This asymmetric selection is motivated by three general properties, namely the decrease of the slope of the static energy at larger R, the increase of the noise at larger R, and the higher density of data at larger R due to the larger number of Euclidean spatial vectors with integer components. Without the random picks the first two properties would be counterbalanced by the latter in terms of the constraining power attributable to data at smaller or larger R. In our procedure that uses a fixed number of data, we have to make a somewhat arbitrary choice how to skew the selection procedure to mimic these properties. At very large R, the data are similarly noisy across the available R range, the slope does not change visibly, and the density is always fairly high for all ensembles. Hence, these considerations do not apply, and we pick five R values out of each third of the interval for fits of the string tension.

Now, the very restrictive fit form, Eq. (3.5), may underestimate the uncertainties in the derivative, and a thinned-out set of R values may exaggerate the influence of nonsmooth discretization artifacts. For this reason, we repeat the random picks N_P times. For the finest β `7.28 M iii` ensemble we use $N_P = 200$, and for the others $N_P = 100$. The same N_P sets of random picks are used on each of the N_J jackknife pseudoensembles. The procedure is illustrated in Fig. 4, which shows the first 30 fits on the first of the jackknife pseudoensemble of the physical β `7.00 M i` ensemble. Sometimes there are fewer than three points to the left of the fit result, which happens because the separator is set by r_i from $(2+1)$-flavor QCD, Eq. (3.1), and the $(2+1+1)$-flavor QCD scale $a_{f_{p4s}}$ in Table I. This effect is found to happen most often for r_2, which is the distance most sensitive to the charm quark sea.

While repeating the fit on all jackknife pseudoensembles takes care of the correlated statistical fluctuations, using different random picks accounts for the systematic

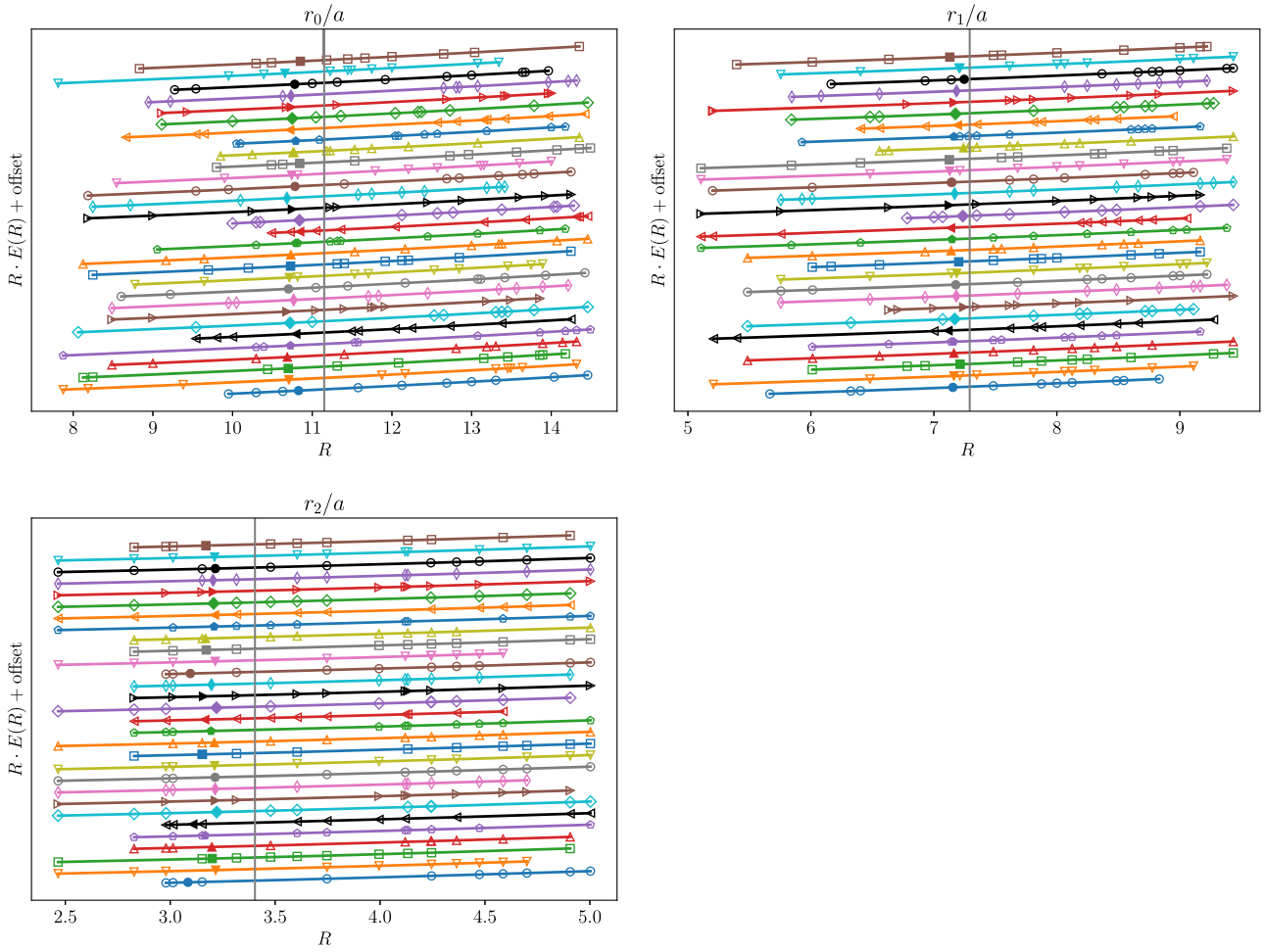

FIG. 4. First 30 of the N_P randomly selected data points (open symbols) and corresponding fit results (filled symbols) for the first jackknife pseudoensemble of the bare-link data on the physical β `7.00 M i` ensemble. A vertical offset is introduced for clarity, while the colors and symbol shapes are for visual distinction only. The separation between the lower and upper half of the interval is indicated by a gray vertical line, based on Eq. (3.1) and $a_{f_{p4s}}$ as in Table I.

uncertainties that arise from nonsmooth discretization artifacts and thinning the data. For each of the N_P sets of random picks, we obtain the mean and statistical error from the variation over the N_J jackknife pseudoensembles. Figure 5 shows the jackknife histograms of the N_P picks for each of the three r_i/a. The variation over the random picks is much larger than the statistical variance of each individual pick. (Bear in mind that the width of a jackknife histogram has to be multiplied by $\sqrt{N_J}$ to get the statistical error.) Under the natural assumption of some uncorrelated component in the statistical fluctuations across different R, the random picks partially account for statistical errors, too. It is not *a priori* obvious whether such statistical or systematic effects dominate the spread of the distribution of the histograms associated with the random picks. Statistically significant variation of the (weighted) mean in Fig. 5 upon including some direction-dependent parametrization of discretization artifacts via $\kappa_P \Delta_P$ or $\kappa_{LW} \Delta_{LW}$ as in Eq. (3.4) would indicate dominance of the latter, while a small variation of the (weighted) mean would suggest dominance of the former. We observe a small variation of the weighted mean, covered by the spread without direction-dependent terms, which increases slowly toward smaller distances R. We conclude that statistical effects are dominant for the distances considered.

There are systematic dependencies between the extracted scale r_i/a and the details of the N_P random picks, which can be visualized if the N_P random picks are projected to a more simple measure such as the (randomly chosen) minimum distance R_{min}. For example, Fig. 27 in Appendix B 3 shows that the extracted r_i/a sometimes is, and sometimes is not, correlated with R_{min}. For some other cases, these dependencies may be clearly monotonic, rather flat, or clearly nonmonotonic. Lacking clear patterns, we account for the variation by taking for the central value an average of the N_P different mean values, weighted by the statistical (jackknife) errors and estimating the systematic uncertainty by considering the maximal

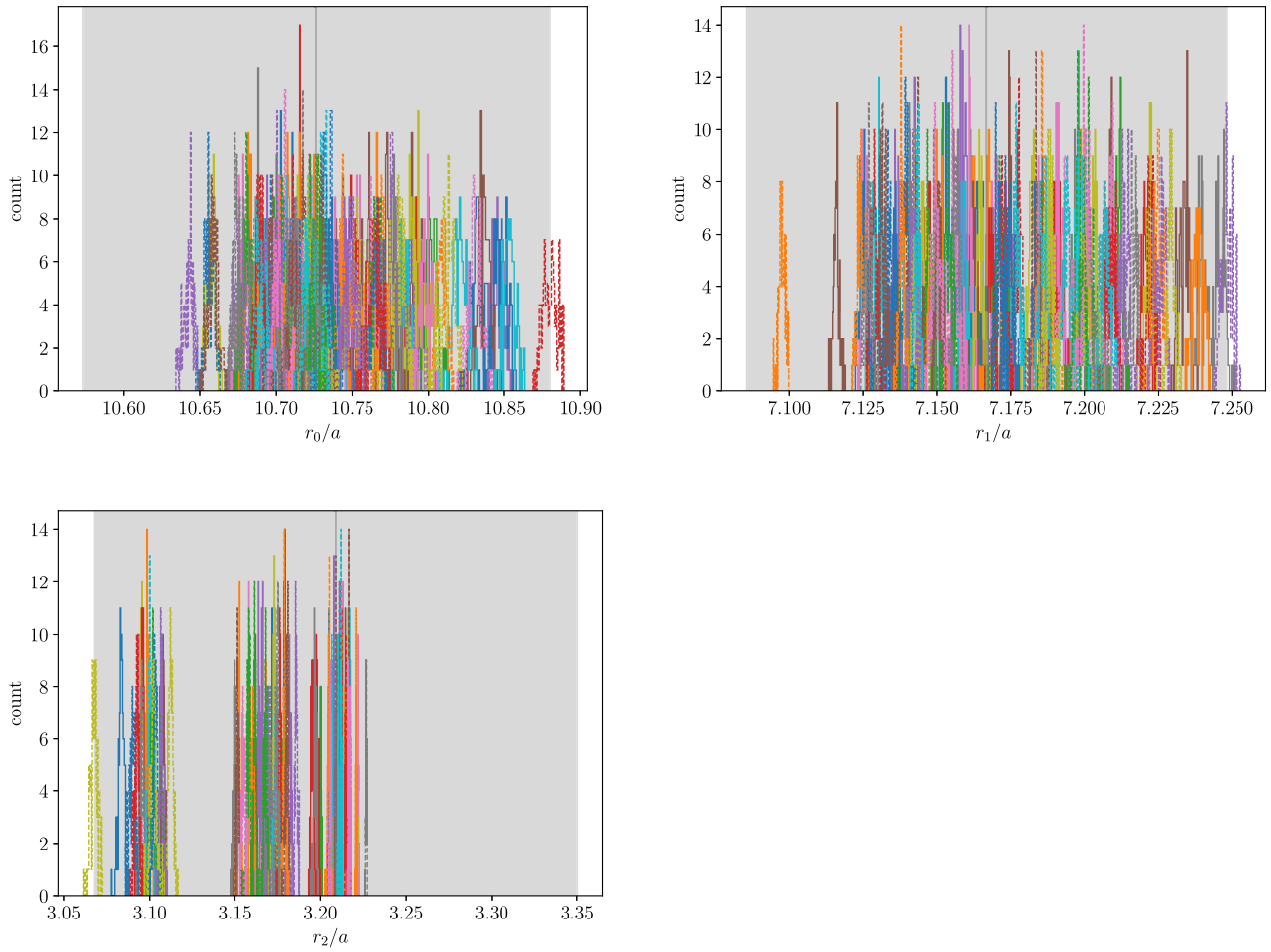

FIG. 5. Jackknife histograms of the r_i/a for each of N_P random picks, distinguished by color for the bare-link data on the β `7.00Mi` ensemble. The gray vertical lines and bands represent the corresponding mean value and error estimate, described in the text and collected in Table V. Similar plots for $a^2\sigma$ are shown in Fig. 26 in Appendix B 3.

absolute difference between this weighted mean and any of the N_P random picks. This systematic uncertainty estimate is much larger than the (statistical) sample standard deviation for small r_i/a, but smaller than it for large enough r_i/a. Nevertheless, the statistical error of the mean—proportional to the sample standard deviation—is practically always smaller than this systematic uncertainty estimate. Although the statistical error of the mean is further reduced for the smeared-link result, the systematic error remains similar. As a consequence, the benefits of smearing are astonishingly small for the determination of the lattice scale.

Turning to the string tension, our data are insufficient to constrain the coefficient A when fitting the static energy over the range $r \geq 0.58$ fm. This range lies between the Coulomb and (asymptotic) string regime, where a $1/R$ behavior is also expected albeit on very different physical grounds [95]. With no obvious physical origin for a $1/R$ term in this range, we choose fits fixing A to either A_{r_0}, the fit results from the r_0 fit, or $\pi/12$ [95]. In fact, A_{r_0} turns out to be within a factor of 2 of $\pi/12$, and it is natural to expect a coefficient of an effective $1/R$ term within this range. As the string tension is not the main objective of this work, we simply present both choices in Appendix B 3.

The resulting values and errors for the scales r_i/a and the string tension $a^2\sigma$ are given in Table V of Appendix B 3. We observe a strikingly nontrivial quark mass dependence for all scales r_i/a. First, as naively expected and observed in previous calculations in $(2+1)$-flavor QCD [11], we obtain larger values of r_i/a at smaller light quark masses,[12] which is clearly visible in Fig. 6. However, this effect seems to have a very peculiar lattice spacing dependence. On the one hand, the physical m_l/m_s or $m_l/m_s = 1/10$ results are very close at $\beta = 6.00$ or $\beta = 6.30$, while the $m_l/m_s = 1/5$ is somewhat off at $\beta = 6.30$. On the other hand, at

[12]For unclear reasons, the smeared result for r_1/a with the intermediate mass $m_l/m_s = 1/10$ (β `6.30Mii`) does not follow a consistent mass ordering and is a clear outlier from many other trends, too.

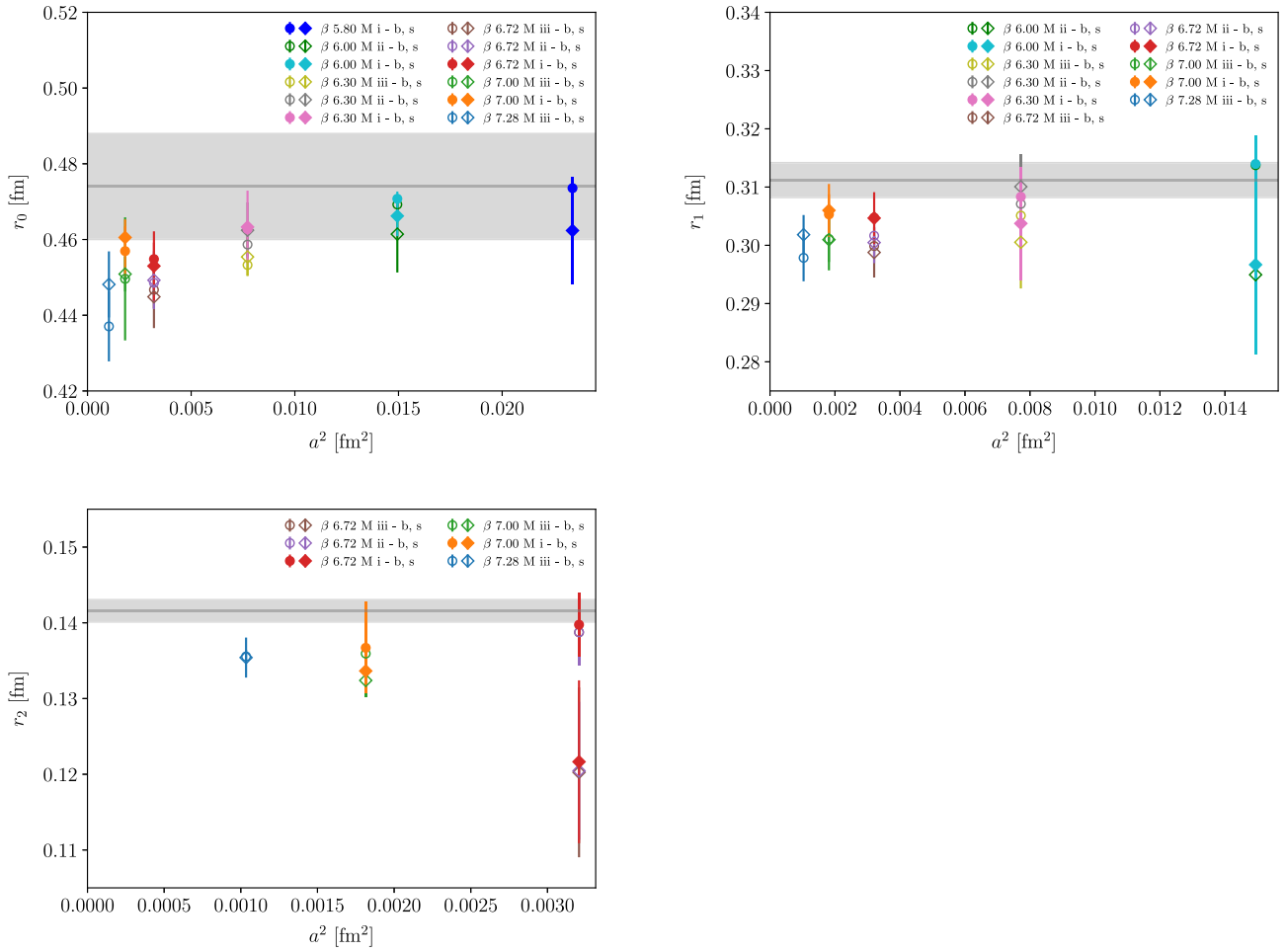

FIG. 6. The potential scales r_i/a, $i = 0, 1, 2$ for all ensembles (indicated by colors) and bare (circles) and smeared (diamonds) gauge links. We use the lattice scale $a_{f_{p4s}}$ to convert our r_i/a results to physical units and $a^2_{f_{p4s}}$ for the x coordinate. Filled symbols correspond to physical light quark mass ensembles, while open symbols represent larger than physical quark masses. The gray band indicates the $(2 + 1)$-flavor value from Flavour Lattice Averaging Group (FLAG) 2021 [96] for r_0 and r_1, and from Ref. [11] for r_2; see those references for details on the conversion to physical units. Similar plots for $\sqrt{\sigma}$ are shown in Fig. 28 of Appendix B 3.

$\beta = 6.72$, the $m_l/m_s = 1/10$ or $m_l/m_s = 1/5$ results are very close, while the physical m_l/m_s is somewhat off. Instead of being due to a statistical fluke, this effect may be caused by the variation of the charm or strange quark masses, which are highly correlated across the ensembles; see Table I. At $\beta = 6.72$, the $m_l/m_s = 1/10$ or $m_l/m_s = 1/5$ ensembles have a charm quark mass that is 10% larger than for the physical m_l/m_s ensemble. However, at $\beta = 6.30$ the physical m_l/m_s or $m_l/m_s = 1/10$ ensembles have almost the same charm quark mass, which is about 2% smaller than for the $m_l/m_s = 1/5$ ensemble. And at $\beta = 6.00$ the physical m_l/m_s or $m_l/m_s = 1/10$ ensembles have identical charm masses. This observation suggests that the dependence of the potential scales on the charm or strange quark masses may be significantly larger than previously anticipated. In Sec. III C, we study this quark mass dependence quantitatively when fitting the r_i/a data to a smooth curve in g_0^2 and quark masses. The light quark mass dependence becomes insignificant for r_2/a, in line with results in $(2 + 1)$-flavor QCD [11].

Since the correlators with bare- or smeared-link variables represent different discretizations, different values of the scales r_i/a with bare or smeared links are to be expected. This effect needs to be distinguished from the distortions of the smeared-link correlators at small distances due to the unphysical contact-term interactions. While the former is not a problem, the latter needs to be avoided. The smeared-link data yield substantially smaller values when $r_i/a < 3$, namely for r_2/a at $\beta = 6.72$ or r_1/a at $\beta = 6.0$, which are clearly inconsistent with the bare-link results. It is suggestive to attribute this discrepancy to the contact-term interactions seen in Fig. 2. Hence, we discard these smeared results (enclosed by square brackets in Table V in Appendix B 3) and use the bare results in their place when smoothening the scales and, in Sec. IV, when extrapolating to the continuum limit. In the range $3 \lesssim r_i/a \lesssim 4$, which

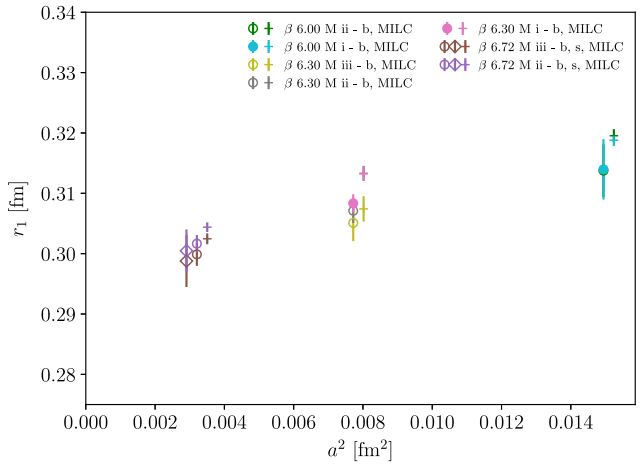

FIG. 7. Comparison of our direct determinations of r_1/a, Table V, to previous results on some on the ensembles from the MILC Collaboration [18,19]. As in Fig. 6, we convert all results to physical units via $a_{f_{p4s}}$ and use $a^2_{f_{p4s}}$ for the x coordinate.

includes the maximal R where the contact-term interactions between the smeared-link variables distort the correlation function, this underestimation of r_i/a with smeared links becomes mild and usually consistent within errors. However, the shift between r_1/a with bare and smeared links in the β `6.30 M ii` ensemble clearly deviates from the pattern exhibited by the other two masses at this (or any larger) β. Since the result with bare links is consistent with the expected pattern of a monotonic light quark mass dependence, we conclude that this smeared-link result is not reliable. To be consistent, we discard the r_1/a results with smeared links for all sea quark masses at $\beta = 6.30$ (enclosed by square brackets in Table V in Appendix B 3) and use the bare results in their place. We opt, however, to keep the smeared-link results for r_0/a at $\beta \leq 6.0$ and for r_2/a at $\beta = 7.0$ since there is nothing obviously wrong with these. With smeared links we find compatible or slightly larger r_i/a for $r_i/a > 5$, where small-distance distortions can be ruled out; see Sec. III A.

Another striking feature of Fig. 6 is that our data lie consistently lower than the $(2+1)$-flavor results (shown as gray bands). In Fig. 7, we compare our r_1/a results to those from earlier calculations using common subsets of the ensembles obtained by the MILC Collaboration [18,19]. Our results are systematically lower than MILC's, significantly so at $\beta = 6.3$. Since the two sets of results are based on different fit procedures, they can differ by discretization effects. Our larger errors originate in the systematic error estimate from the full spread to the randomized variation of the R values in Sec. III B. Even so, the trend of both data sets is toward a lower value of r_1 (in fm) than that from the FLAG compilation of $(2+1)$-flavor results; cf. Fig. 6. This trend is corroborated by our data at smaller lattice spacings, as discussed further in Sec. IV.

C. Smoothening

For relative scale setting in future work on the HISQ ensembles, it is useful to summarize the results for r_i/a as functions of the squared bare gauge coupling g_0^2 and the bare quark masses am_q.[13] In this work, we use an Allton *Ansatz* [88], in particular, the very generic form found, for example, in Ref. [89], adapted to include the charm quark mass dependence,

$$\frac{a}{r_i} = \frac{C_0 f_\beta + C_2 g_0^2 f_\beta^3 + C_4 g_0^4 f_\beta^3}{1 + D_2 g_0^2 f_\beta^2}. \tag{3.7}$$

Here,

$$f_\beta = (b_0 g_0^2)^{-b_1/(2b_0^2)} \mathrm{e}^{-1/(2b_0 g_0^2)}, \quad b_0 = \frac{\beta_0^{(N_\mathrm{f})}}{(4\pi)^2}, \quad b_1 = \frac{\beta_1^{(N_\mathrm{f})}}{(4\pi)^4}, \tag{3.8}$$

is the integrated β function to two loops, which scales asymptotically as $f_\beta \propto a$, and $\beta_{0,1}^{(N_\mathrm{f})}$ are the first two coefficients of the β function; see Appendix C 1. In the present case, $N_\mathrm{f} = 4$. Further,

$$C_0 = C_{00} + C_{01l}\frac{am_\mathrm{l}}{f_\beta} + C_{01s}\frac{am_\mathrm{s}}{f_\beta} + C_{01}\frac{am_\mathrm{tot}}{f_\beta} + C_{02}\frac{(am_\mathrm{tot})^2}{f_\beta},$$
$$C_2 = C_{20} + C_{21}\frac{am_\mathrm{tot}}{f_\beta}, \quad am_\mathrm{tot} = 2am_\mathrm{l} + am_\mathrm{s} + am_\mathrm{c}, \tag{3.9}$$

where C_{00}, C_{01l}, C_{01s}, C_{01}, C_{02}, C_{20}, C_{21}, C_4, and D_2 are parameters to be determined from fits described below. In C_{00}, the second through fourth terms parametrize continuum limit quark mass dependence, while the C_{02} term represents a discretization effect on the largest (i.e., fourth) term. We find we cannot constrain C_4 and C_{21}, so in the following, they are set to zero.

Further, we cannot reliably constrain the coefficients of multiple quark mass dependent terms. Given that the charm quark mass is much larger than light or strange quark masses, am_tot is dominated by the variation of am_c; fits using only am_c (in place of am_tot) typically have larger reduced χ^2 than those incorporating the light quark mass dependence as well through am_tot. Since the strange quark mass usually varies quite similarly to the charm quark mass, such that the physical value of $m_\mathrm{c}/m_\mathrm{s}$ is realized to a fair approximation, using $am_\mathrm{c} + am_\mathrm{s}$ (in place of am_tot) would not lead to different conclusions. Thus, parametrizations with some light quark mass dependence are preferred by the data. The parametrization yielding smallest reduced χ^2 (averaged over four fits for r_0/a or r_1/a using

[13]Here, it is not possible to do so for r_2/a because we have data at only three lattice spacings.

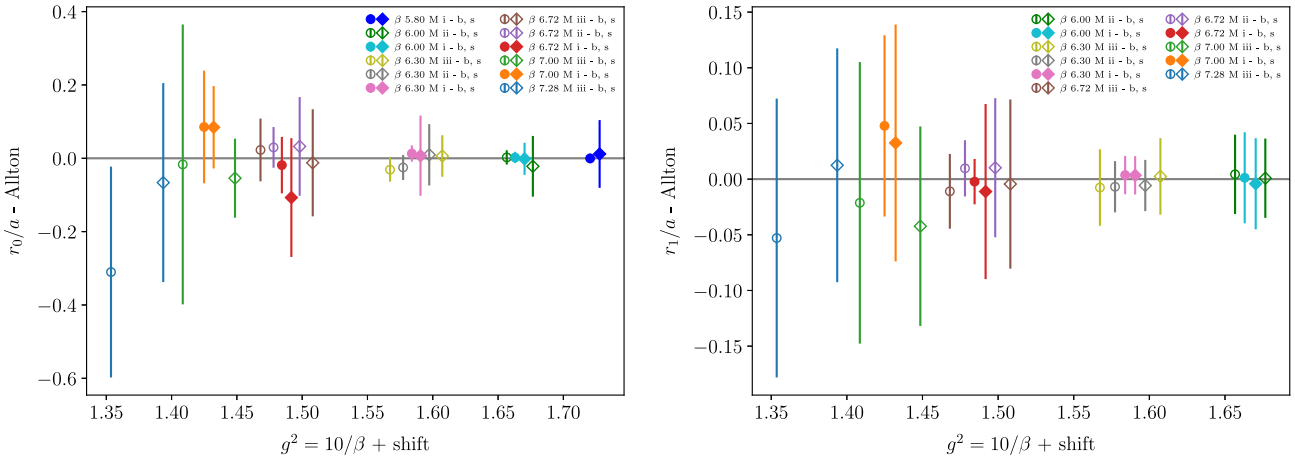

FIG. 8. Residues of the Allton fits for r_i/a using all ensembles (indicated by the color). Filled symbols correspond to physical light quark mass ensembles, while open symbols represent larger-than-physical quark masses; circles (diamonds) denote bare- (smeared)-link data. We use the squared bare gauge coupling g_0^2 for the x coordinate, but shift bare- and smeared-link data horizontally by $\mp 0.1 m_l/m_s$ to improve the visibility.

both bare-link or smeared-link data) is quadratic in am_{tot} with only C_{00}, C_{02}, C_{20}, and D_2 being allowed to vary. For r_1/a, fits are similarly good with a parametrization linear in am_{tot} with only C_{00}, C_{01}, C_{20}, and D_2 being allowed to vary. Finally, for r_0/a, fits with a parametrization linear in am_l and am_s (neglecting am_c) are similarly good, too. The coefficients for the total quark mass term are compatible between all linear or between all quadratic fits; see Table VI in Appendix B 4. The respective covariance matrices are supplemented as text files. Moreover, the coefficients of fits for bare or smeared links are compatible. We point out that the dominant light quark mass dependence in both the linear or the quadratic fit is actually linear, as $(am_{\mathrm{tot}})^2 = (am_c + am_s)^2 + 4(am_c + am_s)(am_l) + \cdots$. We use the quadratic fits including all ensembles as our main results. Their residuals do not show a consistent pattern of the light quark mass dependence; see Fig. 8.

The regression errors of the interpolated values r_i/a obtained from the Allton fit coefficients are reported in Table VII in Appendix B 4. They are similarly large as the errors from the direct determination, while some outliers among the errors have been eliminated; cf. Table V in Appendix B 4. In order to test whether the Allton fit might assign an undue large weight to any ensemble, we repeated the same Allton fit on each subset of the data leaving out one ensemble in each; all of these fits are covered by the regression error of the Allton fit using the full data set, see Fig. 9. In the corresponding curves, evaluated at

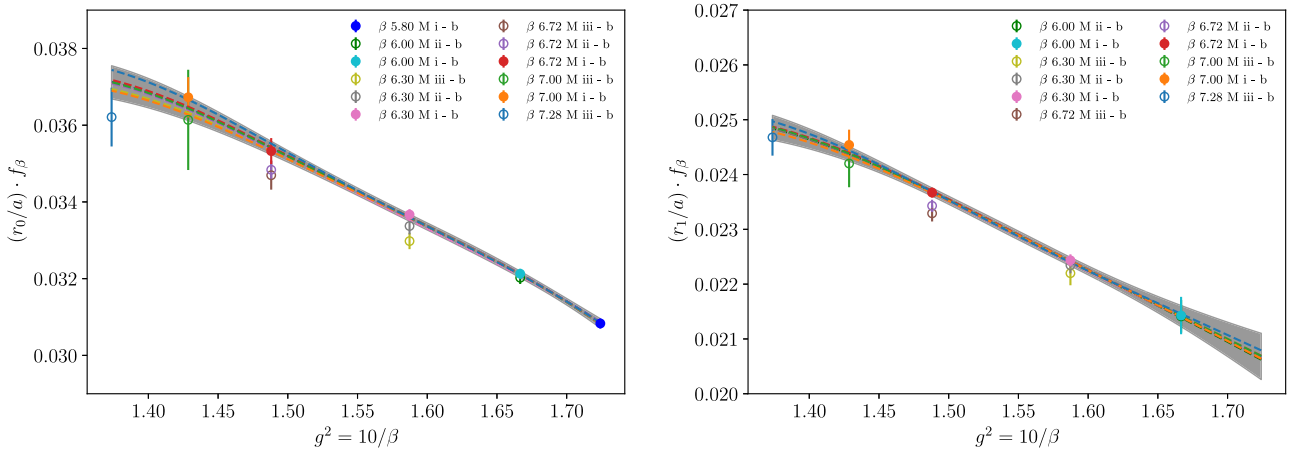

FIG. 9. The potential scales r_i/a, $i = 0, 1$ multiplied by the two-loop β-function, f_β as in Eq. (3.8), for all ensembles (indicated by colors) and bare links. Filled symbols correspond to physical light quark mass ensembles, while open symbols represent larger than physical quark masses. The curves correspond to the Allton fit, Eq. (3.7), evaluated at the masses of the physical mass ensembles using the parameters given in Table VI in Appendix B 4. The color of the lines indicates the ensemble that has been left out, while the black curve (hidden behind the other lines) is the one including all, with the band representing its regression error. We use the squared bare gauge coupling g_0^2 for the x coordinate. A corresponding plot for smeared links is in Fig. 29 in Appendix B 4.

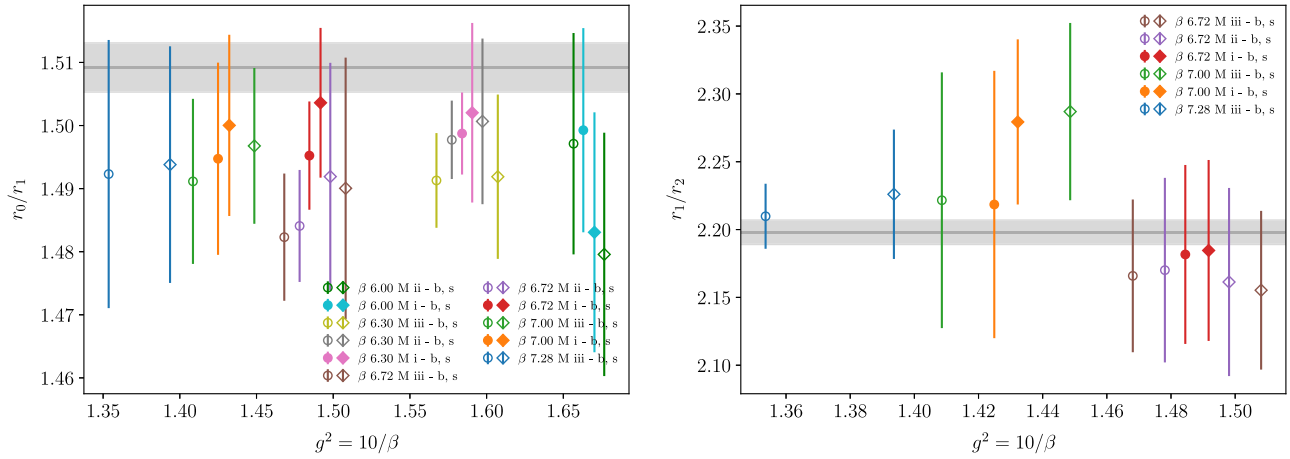

FIG. 10. Ratios of smoothened r_0/r_1 or r_1/r_2 for all ensembles. For visibility's sake the data are shifted horizontally by $\mp 0.1 m_l/m_s$ for the bare-/smeared-link data. The gray solid line and band show published $(2+1)$-flavor values [11,16] for r_0/r_1 and r_1/r_2, respectively.

$m_l \geq m_s/10$ with the corresponding am_s and am_c values (not shown in Fig. 9), we see a wiggly structure between $\beta = 7.28$ and $\beta = 6.30$, which is more pronounced in r_0/a than in r_1/a; hints of such a trend were already seen in Fig. 6 and are interpreted as an effect due to the 10% variation of the charm mass between the different $\beta = 6.72$ ensembles. We also use the parametrization in terms of the Allton fit to obtain results in the chiral limit of the light quark mass, where we use m_s and m_c of the physical mass ensembles, or m_s and m_c of the only existing $\beta = 7.28$ ensemble. In the latter case, we estimate the physical value of the light quark mass from the sea strange quark mass using the physical m_l/m_s-ratio, i.e., $1/27.3$, to be $am_l = 0.000409$.

IV. CONTINUUM LIMITS

In Sec. III C, we have determined the individual results for the scales r_i/a and the string tension $a^2\sigma$ on each ensemble. Here, we form dimensionless combinations of the r_i/a and $a^2\sigma$. In particular, we compute r_0/r_1 and r_1/r_2 for which we use the smoothened values for $r_{0,1}/a$ given in Table VII in Appendix B 4 and the direct determination of r_2/a given in Table V in Appendix B 3. The results for the string tension are conveniently multiplied by the smoothened $(r_0/a)^2$; the square root of this product is collected in Table VII in Appendix B 4. We then perform continuum extrapolations of these universal dimensionless quantities. We also multiply the smoothened values for $r_{0,1}/a$ with $a_{f_{p4s}}$, cf. the last few paragraphs of Sec. III B, in order to perform a continuum extrapolation of these two dimensionful quantities.

A. Ratios r_0/r_1 and r_1/r_2

The errors of the individual r_i/a contain our estimates of systematic uncertainties, dominated by the variation of the independent randomly chosen sets of R values. These are considerably larger than the statistical errors, and as explained in the discussion around Fig. 5, we add them and the statistical uncertainties in quadrature. The regression errors of the smoothened r_i/a therefore reflect the systematic errors. We show the results for the ratios of the smoothened scales evaluated at the parameters of the individual ensembles as a function of the squared bare gauge coupling in Fig. 10. The gray bands indicate published $(2+1)$-flavor values [11,16]. Across all ensembles, our results for r_0/r_1 in $(2+1+1)$-flavor QCD are marginally lower than the HotQCD result in $(2+1)$-flavor QCD [16], where the approach to the continuum limit has been found to be flat within errors for similar lattice spacings with a variety of actions [14,16]. The $(2+1+1)$-flavor QCD result shows a fairly flat behavior, too, although there are hints of some curvature that point to a mild decrease towards the continuum limit. A systematic dependence on the light quark mass with larger r_0/r_1 for smaller pion mass is visible. With the exception of the results on the corresponding coarsest lattices, $\beta = 6.72$, our results for r_1/r_2 in $(2+1+1)$-flavor QCD turn out to be systematically higher than the result in $(2+1)$-flavor QCD, where the approach to the continuum limit has been found to be flat within errors for a similar range of lattice spacings [11]. The coarsest lattices for which r_2/a has been obtained in either analysis have $r_2/a < 3$. Such distances are still affected by substantial nonsmooth discretization artifacts after the tree-level correction, see Sec. III A. Since the $(2+1)$-flavor QCD analysis had benefited from nonperturbative corrections, they may have not been affected by a similar discretization artifact that impacts the $(2+1+1)$-flavor QCD result at $\beta = 6.72$; this might explain the somewhat lower value for r_1/r_2. No systematic dependence on the light quark masses can be resolved.

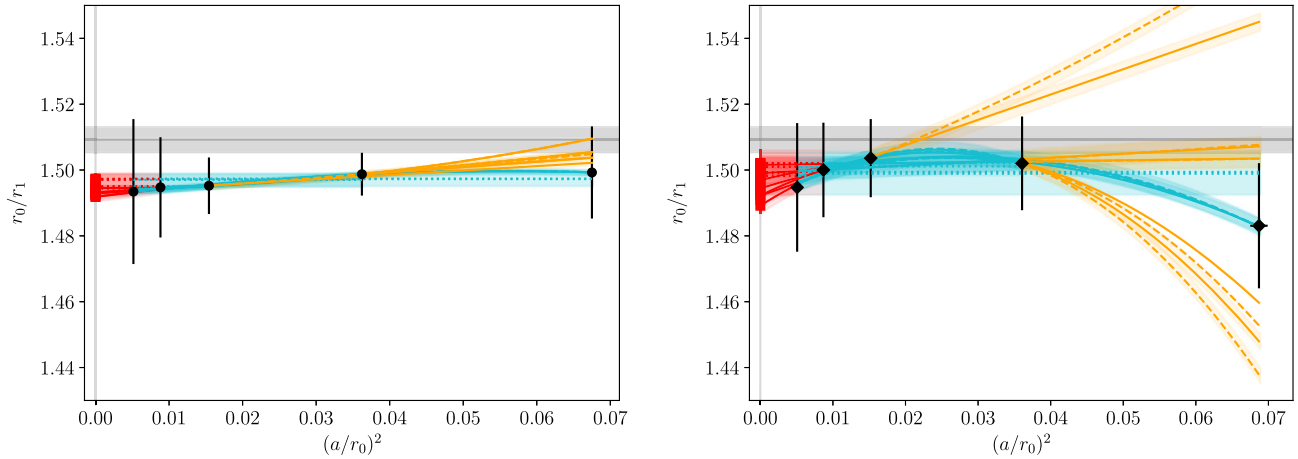

FIG. 11. Continuum extrapolation of the parametrization of r_0/r_1 evaluated at the physical m_l/m_s-ratio for $6.0 \le \beta \le 7.28$ as a function of $(a/r_0)^2$. The black points show the bare-link data (left) and the smeared-link data (right) with the corresponding continuum results shown in red. The lines and bands show the fit curves and errors; within the fit range in cyan, as extrapolations towards the continuum or coarser lattices in red/orange, respectively. The gray solid line and band indicate the HotQCD result in (2 + 1)-flavor QCD [16]. A corresponding plot as a function of $(a/r_1)^2$ is shown in Fig. 30 in Appendix B 5.

We now describe our continuum extrapolations following the same procedures for all quantities. For brevity and clarity, we denote each of these as ξ in the following. The leading discretization effects are of order $\alpha_s^2 a^2$ and a^4, as discussed in Sec. II A. With the lattice spacing dependence represented by $x = (a/r_0)^2$ or $(a/r_1)^2$, and the light quark mass dependence represented by $y = (am_l)_{\text{sea}}/(am_s)_{\text{sea}}$ or $(am_l)_{\text{sea}}/(am_s)_{\text{tuned}}$, we consider the functional forms[14]

$$\xi = \xi_0 \qquad \text{(weighted average)}, \tag{4.1}$$

$$\xi = \xi_0 + \alpha^2\xi_1 x \qquad \text{(lin)}, \tag{4.2}$$

$$\xi = \xi_0 + \alpha^2\xi_1 x + \xi_2 x^2 \qquad \text{(quad)}, \tag{4.3}$$

$$\xi = \xi_0 + \alpha^2[\xi_1 x + \xi_2 xy] \qquad \text{(l, lm)}, \tag{4.4}$$

$$\xi = \xi_0 + \alpha^2[\xi_1 x + \xi_2 xy] + \xi_3 x^2 \qquad \text{(q, lm)}, \tag{4.5}$$

$$\xi = \xi_0 + \alpha^2[\xi_1 x + \xi_2 xy^2] \qquad \text{(l, qm)}, \tag{4.6}$$

$$\xi = \xi_0 + \alpha^2[\xi_1 x + \xi_2 xy^2] + \xi_3 x^2 \qquad \text{(q, qm)}, \tag{4.7}$$

$$\xi = \xi_0 + \alpha^2[\xi_1 x + \xi_2 xy] + \xi_3 y \qquad \text{(l, lm, mc)}, \tag{4.8}$$

$$\xi = \xi_0 + \alpha^2[\xi_1 x + \xi_2 xy] + \xi_3 x^2 + \xi_4 y \qquad \text{(q, lm, mc)}, \tag{4.9}$$

$$\xi = \xi_0 + \alpha^2[\xi_1 x + \xi_2 xy^2] + \xi_3 y \qquad \text{(l, qm, mc)}, \tag{4.10}$$

$$\xi = \xi_0 + \alpha^2[\xi_1 x + \xi_2 xy^2] + \xi_3 x^2 + \xi_4 y \qquad \text{(q, qm, mc)}, \tag{4.11}$$

where we assume either $\alpha = \alpha_b \equiv g_0^2/(4\pi u_0^4)$, including the tadpole factors given in Table I (originally from Ref. [26]), or $\alpha = 1$, i.e., we either incorporate or ignore the one-loop improvement of the a^2 dependence.

We fit the ratio r_0/r_1 using the parametrization evaluated at four fixed m_l/m_s-ratios, namely, in the chiral limit of the light quark masses, or at the three sets of actual values present in the simulations, see Table I. Here we have five[15] data points available, which allows us to vary β_{min} and β_{max}. We start with a weighted average, Eq. (4.1), for $\beta_{\text{min}} \in \{7.0, 6.72, 6.3, 6.0\}$, and we use linear, Eq. (4.2), for $\beta_{\text{min}} \in \{6.72, 6.3\}$, and quadratic, Eq. (4.3), for $\beta_{\text{min}} \in \{6.3, 6.0\}$ fits in $(a/r_0)^2$. We use $\beta_{\text{max}} \in \{7.28, 7.0\}$. We repeat these fits with the exception of the weighted average as a function of $(a/r_1)^2$. These constitute inequivalent extrapolations with different error budgets: on the one hand, due to the different error in x,[16] and on the other hand, due to the different cutoff and quark mass dependence of r_0/a and r_1/a. The smoothened data, continuum results, and fit curves of the parametrization evaluated at the physical m_l/m_s-ratio as a function of $(a/r_0)^2$ are shown in Fig. 11. The errors of the ratio are obtained by adding the

[14]The abbreviations shown below are also the ones used in the Supplemental Material [86] providing details of the individual fit results.

[15]Not six because we do not determine r_1/a on the β `5.80Mi` ensemble.

[16]All of the fits here are performed using orthogonal distance regression fits that, in contrast to ordinary least squares minimization, also takes into account uncertainties in the independent variable [97].

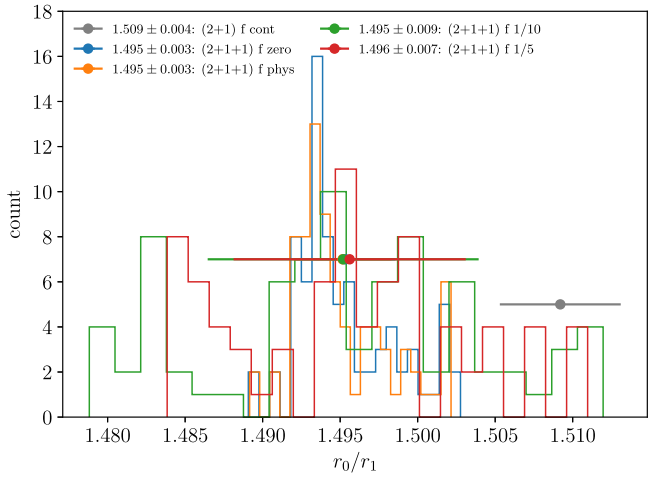

FIG. 12. Continuum results for r_0/r_1 are obtained at four different fixed m_l/m_s-ratios (distinguished by color). The histograms show the distributions accumulated from fits like those shown in Fig. 11. The symbols of each color correspond to the respective mean and standard deviation. The gray symbol indicates the HotQCD result in $(2+1)$-flavor QCD [16] for r_0/r_1.

errors derived from the full parameter covariance matrix of each parametrization in quadrature.

The distribution of the results for the four different light quark mass ratios (chiral limit, physical, $1/10$, and $1/5$) is shown in Fig. 12. While the central values are indistinguishable, the distributions are much broader for the two larger masses, a consequence of the wiggles mentioned in Sec. III C. We include all four of them for our final determination of r_0/r_1.

Furthermore, we perform joint fits combining different light quark masses. Namely, we use the parametrization of r_0/r_1 evaluated at the actual ensemble parameters in our study, or at subsets thereof. For r_1/r_2 we exclusively use joint fits and combine the smoothened r_1/a data with the direct r_2/a data. We start the joint fits with weighted averages as above and employ fits linear and quadratic in $(a/r_0)^2$, where we neglect explicit light quark mass dependence. Again, for r_0/r_1 and the linear fits in $(a/r_0)^2$, we vary $\beta_{\min} \in \{6.72, 6.3\}$ and for the quadratic fits in $(a/r_0)^2$, we vary $\beta_{\min} \in \{6.3, 6.0\}$. For r_1/r_2, we use $\beta_{\min} = 6.72$, using only linear fits in $(a/r_0)^2$. For either, we use $\beta_{\max} \in \{7.28, 7.0\}$. We additionally supplement the fits with terms linear and quadratic in the m_l/m_s-ratio, and furthermore, we also repeat these fits, adding a term proportional to the m_l/m_s-ratio that survives in the continuum limit. At this stage, we perform the fits with either the sea strange quark mass of the ensemble or with the tuned strange quark mass given in Table I, doubling the amount of fits. On top, we choose either $\alpha = \alpha_b \equiv g_0^2/(4\pi u_0^4)$ or $\alpha = 1$, again doubling the amount of fits. The fit functions are given in Eqs. (4.4)–(4.11). In order to get the continuum contribution due to the terms proportional to m_l/m_s that survive in the continuum, we substitute the values for m_l/m_s by expressions using the neutral or charged pion masses and the average squared kaon mass, respectively. For this, we use that in the isospin limit, we have, using the Gell-Mann–Oakes–Renner (GMOR) relation [98],

$$M_\pi^2 = 2m_l B_0, \qquad M_K^2 = (m_l + m_s)B_0, \tag{4.12}$$

where B_0 is a low-energy constant related to the chiral condensate in the chiral limit [98] that cancels in the ratio. We thus get from the GMOR relation,

$$m_l/m_s = 1/(2M_K^2/M_\pi^2 - 1). \tag{4.13}$$

Inserting Particle Data Group (PDG) [99] values we can fix the m_l/m_s-ratio in the continuum. We use the average squared kaon mass, $2M_K^2 = M_{K^\pm}^2 + M_{K^0}^2$, and either the neutral or charged pion mass squared, $M_{\pi^\pm}^2$ or $M_{\pi^0}^2$, yielding

$$m_l/m_s|_{M_\pi^2 = M_{\pi^\pm}^2} = 0.04128, \tag{4.14}$$

$$m_l/m_s|_{M_\pi^2 = M_{\pi^0}^2} = 0.03851. \tag{4.15}$$

We show the data together with the respective continuum results in Fig. 13.

All of these combinations lead to about 100 trial fits whose results, together with the ones previously discussed, are shown in the histograms of Fig. 14. The blue lines and bands correspond to the mean and the standard deviation of the distributions. We also show a box plot[17] together with the histograms. The gray bands correspond to the published $(2+1)$-flavor values [11,16] for r_0/r_1 and r_1/r_2, respectively. Because the distribution for r_0/r_1 is fairly similar to a Gaussian, the width appears to be an appropriate estimate of the error; cf. Fig. 34 in Appendix B 5. However, the distribution for r_1/r_2 does not resemble a Gaussian and is, at least, bimodal. Even so, the confidence interval derived from the cumulative distribution function of the histogram is quite similar to the one from a Gaussian interpretation. We obtain the best Akaike information criterion (AIC) [100–102] with weighted averages of all included

[17]The box plots use the standard, yet arbitrary, definition where the box extends from the first quartile (Q1) to the third quartile (Q3) of the data, with the dashed line at the median. The whiskers extend from the box by 1.5× the interquartile range (IQR). Flier points are those past the end of the whiskers. They are sometimes considered outliers to be omitted; however, we do include them as regular data points. In all of our results the mean (solid lines) and the median in the box lie close to one another, and the median lies within the box supporting the decision to take the mean as our final result. Furthermore, the standard deviation in our results (areas) and the IQR coincide very well supporting the decision to take the former as our final error estimate.

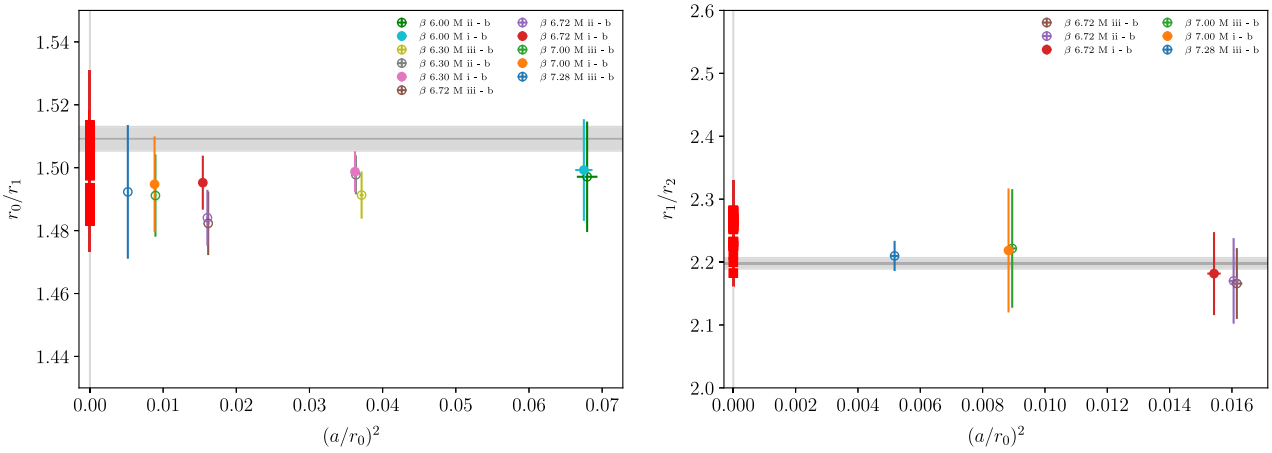

FIG. 13. Continuum results (red) and smoothened data (other colors) for the ratios r_0/r_1 (left) or r_1/r_2 (right) as functions of $(a/r_0)^2$, using bare links. The gray solid line and band show the published $(2+1)$-flavor QCD values [11,16] for r_0/r_1 and r_1/r_2, respectively. The corresponding plots for smeared links are shown in Fig. 31 of Appendix B 5.

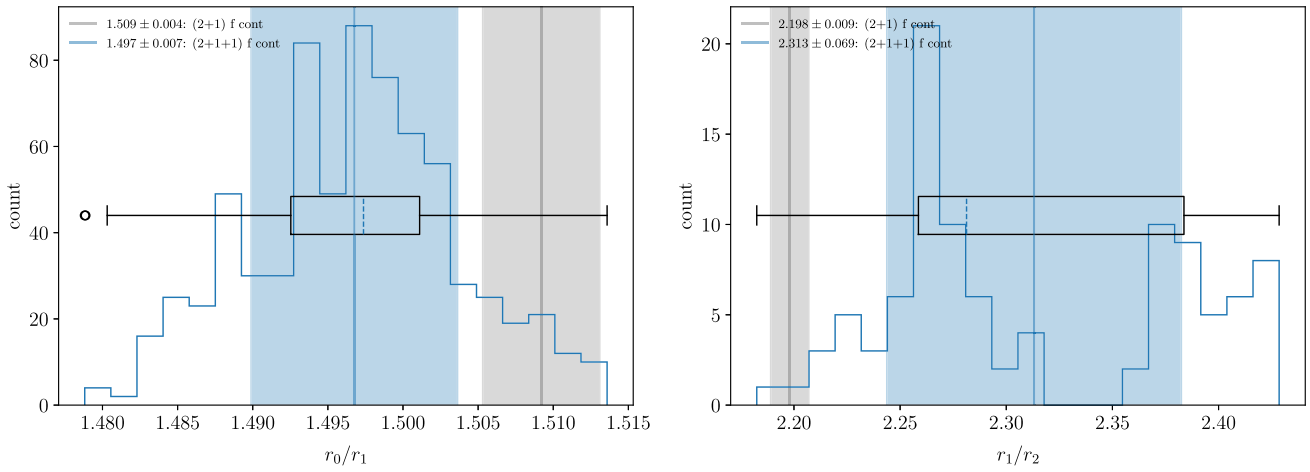

FIG. 14. Histogram of the continuum extrapolations for the ratios r_0/r_1 and r_1/r_2 using the *Ansätze* discussed in the text. The box plots are explained in a footnote on p. 28. We take the mean and the standard deviation of the respective distributions as our final value and uncertainty. The gray solid line and band show published $(2+1)$-flavor values [11,16] for r_0/r_1 and r_1/r_2, respectively. The distribution of the errors is shown in Fig. 34 of Appendix B 5.

ensembles, both for r_0/r_1 or r_1/r_2, both for bare- or smeared-link data, and both for separate fits at any of the light quark masses—if applicable—or joint fits of the different masses. For r_0/r_1, these weighted averages scatter within the central 1σ interval of the distribution. For r_1/r_2, however, they are very close to the $(2+1)$-flavor QCD result, while the distribution of the fits yields a significantly larger central value. Given that there are hints that r_1/r_2 for $\beta = 6.72$ could be a bit on the low side due to discretization artifacts, this situation could be cleared up once a correction beyond the tree level becomes available in $(2+1+1)$-flavor QCD as well. Our final continuum results for the ratios read

$$r_0/r_1 = 1.4968 \pm 0.0069, \tag{4.16}$$

$$r_1/r_2 = 2.313 \pm 0.069. \tag{4.17}$$

B. The scales r_0 and r_1 and the string tension

We repeat the analysis via the joint fits described earlier on p. 26 for the two scales $r_{0,1}$, or for the string tension σ. To be more precise, we extrapolate $a_{f_{p4s}}(r_{0,1}/a)$, as well as $\sqrt{\sigma r_0^2}$ for the two choices of the coefficient A of $1/R$, discussed in Sec. III B as functions of $(a/r_0)^2$. The parametrizations are evaluated at the actual ensemble parameters in our study, or at subsets of these. We show the data together with the respective continuum results in Figs. 15 and 16, respectively.

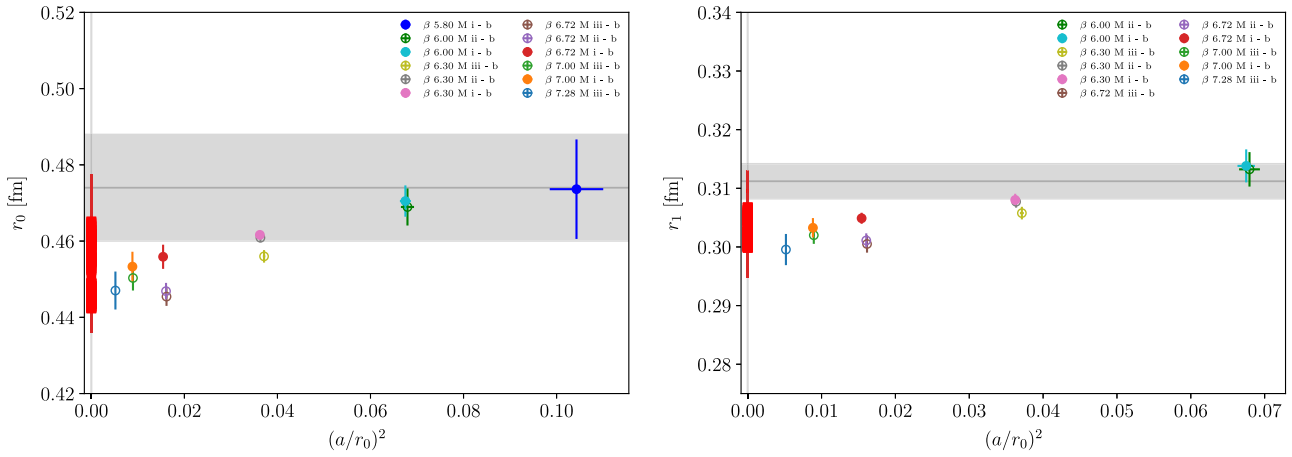

FIG. 15. Continuum results (red) and smoothened data (other colors) for $a_{f_{p4s}} r_{0,1}/a$ are shown in the left or right columns, respectively, as functions of $(a/r_0)^2$, using bare links. The gray solid line and band show the published $(2+1+1)$-flavor QCD values [25,34] for r_0 and r_1, respectively. The corresponding plots for smeared links are shown in Fig. 32 of Appendix B 5.

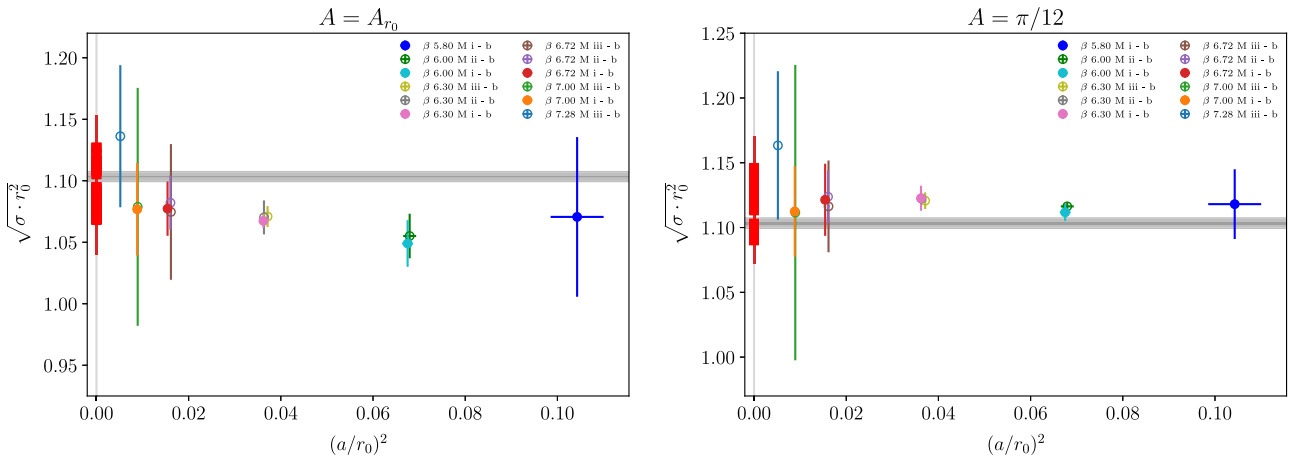

FIG. 16. Continuum results (red) and smoothened data (other colors) for $\sqrt{\sigma r_0^2}$ assuming two different coefficients A for the Coulomb term are shown in the left or right columns, respectively, as functions of $(a/r_0)^2$, using bare links. The gray solid line and band show the published $(2+1)$-flavor QCD value [14]. The corresponding plots for smeared links are shown in Fig. 33 of Appendix B 5.

The histograms of the results are shown in Figs. 17 and 18. For the physical mass ensembles, the products $a_{f_{p4s}}(r_{0,1}/a)$ approach their respective continuum limits from above, with clearly monotonic behavior throughout the scaling window. In the case of r_0, the best AIC is reached for the bare-link result with quadratic x dependence, or for smeared-link result with weighted averages, in both cases for the full β range. In the case of r_1, the best AIC is reached for the bare- or smeared-link results with quadratic x dependence for the full β range. Fits with quadratic x dependence usually yield rather low continuum results in the first quartile, while fits in the fourth quartile are obtained by omitting smaller β values, and are substantially disfavored in terms of AIC. On the other hand, for the string tension, weighted averages are favored in terms of AIC and close to the center of each distribution. The distributions of errors suggest that the width of the histograms are good estimates of the uncertainty; cf. Fig. 35 in Appendix B 5.

Both histograms of $\sqrt{\sigma r_0^2}$ have a more pronounced tail towards lower values. The blue and orange lines and bands correspond to the mean and the standard deviation of the distributions using the two different A values, respectively. The gray band corresponds to the published $(2+1)$-flavor QCD result [14] for $\sqrt{\sigma r_0^2}$, which had been determined in simultaneous fits of r_0/a and $a\sqrt{\sigma}$. This result is bracketed by our two calculations and conceptually closer to our analysis with $A = A_{r_0}$; after taking into account the lower value for r_0 in our analysis, see Fig. 19, the results for σ are in perfect agreement.

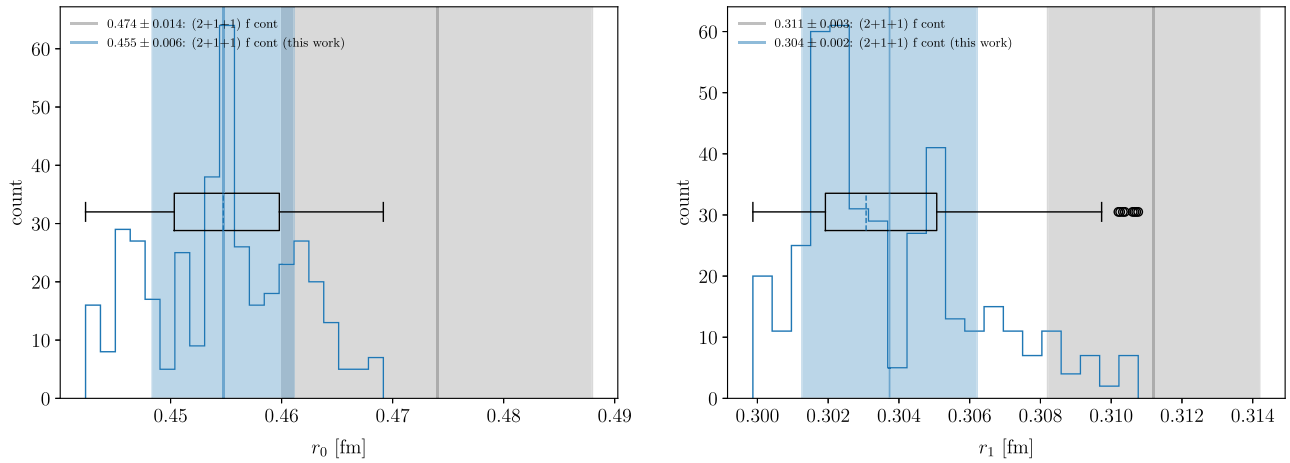

FIG. 17. Histogram of the continuum extrapolations for the individual scales $(r_{0,1}/a)a_{f_{p4s}}$ using the *Ansätze* discussed in the text. The box plots are explained in the text on p. 28. We take as our final value and uncertainty the mean and the standard deviation of the respective distribution. The gray bands corresponds to the literature values [25,34] for r_0 and r_1, respectively. The distribution of the errors is shown in Fig. 35 of Appendix B 5.

Our final results for the scales themselves, and the string tension, are given by the mean and standard deviation of the respective distributions of our fit results. Finally, we may combine the continuum limits of r_1/r_2 and r_1 adding errors in quadrature, i.e., Eqs. (4.17) and (4.19), to obtain our final result for r_2. The corresponding procedure, i.e., combining the continuum limits of r_0/r_1 and r_1, i.e., Eqs. (4.16) and (4.19), and adding the errors in quadrature, yields a consistent result for r_0 with smaller errors, namely 0.4546 ± 0.0043 fm. Our final results read

$$r_0 = 0.4547 \pm 0.0064 \text{ fm}, \tag{4.18}$$

$$r_1 = 0.3037 \pm 0.0025 \text{ fm}, \tag{4.19}$$

$$r_2 = 0.1313 \pm 0.0041 \text{ fm}, \tag{4.20}$$

$$\sqrt{\sigma r_0^2} = 1.077 \pm 0.016 \quad (A = A_{r_0}), \tag{4.21}$$

$$\sqrt{\sigma r_0^2} = 1.110 \pm 0.016 \quad (A = \pi/12). \tag{4.22}$$

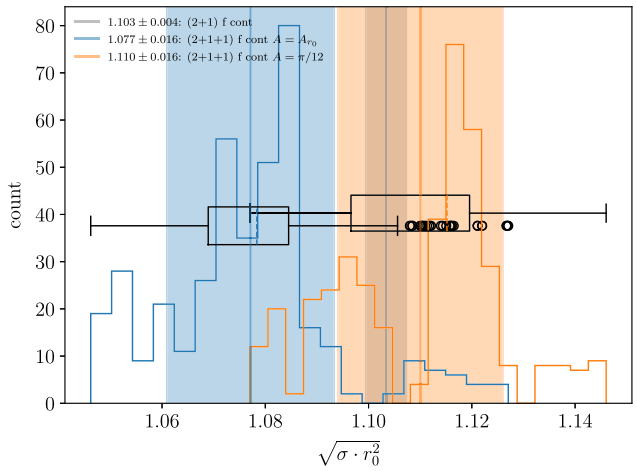

FIG. 18. Histogram of the continuum extrapolations for the string tension using the *Ansätze* discussed in the text. The box plots are explained in the text on p. 28. The blue and orange lines and bands correspond to the mean and the standard deviation of the distributions using the two different A values, respectively. The gray band corresponds to the $(2 + 1)$-flavor value [14] for $\sqrt{\sigma r_0^2}$. The distribution of the errors is shown in Fig. 36 of Appendix B 5.

The decreasing trend in the scale r_1/a in Fig. 15 is similar to the one already discussed in Fig. 6 and is reflected in the continuum value of r_1 that is lower than the published value, namely $r_1 = 0.3112(30)$ fm [34]. A similar statement holds for r_0. The difference between the results in Eqs. (4.21) and (4.22) must be regarded as a measure of the inherent uncertainty of defining the string tension in QCD in an intermediate regime between Coulomb behavior at small distances and string breaking at large distances.

C. Summary plot

We finally have all building blocks available to achieve a curve collapse and generate Fig. 1 in Sec. I. For all ensembles we use the static energy results from the $N_{\text{st}} = 2$ fits described in Sec. II as a function of the tree-level corrected distance $R = r_I/a$ described in Sec. III A. We convert both the dimensionless static energy $E = aE_0(\boldsymbol{r}, a)$ and the distance R to r_0 units, i.e., $(r_0/a)E$ as a function of $(a/r_0)R$. We replace r_0/a by $(r_1/a)(r_0/r_1)$ using Eq. (4.16) and r_i/a from Table VII, if the latter has a smaller error than the former. We use bare-link rather than smeared-link results for the scales. Next, we normalize all

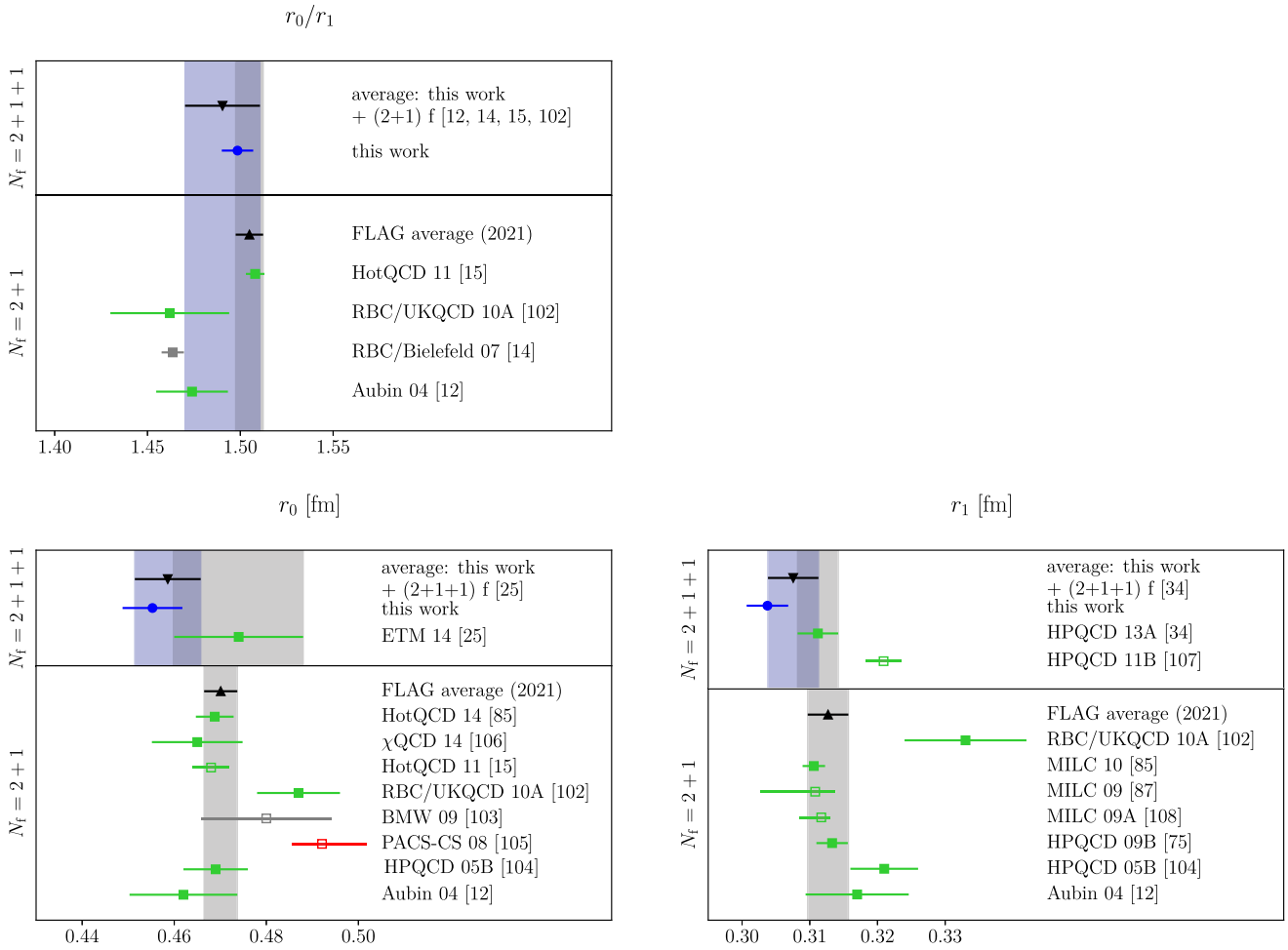

FIG. 19. Comparison plots for r_0/r_1, r_0, and r_1 with the FLAG 2021 averages (gray bands) [96]. Multiple errors on inputs are added in quadrature. References to results entering the FLAG averages are shown in the plots, and we also include $(2+1)$-flavor results (gray symbols) for r_0/r_1 [14] and r_0 [104] that are omitted from the FLAG report. The blue bands constitute our "new" averages explained in the text. See Refs. [12,14,15,25,34,75,85,87,102–108].

results to zero at $(a/r_0)R = 1$ (using Eq. (3.5) to interpolate in a $\pm 25\%$ interval). Then, we combine our normalized continuum results from the bare-link data for $R \leq 4$ and the smeared-link data for $R > 4$ and convert the combined result $(r_0/a)E$ as the ordinate and $(a/r_0)R$ as the abscissa to physical units, using the continuum result for r_0 from Eq. (4.18). This is the set of static-energy results shown in Fig. 1.

D. Comparison to published results

In Fig. 19, we compare our $(2+1+1)$-flavor QCD results for the ratio r_0/r_1 and for the scales $r_{0,1}$ to earlier $(2+1)$- and $(2+1+1)$-flavor QCD results and the corresponding FLAG 2021 average [96]. For the ratio r_0/r_1, the $(2+1)$-flavor FLAG value has a $\chi^2/\text{d.o.f.} \approx 4.741/2$ [degrees of freedom (d.o.f.)]. Under the assumption of the decoupling of the charm quark, we compute a new weighted average of our result, the known $(2+1)$-flavor results [12,15,103] and the result [14] omitted in the FLAG report that encompasses the $(2+1)$-flavor FLAG average and most of its uncertainty band; however, it comes with a slightly larger uncertainty itself. The $\chi^2/\text{d.o.f.} \approx 14.800/3$ increases slightly but not significantly when including our result and the one [14] omitted by FLAG. The change in average is from 1.5049(74) to 1.490(20).

For the scales $r_{0,1}$, the $(2+1)$-flavor FLAG values, $r_0 = 0.4701(36)$ fm and $r_1 = 0.3127(30)$ fm, have a $\chi^2/\text{d.o.f.} \approx 3.790/4 = 0.948$ and $\chi^2/\text{d.o.f.} \approx 7.281/4 = 1.820$, respectively. The $(2+1+1)$-flavor results consist of one determination each: $r_0 = 0.474(14)$ fm [25] (with twisted-mass Wilson sea quarks) and $r_1 = 0.3112(30)$ fm [34] (with a subset of the ensembles used here). Performing a weighted average of the respective determinations with our results yields $r_0 = 0.4586(71)$ fm with $\chi^2/\text{d.o.f.} \approx 1.472/1$ and $r_1 = 0.3076(37)$ fm with $\chi^2/\text{d.o.f.} \approx 3.021/1$.

V. CHARMED LOOPS

As anticipated in the Introduction, now that we have data for the static energy in $(2+1+1)$-flavor QCD, it is possible to study the effect of the massive charm loops. We review the weak-coupling result for N_f massless sea quarks in Sec. V A and discuss the corrections from a massive sea quark in Sec. V B. We collect all relevant two-loop formulas in Appendix C. Finally, in Sec. V C, we conclude the discussion with the explicit, quantitative comparison of our results with perturbation theory, either with finite-quark-mass effects at the two-loop level, or with $(2+1)$-flavor QCD, i.e., without charm at all. We see a clear difference in the lattice-QCD data with and without charm, and the comparison with perturbation theory validates the expected decoupling.

A. Static energy and force in perturbation theory

Similarly to Eqs. (2.2) and (2.3) in lattice gauge theory, the static energy is related to the large time behavior of the real-time rectangular Wilson loop of spatial length r and temporal length t [1,109–111],

$$E_0(r) = \lim_{t\to\infty} \frac{\mathrm{i}}{t} \ln \left\langle \mathrm{tr}\mathcal{P} \exp\left[\mathrm{i}g \oint_{r\times t} \mathrm{d}z^\mu A_\mu(z) \right] \right\rangle, \tag{5.1}$$

where $\mathcal{P}$ stands for the path ordering of the color matrices, g is the QCD gauge coupling ($\alpha_s = g^2/(4\pi)$), and A_μ are the SU(3) gauge fields, which are time ordered. In nonsingular gauges, like the covariant gauges and the Coulomb gauge, the Wilson lines at equal initial and final time do not contribute to the energy and may be ignored or replaced with any initial and final state that overlaps with the ground state. The static energy is, up to a constant shift, a physical observable, hence, gauge invariant and renormalization scheme and scale independent.

At short distances, i.e., when $r\Lambda_{\mathrm{QCD}} \ll 1$, it holds that $\alpha_s(1/r) \ll 1$ and $E_0(r)$ may be expanded as a series in α_s. In the following of this section, we will restrict ourselves to the case of massless sea quarks. The perturbative expansion of $E_0(r)$ has then the form

$$\begin{aligned} E_0(r) = \Lambda - \frac{C_F\alpha_s}{r}(1 + \#\alpha_s + \#\alpha_s^2 + \#\alpha_s^3 \ln\alpha_s \\ + \#\alpha_s^3 + \#\alpha_s^4 \ln^2\alpha_s + \#\alpha_s^4 \ln\alpha_s + \ldots), \end{aligned} \tag{5.2}$$

where Λ is a constant of mass dimension one and the # stand for the numerical coefficients that have been analytically computed so far (some of them are given in Appendix C 1). It is precisely because the expansion (5.2) is known to high order, that fitting the static energy computed with lattice QCD to (5.2) has the potential to provide an accurate determination of α_s.

Up to two loops, the only scale that sets the running of the strong coupling constant is $1/r$. Starting from three loops, however, another scale contributes to the static energy, it is the energy scale α_s/r [3]. Because this scale is much smaller than $1/r$, it may be called the ultrasoft scale, and the latter, the soft scale. Ultrasoft gluons may be emitted by static quark-antiquark pairs when changing their color configuration from a color singlet to a color octet.

Soft and ultrasoft effects are conveniently factorized in an effective field theory framework [4,5],

$$E_0(r) = \Lambda + V(r,\nu,\mu_{\mathrm{us}}) + \delta_{\mathrm{us}}(r,\nu,\mu_{\mathrm{us}}), \tag{5.3}$$

where $V(r,\nu,\mu_{\mathrm{us}})$ contains all soft contributions and can be identified with the color-singlet static potential, and $\delta_{\mathrm{us}}(r,\nu,\mu_{\mathrm{us}})$ encodes the ultrasoft contributions. The scale ν is the renormalization scale of the strong coupling constant. It is typically of the order of the soft scale $1/r$. The energy scale $1/r \gtrsim \mu_{\mathrm{us}} \gtrsim \alpha_s/r$ is a factorization scale separating soft from ultrasoft modes.

While the static energy is up to a constant shift finite, the functions $V(r,\nu,\mu_{\mathrm{us}})$ and $\delta_{\mathrm{us}}(r,\nu,\mu_{\mathrm{us}})$ are not. Indeed, the $\ln\alpha_s$ terms appearing in the expansion (5.2), first at order α_s^4, are remnants of cancellations happening between infrared divergences affecting the potential $V(r,\nu,\mu_{\mathrm{us}})$ and ultraviolet divergences affecting $\delta_{\mathrm{us}}(r,\nu,\mu_{\mathrm{us}})$:

$$\ln\alpha_s = \ln\frac{\mu_{\mathrm{us}}}{1/r} + \ln\frac{\alpha_s/r}{\mu_{\mathrm{us}}}. \tag{5.4}$$

The potential satisfies renormalization group equations that have been determined and solved up to subleading logarithmic accuracy [112,113]. This means that all logarithms of the form $\alpha_s^{3+n}\ln^n(\mu_{\mathrm{us}}r)$ and $\alpha_s^{4+n}\ln^n(\mu_{\mathrm{us}}r)$ entering the potential have been computed. The two-loop expression of the static potential (energy) supplemented by the logarithms $\alpha_s^{3+n}\ln^n(\mu_{\mathrm{us}}r)$ ($\alpha_s^{3+n}\ln^n\alpha_s$) is said to provide the static potential (energy) at next-to-next-to-leading logarithmic accuracy (N^{2}LL). The three-loop expression of the static potential (energy) supplemented by the logarithms $\alpha_s^{4+n}\ln^n(\mu_{\mathrm{us}}r)$ ($\alpha_s^{4+n}\ln^n\alpha_s$) is said to provide the static potential (energy) at next-to-next-to-next-to-leading logarithmic accuracy (N^{3}LL).

In lattice regularization, the constant Λ in Eq. (5.3) accounts for the linear divergence of the self energy. In dimensional regularization the linear divergence vanishes but the constant Λ encodes a renormalon of order Λ_{QCD} that cancels against a renormalon of the same order in the color-singlet static potential [6,7]. The renormalon in the static potential is responsible for the poor convergence of the perturbative expansion of $E_0(r)$. The poor convergence of the static energy may be treated by subtracting the renormalon of the static potential in a suitable renormalon subtraction scheme and reabsorbing it into a redefinition of Λ [65]. Another way to enforce the renormalon cancellation in the perturbative expansion of the static energy is by computing the force [64] defined in Eq. (1.1). The force is

free of renormalons and therefore well behaved as an expansion in α_s. One then recovers the static energy by integrating back over the quark-antiquark distance r,

$$E_0(r) = \int_{r^*}^{r} \mathrm{d}r'\, F(r') + \text{const.} \tag{5.5}$$

The distance $r^* < r$ is arbitrary and contributes only with an additive constant. This constant can be reabsorbed into an additive shift when comparing with lattice data. Equation (5.5) effectively amounts to a rearrangement of the perturbative series enforcing the renormalon cancellation [65]. The integral in Eq. (5.5) can be computed (numerically) while setting the renormalization scale ν at $1/r$. At two-loop accuracy the static force with N_f massless quarks reads [68]

$$\begin{aligned} F^{(N_f)}(r,\nu=1/r) = \frac{C_F\alpha_s^{(N_f)}(1/r)}{r^2}\Bigg\{1 + \frac{\alpha_s^{(N_f)}(1/r)}{4\pi}\left[a_1^{(N_f)} + 2\gamma_E\beta_0^{(N_f)} - 2\beta_0^{(N_f)}\right] \\ + \left(\frac{\alpha_s^{(N_f)}(1/r)}{4\pi}\right)^2\left[a_2^{(N_f)} + \left(\frac{\pi^2}{3} + 4\gamma_E^2\right)\left(\beta_0^{(N_f)}\right)^2 + \gamma_E\left(4a_1^{(N_f)}\beta_0^{(N_f)} + 2\beta_1^{(N_f)}\right)\right. \\ \left. - 4\left(a_1^{(N_f)} + 2\gamma_E\beta_0^{(N_f)}\right)\beta_0^{(N_f)} - 2\beta_1^{(N_f)}\right]\Bigg\}. \end{aligned} \tag{5.6}$$

Resumming the ultrasoft leading logarithms in the expression of the static potential yields the expression of the force at N^{2}LL accuracy [68],

$$\begin{aligned} F^{(N_f)}(r,\nu=1/r) = \frac{C_F\alpha_s^{(N_f)}(1/r)}{r^2}\Bigg\{1 + \frac{\alpha_s^{(N_f)}(1/r)}{4\pi}\left[a_1^{(N_f)} + 2\gamma_E\beta_0^{(N_f)} - 2\beta_0^{(N_f)}\right] \\ + \left(\frac{\alpha_s^{(N_f)}(1/r)}{4\pi}\right)^2\left[a_2^{(N_f)} + \left(\frac{\pi^2}{3} + 4\gamma_E^2\right)\left(\beta_0^{(N_f)}\right)^2 + \gamma_E\left(4a_1^{(N_f)}\beta_0^{(N_f)} + 2\beta_1^{(N_f)}\right)\right. \\ \left. - 4\left(a_1^{(N_f)} + 2\gamma_E\beta_0^{(N_f)}\right)\beta_0^{(N_f)} - 2\beta_1^{(N_f)}\right] + \left(\frac{\alpha_s^{(N_f)}(1/r)}{4\pi}\right)^2\left[-\frac{a_3^L}{2\beta_0^{(N_f)}}\ln\left(\frac{\alpha_s^{(N_f)}(\mu_{us})}{\alpha_s^{(N_f)}(1/r)}\right)\right]\Bigg\}, \end{aligned} \tag{5.7}$$

where we have set the ultrasoft scale to be

$$\mu_{us} = \frac{C_A\alpha_s^{(N_f)}(1/r)}{2r}, \tag{5.8}$$

which is the difference between the Coulomb potential in the adjoint and in the fundamental representation of SU(3). The coefficients $a_1^{(N_f)}$, $a_2^{(N_f)}$, a_3^L, $\beta_0^{(N_f)}$, and $\beta_1^{(N_f)}$ can be found in Appendix C 1; γ_E is the Euler–Mascheroni constant.

B. Charm quark mass effects in perturbation theory

Effects due to the finite mass of a heavy quark, while keeping N_f quarks massless, can be cast into a correction $\delta V_m^{(N_f)}(r)$ to be added to the static potential or energy. This correction has been computed at $O(\alpha_s^2)$ in Ref. [114] and at $O(\alpha_s^3)$ in Refs. [115–117]. For a typo-free summary, see Ref. [118] and Appendix C 2. In our case of interest, the relevant massive quark is the charm quark.

The expression for the static energy that we use in this work for comparison to lattice simulations with $N_f = 3$ nearly massless quarks and a charm quark of mass $m = m_c = 1.28$ GeV is

$$E_{0,m}^{(N_f)}(r) = \int_{r^*}^{r} \mathrm{d}r'\, F^{(N_f)}(r') + \delta V_m^{(N_f)}(r) + \text{const}, \tag{5.9}$$

where we have explicitly indicated for each quantity the number of massless quarks. In particular, in the right-hand side all couplings are computed with N_f massless flavors. The expression of $F^{(N_f)}(r)$ at two loops is given in Eq. (5.6), and the expression of $F^{(N_f)}(r)$ at N^{2}LL accuracy is given in Eq. (5.7). The expression of $\delta V_m^{(N_f)}(r)$ up to two-loop accuracy is given by

$$\delta V_m^{(N_f)}(r) = \delta V_m^{(N_f),[2]}(r,\nu) + \delta V_m^{(N_f),[3]}(r,\nu), \tag{5.10}$$

where ν is the renormalization scale, and $\delta V_m^{(N_f),[2]}(r,\nu)$ and $\delta V_m^{(N_f),[3]}(r,\nu)$ are the one- and two-loop corrections, given

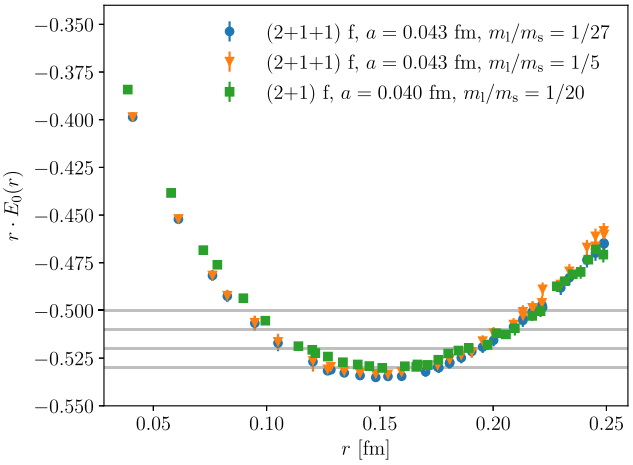

FIG. 20. The dimensionless quantity $rE_0(r)$ for two different $(2+1+1)$-flavor ensembles using different light quark masses and one $(2+1)$-flavor ensemble of similar lattice spacing. The latter has been matched to the $(2+1+1)$-flavor ensemble of the similar light quark mass ratio at large distances.

in Eqs. (C10) and (C11), respectively. The renormalization scale of the coupling is set to be $1/r$. The integral over the force $F^{(N_f)}(r)$ is performed numerically while keeping α_s running at three-loop accuracy using the RunDec package [119–121].

The static energy with a massive quark and N_f massless quarks reduces to the static energy with N_f massless quarks, $E_0^{(N_f)}(r)$, for $m \gg 1/r$, and it reduces to the static energy with N_f+1 massless quarks, $E_0^{(N_f+1)}(r)$, for $m \ll 1/r$. This is a consequence of the decoupling of the static potential discussed in Appendix C 2.

Finally, we remark that since the finite mass corrections to the static potential, $\delta V_m^{(N_f)}(r)$, are known only up to two loops, the available three-loop information on the force, $F^{(N_f)}(r)$, cannot be used in a consistent manner. In particular, adding the three-loop correction to $F^{(N_f)}(r)$ without the three-loop correction to $\delta V_m^{(N_f)}(r)$ would lead to a violation of the decoupling theorem in the static energy at order α_s^4.

C. Charm quark mass effects on the lattice

In this section, we study how a finite charm quark mass affects the determination of the static energy on lattices with $(2+1+1)$ flavors. In particular, we focus on the short distance behavior of the static energy and compare it with the expectation from perturbation theory, i.e., Eq. (5.9). In principle, we could use this comparison to extract α_s, as this is the only free parameter (up to the constant shift) in Eq. (5.9). For the argument given at the end of the previous section, this would lead to a determination of α_s accurate at two loops. A two-loop determination of α_s would, however, not be competitive with respect to existing three-loop determinations based on $(2+1)$-flavor lattices [17,68,70,122]. Hence, we will refrain from a determination of α_s in this work, while we will limit ourselves to some observations on the impact of finite charm quark mass effects on the static energy. This is a first time study of this kind of effects.

In Fig. 20, we show $(2+1)$-flavor and $(2+1+1)$-flavor lattice data for $rE_0(r)$,[18] which correspond to different discretizations and to light quark mass over strange quark mass ratios $m_l/m_s = 1/20$ and $m_l/m_s = 1/27$, respectively. For the $(2+1+1)$-flavor data we use the scale $a_{f_{p4s}}$ in Table I to convert the abscissa to physical units; for the $(2+1)$-flavor data, we use the published value $r_1/a = 7.690(58)$ combined with the published value of r_1 in Eq. (3.1), both from Ref. [16]. We add a mass independent constant to the $(2+1+1)$-flavor $E_0(r)$ such that the shifted data at physical mass (in blue color) are rather flat in the range of interest to facilitate the visualization of the small finite mass effects that we are investigating. We additionally show another $(2+1+1)$-flavor data set (in orange color) with larger light quark mass $m_l/m_s = 1/5$, whose data set has not been shifted relative to the physical one. Therefore, the difference between the two $(2+1+1)$-flavor data sets is due to the different light quark masses. We match the $(2+1)$-flavor data (in green color) to the $(2+1+1)$-flavor data of the similar m_l/m_s-ratio, whose additive shift is different due to the difference in discretizations, at large distances, $r \gg 1/m_c \sim 0.15$ fm, where they must agree up to a constant due to the decoupling of the charm quark. This matching of the $(2+1)$-flavor data to the $(2+1+1)$-flavor data is done by minimizing their difference over the range $r \in [0.18, 0.27]$ fm and by varying the range to estimate the matching error. This corresponds to a relative shift of the $(2+1)$-flavor data compared to the $(2+1+1)$-flavor data by an amount of 0.028 ± 0.001 at $r = 0.15$ fm. The difference in the light quark mass between the $(2+1)$-flavor data and the $(2+1+1)$-flavor data is smaller than the one between the two sets of $(2+1+1)$-flavor data. Since the latter are hardly distinguishable, we deduce that the light quark mass difference should be irrelevant in this entire range and that the difference between the $(2+1)$-flavor data and the $(2+1+1)$-flavor data is due to the dynamical charm quark in the sea. The effect of the dynamical charm is therefore significant and visible in the data.

Comparison between $(2+1)$-flavor and $(2+1+1)$-flavor lattice data using different ensembles with $m_l/m_s = 1/5$ (the β `7.28 M iii` ensemble compared to two

[18]We prefer to show $rE_0(r)$ rather than $E_0(r)$ because $rE_0(r)$ is a dimensionless quantity. Moreover, it has no Coulomb singularity, which facilitates plotting and comparisons.

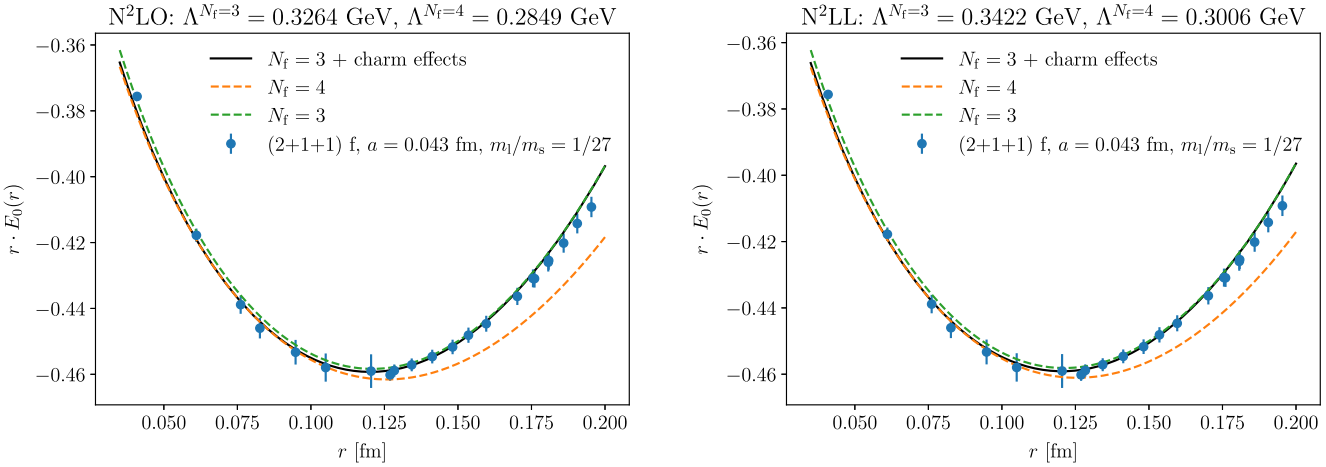

FIG. 21. Comparison of the $(2+1+1)$-flavor data with curves obtained from different perturbative expressions of the static energy times the distance. Left: in black, green, and orange we show $rE^{(3)}_{0,m}(r)$, $rE^{(3)}_0(r)$, and $rE^{(4)}_0(r)$, respectively. The perturbative curves have been obtained from the static force at two loops [next-to-next-to-leading order (N^{2}LO)], Eq. (5.6), using three-loop running of α_s. Charm mass effects have been included in the black curve at two-loop accuracy using $m_c^{\overline{\rm MS}}(m_c^{\overline{\rm MS}}) = 1.28$ GeV. Right: as in the left panel but at N^{2}LL accuracy, i.e., the force is given by Eq. (5.7).

$(2+1)$-flavor ensembles with $r_1/a = 10.653(60)$ or 8.905 (60) from Ref. [11]) gives qualitatively similar results.

As discussed in Sec. V B and Appendix C 2, the effective number of active flavors that enters the running of α_s and the static energy changes at different distances with m_c fixed. At large distance, $r \gg 1/m_c$, the charm quark decouples, and in this region the static energy behaves effectively as with three massless flavors. At short distance, $r \ll 1/m_c$, the charm quark contributes as an active massless flavor, and thus, in this region the static energy behaves effectively as with four massless flavors. One expects to see this behavior realized by the $(2+1+1)$-flavor lattice data of the static energy. In the following, we will superimpose Fig. 37 to the lattice data and verify that this is indeed the case in the distance region for which we expect perturbation theory to work: $r < 1/\Lambda_{\rm QCD} \approx 0.2$ fm.

In order to compare with perturbation theory, we need first to determine $\Lambda_{\overline{\rm MS}}$.[19] We determine $\Lambda^{(N_f=3)}_{\overline{\rm MS}}$ by fitting Eq. (5.9) to the physical $(2+1+1)$-flavor ensemble. We leave out data at $r/a = 1$ from all the fits and vary the fit range up to $r \approx 0.19$ fm using $m_c^{\overline{\rm MS}}(m_c^{\overline{\rm MS}}) = 1.28$ GeV and the three-loop running of α_s. To account for the residual discretization artifacts, see Fig. 3, we enlarge the error to 3‰ of the raw data at $r/a \le \sqrt{8}$, or to 1‰ of the raw data, otherwise. The numerical running of α_s and the conversion between the three-flavor and the four-flavor values of $\Lambda_{\overline{\rm MS}}$ is performed using the RunDec package [119–121].

[19]Although we do not attempt to give a precision extraction of α_s or $\Lambda_{\overline{\rm MS}}$, we need to determine a reference value and use it throughout the analysis.

The value of $\Lambda^{(N_f=3)}_{\overline{\rm MS}}$ that we obtain using the N^{2}LO expression of the force, Eq. (5.6), is $\Lambda^{(N_f=3)}_{\overline{\rm MS}} \approx 326$ MeV.[20]

The static energy at N^{2}LO, including N^{2}LO massive charm loop effects, is shown by the black curve in the left panel of Fig. 21. Lattice data are the blue dots. Omitting the data point at the smallest distance, we obtain $\chi^2_{\rm red} \approx 0.5$. We use $r \le 0.19$ fm. The static energy, Eq. (5.5), with four massless active flavors, $N_f = 4$, which is the orange dashed curve, is matched to the black curve at 0.08 fm to compensate for truncation effects of order α_s^4. It begins to deviate from the lattice data at distances $r \gtrsim 0.12$ fm. The static energy, Eq. (5.5), with three massless active flavors, $N_f = 3$, is shown by the green dashed curve. In this case no shift is performed to match with the black curves, as the two overlap exactly by construction at large distances. The green dashed curve shows a systematic overshooting of the data at distances $r \lesssim 0.12$ fm (with the exception of the first data point, corresponding to one lattice spacing, which is possibly affected by large discretization artifacts). The $(2+1+1)$-flavor lattice data behave therefore accordingly to the decoupling theorem. At large distance they are well described by the perturbative static energy with three

[20]This value is about 3.8% higher than the $(2+1)$-flavor determination of Ref. [17], yet still covered within the perturbative truncation error. Note that the determination in Ref. [17], based on $(2+1)$-flavor lattice data, is accurate up to three loops, although the central value is the same between two or three loops with leading ultrasoft resummation. If we compare, instead, the values for $r_1\Lambda^{(N_f=3)}_{\overline{\rm MS}}$, then we see a partial compensation between the smaller value of r_1 and the larger value of $\Lambda^{(N_f=3)}_{\overline{\rm MS}}$ in $(2+1+1)$-flavor QCD—the difference shrinks to the level expected from combined lattice uncertainties.

massless flavors and at short distance by the perturbative static energy with four massless flavors. The static energy with three massless flavors and one massive charm interpolates smoothly between these two curves and on the overall describes well the data. We have seen, indeed, in Fig. 20 that the lattice data are sensitive to finite charm mass effects in the intermediate region $r \sim 1/m_c$.

A similar analysis can be done using the N^{2}LL expression of the force, Eq. (5.7). We get, in this case, $\Lambda_{\overline{\rm MS}}^{(N_f=3)} \approx 342$ MeV.[21] As before, the black curve, which includes the charm mass effects, reproduces the data with $\chi^2_{\rm red} \approx 0.5$, while the orange dashed curve with four massless flavors deviates significantly from the data at $r \gtrsim 0.12$ fm, and the green dashed curve with three massless flavors overshoots the data at $r \lesssim 0.12$ fm, with the possible exception of the first data point. Again, we see that the lattice data reflect the expectations from the decoupling theorem, i.e., at large distance they are well described by the perturbative static energy with three massless flavors and at short distance by the perturbative static energy with four massless flavors, while the static energy with three massless flavors and one massive charm interpolates smoothly between these two curves and describes well the data.

VI. CONCLUSIONS

In this paper, we present results for the static energy in $(2+1+1)$-flavor QCD over a wide range of lattice spacings and several quark masses, including the physical quark mass. To gain better control of the statistical errors in the static energy at large distances, the calculations have been performed using bare links, or links after one level of HYP smearing. This enabled us to obtain reliable results for the static energy also at relatively large distances. We perform a simultaneous determination of the scales r_1 and r_0, as well as the string tension σ, and for the smallest three lattice spacings, we also determine the scale r_2. For the scales, direction-dependent discretization uncertainties dominate over statistical errors. Our values of r_1/a on the coarser lattices are marginally lower than previous ones from the MILC Collaboration [18,19] and have larger uncertainties due to the differences in the procedure for obtaining r_1/a. Our results on r_0/r_1 and $r_0\sqrt{\sigma}$ agree with published $(2+1)$-flavor results. On the other hand, our result for r_1/r_2 differs significantly from the value obtained in the $(2+1)$-flavor case [11], which is most likely due to the effect of the charm quark.

We study in detail the effect of the charm quark on the static energy by comparing our results on some of the finest two lattices with previously published $(2+1)$-flavor QCD results at similar lattice spacing. Significant influence of the different light quark masses can be ruled out. We have found that for $r > 0.2$ fm our results on the static energy agree with the $(2+1)$-flavor results, implying the decoupling of charm quark for these distances. For smaller distances, on the other hand, we find that the effect of the dynamical charm quark is noticeable. The behavior of the $(2+1+1)$-flavor lattice data for the static energy is well reproduced by the perturbative expression of the static energy incorporating the charm mass effects at two loops. This shows at a quantitative level how the $(2+1+1)$-flavor lattice data smoothly interpolate between the large distance region, where the charm quark decouples, and the short distance region, where the charm quark may be treated as massless.

A precision extraction of α_s from lattice QCD data of the static energy with $(2+1+1)$ flavors is at the moment problematic if data are included for distances around $1/m_c$. At such distances, as we have seen, finite charm mass effects have to be included in the fitting perturbative expression. Since these are known up to two loops, this is also the maximal precision one may obtain at present for the strong coupling from these data. The computation of finite charm-mass corrections to the static energy at three loops is certainly challenging.

ACKNOWLEDGMENTS

We thank the MILC Collaboration for allowing us to use of their $(2+1+1)$-flavor HISQ ensembles. The simulations were carried out on the computing facilities of the Computational Center for Particle and Astrophysics (C2PAP) in the project *Calculation of finite T QCD correlators* (pr83pu) and of the SuperMUC cluster at the Leibniz-Rechenzentrum (LRZ) in the project *The role of the charm-quark for the QCD coupling constant* (pn56bo), both located in Munich (Germany). This research was funded by the Deutsche Forschungsgemeinschaft (DFG, German Research Foundation) cluster of excellence "ORIGINS" ([123]) under Germany's Excellence Strategy EXC-2094-390783311. This research is supported by the DFG and the NSFC through funds provided to the Sino-German CRC 110 "Symmetries and the Emergence of Structure in QCD." R. L. D. is supported by the Ramón Areces Foundation, the INFN postdoctoral fellowship AAOODGF-2019-0000329, and the Spanish Grant MICINN: PID2019–108655GB-I00. Fermilab is managed by Fermi Research Alliance, LLC, under Contract No. DE-AC02-07CH11359 with the U.S. Department of Energy. P. P. is supported by the U.S. Department of Energy under Contract No. DE-SC0012704. A. V. is supported by the EU Horizon 2020 research and innovation programme, STRONG-2020 project, under Grant Agreement No. 824093. J. H. W.'s research is funded by the Deutsche Forschungsgemeinschaft (DFG, German Research Foundation)—Projektnummer 417533893/GRK2575 "Rethinking Quantum Field Theory." The lattice QCD calculations have been performed using the publicly

[21]This value is only about 1.1% away from, and therefore consistent inside uncertainties with, the N^{3}LL fit of Ref. [70], which found $\Lambda_{\overline{\rm MS}}^{(N_f=3)} \approx 338$ MeV by reanalyzing a subset of the $(2+1)$-flavor data.

available MILC code. The data analysis for the ground state extraction was performed using the R-base and NLME packages [81,82]. The data analysis for all further quantities was performed using Python3 [124–126] and the libraries GVAR [127], Matplotlib [128], NumPy [129–131], PANDAS [132,133], and SciPy [134]. V. L. and S. S. would like to thank Xavier Garcia i Tormo for discussions. S. S. would like to thank Florian M. Kaspar for discussions.

APPENDIX A: WILSON LINE CORRELATION FUNCTION AT DIFFERENT LEVELS OF GAUGE FIXING

As stated in Sec. II A in the body of this paper, different gauge-fixing schemes were unintentionally mixed during the simulations. On the one hand, we utilized the original scheme with a tolerance of $\epsilon = 2 \times 10^{-6}$ for the coarser ensembles with $\beta \leq 6.30$. On the other hand, we have employed a fixed number (320) of steps for the finer ensembles with $\beta \geq 7.00$. Lastly, we could use gauge-fixed ensembles for $\beta = 6.72$ with unphysical masses (β `6.72 M ii` or β `6.72 M iii`) with a tolerance of $\epsilon = 2 \times 10^{-6}$. However, for β `6.72 M i` we could use only a fraction of the ensemble gauge fixed with a tolerance of $\epsilon = 2 \times 10^{-6}$ and had to gauge fix the rest ourselves. Due to an initial misunderstanding, we used a prescription with a fixed number (320) of steps instead. These lead to slight deviations in the final gauge-fixing precision, as the procedure usually stopped O(1) steps before reaching the tolerance of $\epsilon = 2 \times 10^{-6}$ (usually less than 10% level

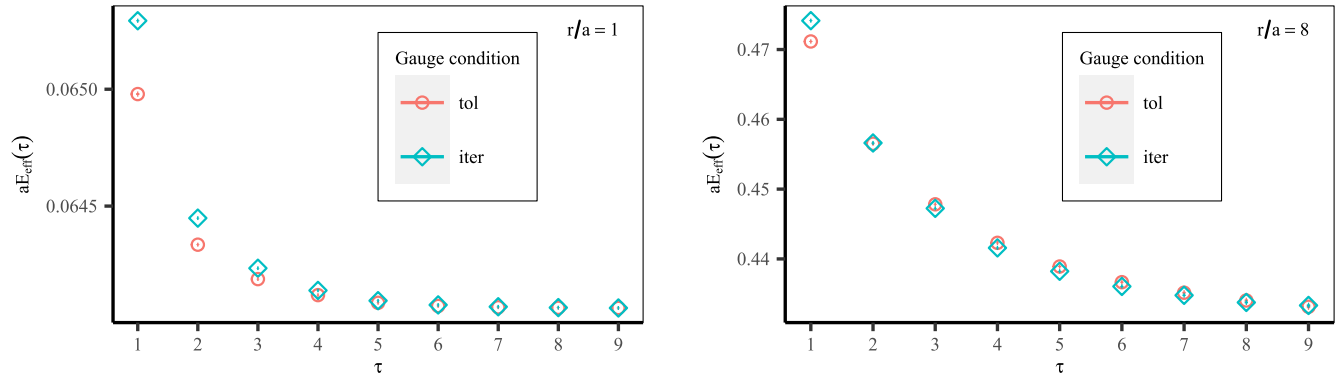

FIG. 22. The effective mass $aE_{\text{eff}}(\tau)$ has been calculated on the two subsets of the ensemble β `6.72 M i` with different gauge-fixing schemes, which are labeled `tol` for fixed tolerance (red) and `iter` for fixed number of iterations (teal). $aE_{\text{eff}}(\tau)$ differs at small τ but approaches the same plateau at large τ. Note, that the ordering of the two gauge-fixing schemes changes in a statistically significant manner with τ. At least two crossings occur for larger r/a; the first of these occurs at smaller τ for larger r/a. We show the effective mass for one iteration of HYP smearing since the errors and fluctuations are larger without smearing. Jackknife errors are obtained from the distribution of the resamples.

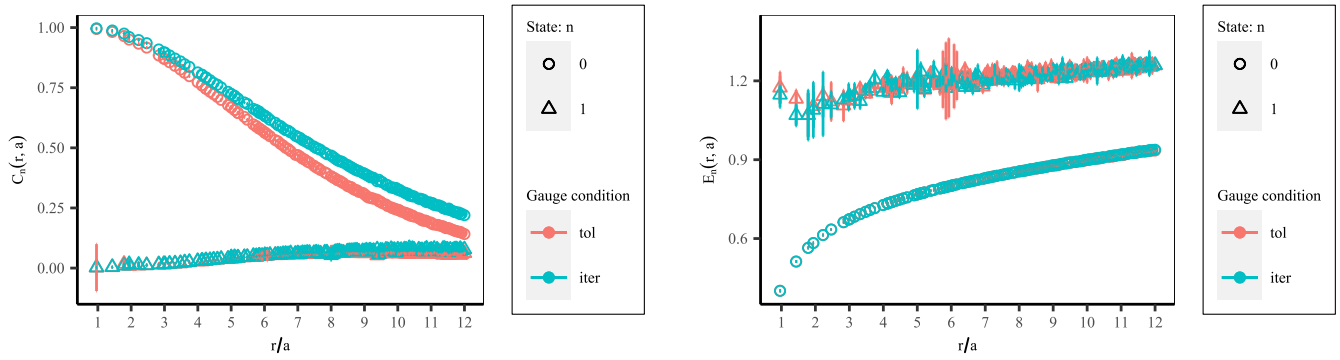

FIG. 23. The correlation function (without smearing) has been analyzed on the two subsets of the ensemble β `6.72 M i` with different gauge-fixing schemes via three-state fits (for the schemes and the color code, see Fig. 22 and text). Left: both overlap factors, $C_{0,1}$, of the ground state or first excited state, respectively, decrease as the volume-averaged final gauge-fixing functional is reduced towards a lower tolerance. The relative decrease of the ground state overlap factor $C_0(r,a)$ increases quite dramatically from 0.3% at $r/a = 1$ to 30% at $r/a = 12$. For the excited state, the overlap factor $C_1(r,a)$ changes mildly by about 40% at $r/a = 1$ to 25% at $r/a = 12$; however, since $C_1(r,a)$ increases for large r/a, this is statistically significant only for large enough r/a. Right: the change of the energy levels between the two smearing schemes is statistically insignificant. $E_1(r,a)$ represents in this plot the full first excited state energy. Thick error bars represent Hessian errors, while thin error bars represent jackknife errors obtained from the distribution of the resamples.

deviation between the volume-averaged final gauge-fixing functional). Since the time history mostly consisted of consecutive segments that used either tolerance or step number as criteria, this led to unexpectedly large autocorrelations in the correlator size in some streams that were, however, practically absent in the effective mass.

As a consequence, we analyzed the subsets of the β `6.72 M i` ensemble with different gauge-fixing schemes separately and confirmed the independence of the energy levels. We show the results of this analysis on the level of the effective mass in Fig. 22 and on the level of the fit parameters in Fig. 23.

APPENDIX B: ADDITIONAL PLOTS AND TABLES OF NUMERICAL DATA

This appendix contains additional material in which we discuss further details of the analysis. In Appendix. B 1 we provide further details on the correlator fits. We tabulate the tree-level corrections in Appendix. B 2. Appendix B 3 extends the discussion of the systematic uncertainty and the discretization effects of the scales and string tension.

1. Fit ranges, quality, and stability

Table III shows the actual time ranges used in the correlator fits. The choices have been informed by keeping similar time ranges in physical units across all ensembles accounting for the number of states used, see Eq. (2.5), with an extra variation to check for systematic effects.

We show representative plots of p value distributions for correlator fits with different numbers of states on the physical β `7.00 M i` ensemble in Fig. 24. We show stability plots for the ground state energy on the same ensemble under variation of the time range or of the number of states in Fig. 25.

TABLE III. Time intervals used in the correlator fits, see Sec. II B; $t = \tau/a$. And open-ended dash means "until upper or lower end of available data", respectively. Entries marked as "…" indicate that the fit was not possible.

$\approx a$ (fm)	β	$t_{\max}$	Operator	r_I/a	$t_{\min}^{(1,-)}$	$t_{\min}^{(2,-)}$	$t_{\min}^{(3,-)}$	$t_{\min}^{(1,0)}$	$t_{\min}^{(2,0)}$	$t_{\min}^{(3,0)}$	$t_{\min}^{(1,+)}$	$t_{\min}^{(2,+)}$	$t_{\min}^{(3,+)}$
0.15	5.8	9	Bare	All	1	1	…	2	2	…	3	3	…
			HYP	–3.5	1	1	2	2	2	2	3	3	2
				3.5–	1	1	1	2	2	1	3	3	1
0.12	6.0	6	Bare	–1.6	2	2	…	3	2	…	…	…	…
				1.6–	2	2	…	3	2	…	…	…	…
			HYP	–3.5	2	2	1	3	2	1	…	…	…
				3.5–	2	2	…	3	2	1	…	…	…
0.088	6.3	8	Bare	–1.0	3	1	2	4	2	2	5	3	2
				1.0–3.5	3	2	2	4	3	2	5	3	2
				3.5–	3	2	1	4	3	1	5	3	1
			HYP	–3.5	3	3	2	4	3	2	5	3	2
				3.5–	3	3	1	4	3	1	5	3	1
0.057	6.72	10	Bare	–1.6	4	3	2	5	3	2	6	4	2
				1.6–1.9	5	3	2	6	4	2	7	4	2
				1.9–3.0	5	3	2	6	4	2	7	5	2
				3.0–3.5	5	3	2	6	4	2	7	5	3
				3.5–	5	3	1	6	4	2	7	5	3
			HYP	–1.6	4	3	2	5	3	2	6	4	2
				1.6–1.9	5	3	2	6	3	2	7	4	2
				1.9–3.0	5	3	2	6	4	2	7	5	2
				3.0–3.5	5	3	2	6	4	2	7	5	3
				3.5–	5	3	1	6	4	2	7	5	3

(Table continued)

TABLE III. *(Continued)*

$\approx a$ (fm)	β	$t_{\max}$	Operator	r_I/a	$t_{\min}^{(1,-)}$	$t_{\min}^{(2,-)}$	$t_{\min}^{(3,-)}$	$t_{\min}^{(1,0)}$	$t_{\min}^{(2,0)}$	$t_{\min}^{(3,0)}$	$t_{\min}^{(1,+)}$	$t_{\min}^{(2,+)}$	$t_{\min}^{(3,+)}$
0.042	7.0	20	Bare	–1.0	5	3	2	6	3	2	7	4	2
				1.0–2.4	6	3	2	7	4	2	8	5	2
				2.4–2.7	6	3	2	8	4	2	9	5	2
				2.7–3.0	7	4	2	8	5	2	9	6	2
				3.0–3.5	7	4	2	8	5	2	9	6	3
				3.5–3.8	7	4	1	8	5	2	9	6	3
				3.8–6.0	7	5	1	8	6	2	9	7	3
				6.0–9.0	7	5	2	8	6	3	9	7	4
				9.0–	7	5	3	8	6	4	9	7	5
			HYP	–2.5	6	3	2	8	4	2	7	4	2
				2.5–3.0	7	4	2	8	5	2	8	5	2
				3.0–3.5	7	4	2	8	5	2	8	5	2
				3.5–3.8	7	4	1	8	5	1	8	5	2
				3.8–6.0	7	5	1	8	6	1	8	6	2
				6.0–9.0	7	5	2	8	6	2	8	6	3
				9.0–	7	5	3	8	6	3	8	6	4
0.032	7.28	28	Bare	–1.0	7	3	2	8	4	2	9	5	2
				1.0–1.6	7	4	2	8	5	2	9	6	2
				1.6–2.5	8	4	2	9	5	2	10	6	2
				2.5–2.8	9	4	2	9	5	2	10	6	2
				2.8–2.9	9	4	2	10	5	2	11	6	2
				2.9–3.0	9	5	2	10	6	2	11	7	2
				3.0–3.5	9	5	2	10	6	2	11	7	3
				3.5–4.3	9	5	1	10	6	2	11	7	3
				4.3–5.8	9	6	1	10	7	2	11	8	3
				5.8–6.0	9	7	1	10	8	2	11	9	3
				6.0–9.0	9	7	2	10	8	3	11	9	4
				9.0–12.0	9	7	3	10	8	4	11	9	5
				12.0–15	9	7	4	10	8	5	11	9	6
				15.0–	9	7	5	10	8	6	11	9	7
			HYP	–1.7	7	4	2	8	5	2	9	6	2
				1.7–2.5	8	4	2	9	5	2	10	6	2
				2.5–2.8	9	4	2	9	5	2	11	6	2
				2.8–2.9	9	4	2	10	5	2	11	6	2
				2.9–3.0	9	5	2	10	6	2	11	7	2
				3.0–3.5	9	5	2	10	6	2	11	7	3
				3.5–4.3	9	5	1	10	6	2	11	7	3
				4.3–5.8	9	6	1	10	7	2	11	8	3
				5.8–6.0	9	7	1	10	8	2	11	9	3
				6.0–9.0	9	7	2	10	8	3	11	9	4
				9.0–12	9	7	3	10	8	4	11	9	5
				12–15	9	7	4	10	8	5	11	9	6
				15–	9	7	5	10	8	6	11	9	7

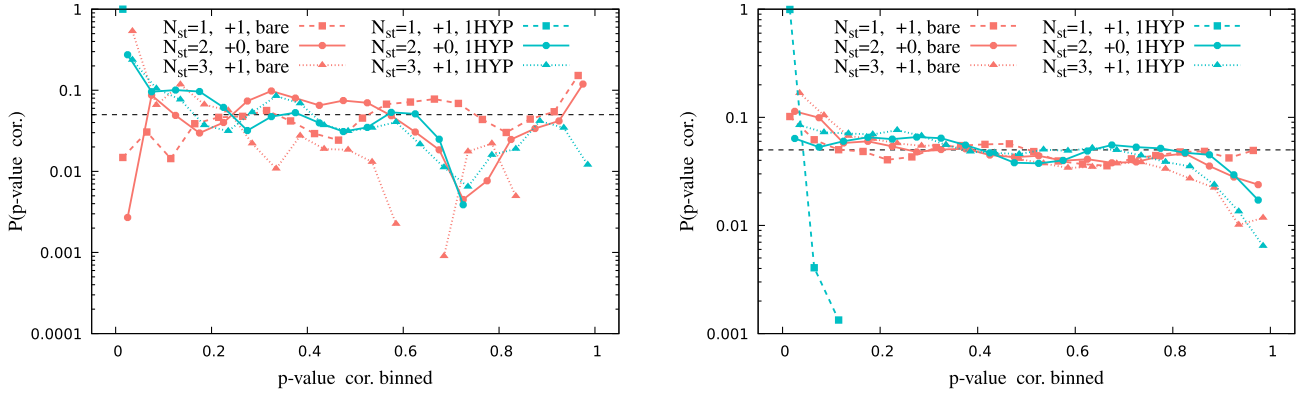

FIG. 24. Distribution of p values for fits to the correlator on the physical β `7.00 M i` ensemble. The horizontal dashed line corresponds to a flat distribution at $P(p\,\text{value}) = 1/20$, while colored lines serve as guides to the eyes. We separately show results at small distances, i.e., $|\boldsymbol{r}| \leq 0.2$ fm (left) or at large distances, i.e., $|\boldsymbol{r}| > 0.2$ fm (right). The former constitutes a much smaller sample of fits (fewer combinations of $|\boldsymbol{r}|/a$). Left: at $|\boldsymbol{r}| \leq 0.2$ fm, the p value distribution is reasonably flat in the case of bare links and $N_{\text{st}} \leq 2$, while fits with $N_{\text{st}} \geq 2$ in similar ranges fare similarly well for smeared links. Right: at $|\boldsymbol{r}| > 0.2$ fm, the p value distribution with bare links is quite flat. Fits with $N_{\text{st}} = 1$ in similar intervals are disfavored for smeared links.

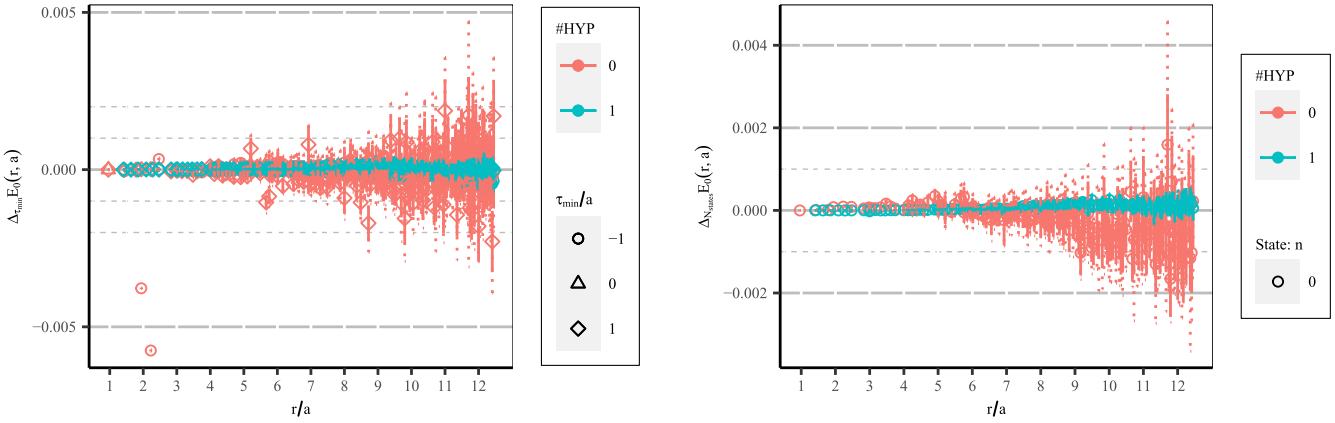

FIG. 25. Stability plots of the correlation function fits for the physical β `7.00 M i` ensemble. Differences between extracted ground state energy values $E_0(r,a)$ from different fits are usually covered by the statistical errors corresponding to our canonical choice of fits, i.e., with $N_{\text{st}} = 2$ and $\tau_{\text{min}}^{(2,0)}/a$. Dotted error bars represent Hessian errors, while solid error bars represent jackknife errors obtained from the distribution of the resamples. Left: for fits with $N_{\text{st}} = 2$, we vary τ_{min}/a by ± 1 against our canonical fit. We clearly see that the fit stability breaks down at a few small $\boldsymbol{r}/a$ values for the choice $\tau_{\text{min}}^{(2,-)}/a$. Right: we compare the fits with $N_{\text{st}} = 3$ and $\tau_{\text{min}}^{(3,+)}/a$ to our canonical fits $N_{\text{st}} = 2$ and $\tau_{\text{min}}^{(2,0)}/a$. For $\tau_{\text{min}}^{(3,0)}/a$ we already see that the fit stability breaks down in a few cases.

2. Tree-level corrections

We collect the tree-level corrections for bare or smeared links in Table IV, which are part of an ongoing project aiming at a full one-loop calculation [92] using the HiPPy software package and the HPsrc software framework [90,91].

3. Detailed definition of the scales and the string tension

We show the fit range dependence of the extracted values of $a^2\sigma$ for the physical β `7.00 M i` ensemble (with bare links) using two different fixed values of the Coulomb coefficient in Fig. 26. The distribution with the random picks is fairly Gaussian. For the determinations of the scales r_i/a, the corresponding distributions are in Fig. 5 in Sec. III B. These distributions for r_i/a clearly exhibit non-Gaussian characteristics and, in some cases, correlations between R_{min} and the obtained value of r_i/a, see Fig. 27. The string tension in physical units shows a fairly mild lattice spacing dependence, much smaller than the dependence on assumptions about the Coulomb coefficient, see Fig. 28.

4. Relative scale setting

In this section, we collect additional material relevant for the relative scale setting, namely the scales r_i/a,

TABLE IV. Spatial Euclidean distance $|\boldsymbol{r}|/a$ and tree-level improved distances r_I/a for bare links or for links after one step of HYP smearing in the fourth, fifth, and sixth column. Each row corresponds to any permutation of the three spatial coordinates x_i/a since these belong to the same representation of the cubic group W_3. For bare links the improved distance is smaller than the corresponding Euclidean distance for on-axis vectors with $|\boldsymbol{r}|/a < 5$ and for a few off-axis vectors in the same range; the relative modification is at most 0.3% for $|\boldsymbol{r}|/a > \sqrt{12}$. For smeared links the improved distance is larger than the corresponding Euclidean distance except for $\boldsymbol{r}/a = (2, 2, 1)$ or (2, 2, 2); the relative modification is at most 0.3% for $|\boldsymbol{r}|/a > \sqrt{10}$.

x_1/a	x_2/a	x_3/a	$\lvert\boldsymbol{r}\rvert/a$	r_I/a (bare links)	r_I/a (smeared links)
1	0	0	1.0	0.959904 ± 0.000003	1.409072 ± 0.000027
1	1	0	1.414214	1.433383 ± 0.000013	1.634790 ± 0.000047
1	1	1	1.732051	1.786648 ± 0.000031	1.846760 ± 0.000072
2	0	0	2.0	1.940264 ± 0.000049	2.086964 ± 0.000109
2	1	0	2.236068	2.225023 ± 0.000081	2.282411 ± 0.000149
2	1	1	2.449490	2.465341 ± 0.000119	2.469253 ± 0.000197
2	2	0	2.828427	2.827621 ± 0.000208	2.832540 ± 0.000319
2	2	1	3.0	3.012822 ± 0.000264	2.996896 ± 0.000390
3	0	0	3.0	2.979371 ± 0.000265	3.019798 ± 0.000401
3	1	0	3.162278	3.151661 ± 0.000327	3.174122 ± 0.000479
3	1	1	3.316625	3.315550 ± 0.000396	3.323076 ± 0.000565
2	2	2	3.464102	3.477834 ± 0.000467	3.457683 ± 0.000649
3	2	0	3.605551	3.604281 ± 0.000550	3.608266 ± 0.000761
3	2	1	3.741657	3.746234 ± 0.000637	3.742821 ± 0.000868
4	0	0	4.0	3.994281 ± 0.000855	4.009312 ± 0.001140
3	2	2	4.123106	4.131366 ± 0.000932	4.123893 ± 0.001236
4	1	0	4.123106	4.118891 ± 0.000960	4.130599 ± 0.001270
3	3	0	4.242641	4.244320 ± 0.001049	4.245404 ± 0.001382
4	1	1	4.242641	4.240985 ± 0.001072	4.248958 ± 0.001406
3	3	1	4.358899	4.363650 ± 0.001165	4.361678 ± 0.001525
4	2	0	4.472136	4.472231 ± 0.001313	4.477483 ± 0.001703
4	2	1	4.582576	4.584957 ± 0.001442	4.587801 ± 0.001860
3	3	2	4.690416	4.698346 ± 0.001549	4.694392 ± 0.001997
4	2	2	4.898979	4.904615 ± 0.001863	4.904903 ± 0.002375
4	3	0	5.0	5.003469 ± 0.002027	5.006342 ± 0.002573
5	0	0	5.0	5.000618 ± 0.002127	5.010612 ± 0.002666
4	3	1	5.099020	5.104096 ± 0.002184	5.105849 ± 0.002764
5	1	0	5.099020	5.100262 ± 0.002286	5.109318 ± 0.002860
3	3	3	5.196152	5.205202 ± 0.002313	5.203278 ± 0.002930
5	1	1	5.196152	5.198344 ± 0.002452	5.206361 ± 0.003060
4	3	2	5.385165	5.392954 ± 0.002689	5.393750 ± 0.003380
5	2	0	5.385165	5.388792 ± 0.002802	5.395594 ± 0.003484
5	2	1	5.477226	5.481937 ± 0.002983	5.487994 ± 0.003703
4	4	0	5.656854	5.663307 ± 0.003299	5.667292 ± 0.004106
4	4	1	5.744563	5.752137 ± 0.003495	5.755734 ± 0.004344
5	2	2	5.744563	5.751750 ± 0.003562	5.756765 ± 0.004404
4	3	3	5.830952	5.841093 ± 0.003653	5.842952 ± 0.004549
5	3	0	5.830952	5.837748 ± 0.003783	5.843586 ± 0.004667
5	3	1	5.916080	5.923874 ± 0.003991	5.929386 ± 0.004919
4	4	2	6.0	6.009986 ± 0.004115	6.013449 ± 0.005097
6	0	0	6.0	6.006756 ± 0.004501	6.017224 ± 0.005441

$i = 0$, 1, 2, and the string tension $a^2\sigma$ from the direct fits in Table V, two different parametrizations in terms of Allton fits in Table VI, and the smoothened scales r_i/a, $i = 0$, 1 and σr_0^2, respectively, in Table VII. Finally, in Fig. 29, we show the Allton fits for the scales with smeared links.

5. Continuum extrapolations

In this section, we collect additional material relevant for the continuum extrapolations. The continuum extrapolations of bare- or smeared-link data for r_0/r_1 as a function of $(a/r_1)^2$ are shown in Fig. 30. We show the continuum results and the approach to the continuum limit for

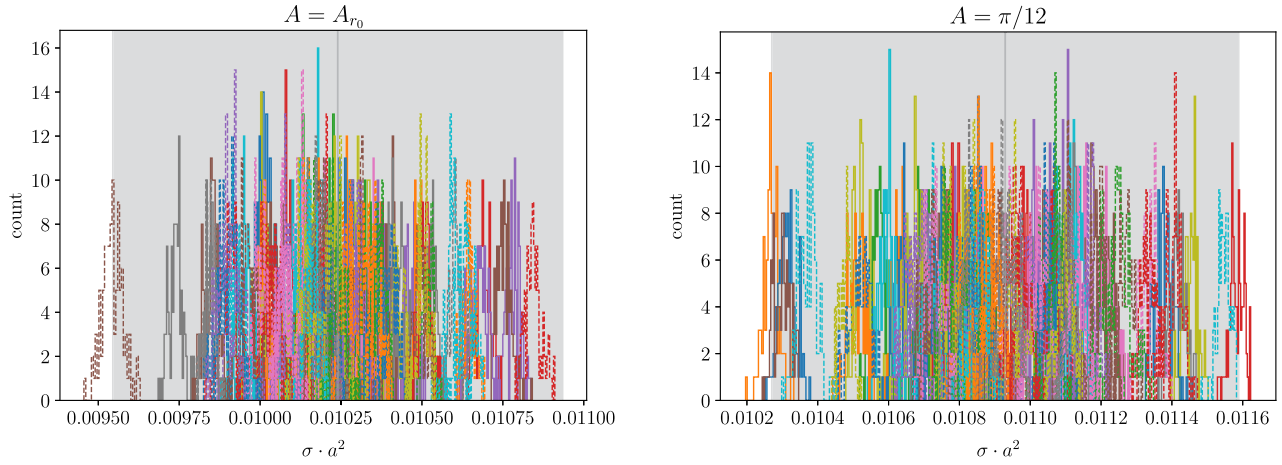

FIG. 26. The distribution of the results obtained on the N_J jackknife pseudoensembles for each set of N_P random picks (designated by the color) is not dissimilar to a Gaussian distribution. However, the distribution of the jackknife means over the N_P sets of random picks is usually not similar to a Gaussian distribution. The data are shown for the bare physical β `7.0 M i` ensemble. The gray vertical line and the gray band represent the corresponding mean value and error estimate in Table V.

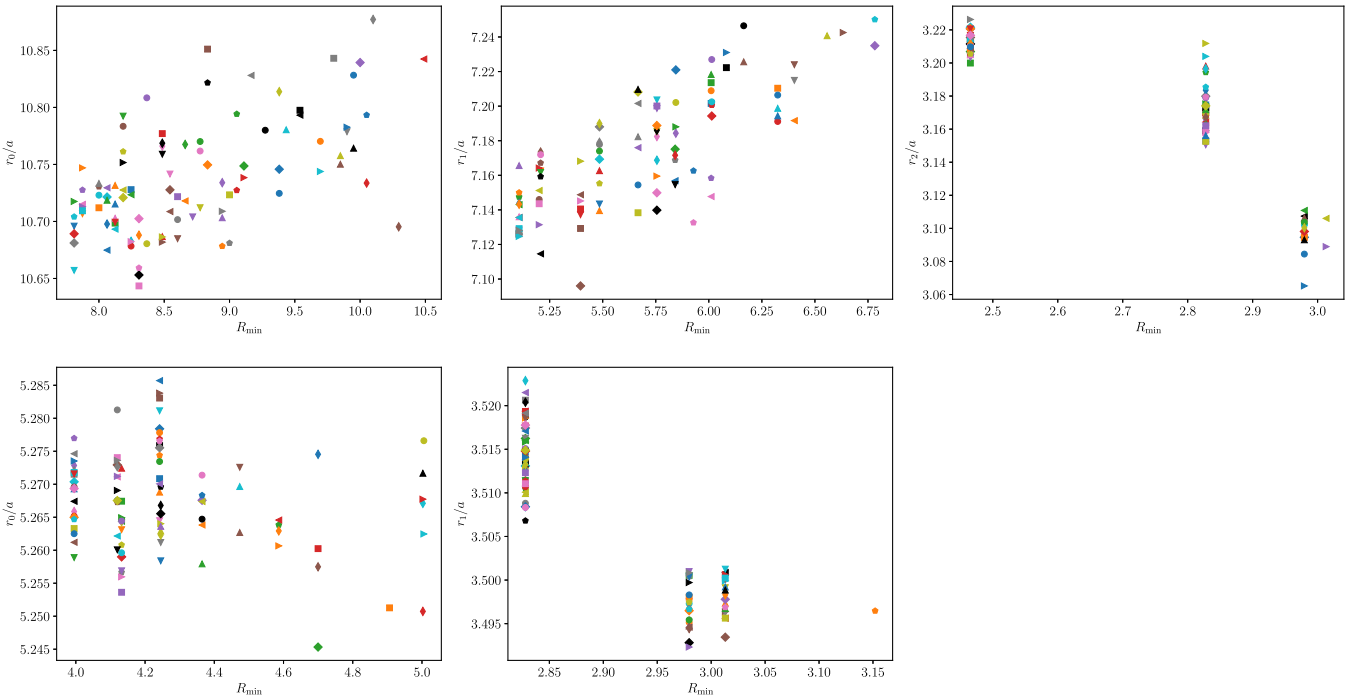

FIG. 27. Dependence of the fit results on the $R_{\min}$ of the N_P randomly selected data points for the first jackknife pseudoensemble of the bare physical β `7.00 M i` ensemble (top) and the bare physical β `6.30 M i` ensemble (bottom). There are correlations between the extracted r_i/a and $R_{\min}$ that are similar between the different ensembles but strongly vary with the considered R range.

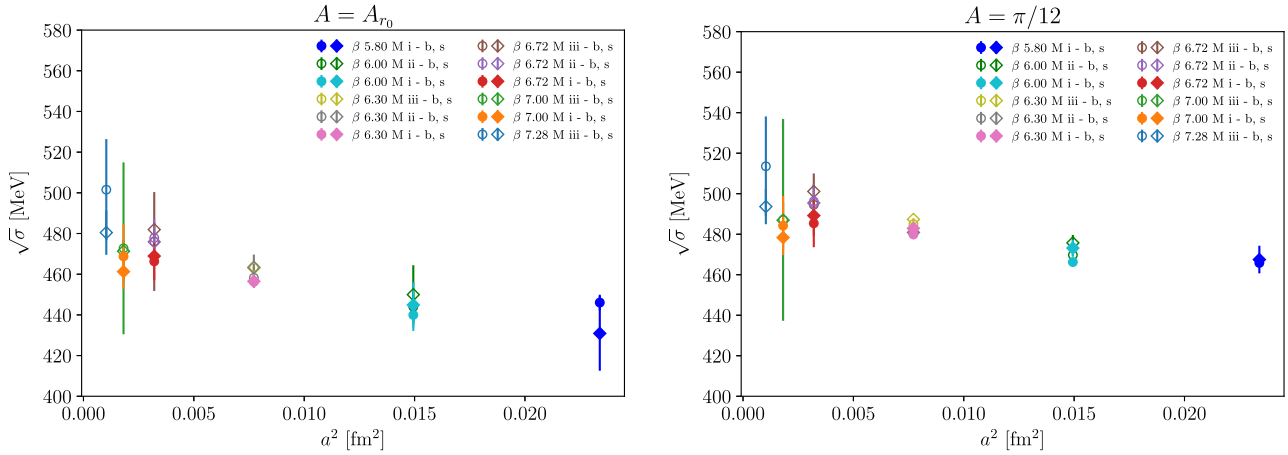

FIG. 28. The string tension $\sqrt{\sigma}$ for all ensembles (indicated by colors) and bare (circles) and smeared (diamonds) gauge links and for the different choices of A. We use the lattice scale $a_{f_{p4s}}$ to convert to physical units and $a^2_{f_{p4s}}$ for the x coordinate. Filled symbols correspond to physical light quark mass ensembles, while open symbols represent larger than physical quark masses.

TABLE V. r_i/a, $i = 0, 1, 2$ and $a^2\sigma$ for all ensembles with the two different choices of A. The first of each row is for bare links, the second one for smeared links. The smeared-link values in brackets are replaced with the bare ones as explained in the text. Entries marked as "$\cdots$" indicate that the fit was not possible.

Ensemble	r_0/a	r_1/a	r_2/a	$a^2\sigma$ $(A = A_{r_0})$	$a^2\sigma$ $(A = \pi/12)$
β 5.80 M i	3.09640 ± 0.01286	$\cdots$	$\cdots$	0.11952 ± 0.00206	0.13035 ± 0.00118
	3.02320 ± 0.09242	$\cdots$	$\cdots$	0.11153 ± 0.00949	0.13128 ± 0.00383
β 6.00 M ii	3.83872 ± 0.01950	2.56673 ± 0.03562	$\cdots$	0.07564 ± 0.00258	0.08468 ± 0.00025
	3.77465 ± 0.08278	$[2.41291 \pm 0.07079]$	$\cdots$	0.07769 ± 0.00499	0.08685 ± 0.00143
β 6.00 M i	3.85113 ± 0.01557	2.56844 ± 0.04089	$\cdots$	0.07428 ± 0.00266	0.08343 ± 0.00011
	3.81394 ± 0.04370	$[2.42701 \pm 0.12536]$	$\cdots$	0.07595 ± 0.00379	0.08591 ± 0.00151
β 6.30 M iii	5.15895 ± 0.03287	3.47263 ± 0.03436	$\cdots$	0.04258 ± 0.00061	0.04663 ± 0.00041
	5.18334 ± 0.05663	$[3.42049 \pm 0.09021]$	$\cdots$	0.04251 ± 0.00052	0.04708 ± 0.00012
β6.30 M ii	5.22042 ± 0.03414	3.49545 ± 0.02301	$\cdots$	0.04163 ± 0.00065	0.04577 ± 0.00023
	5.26352 ± 0.08370	$[3.52911 \pm 0.06433]$	$\cdots$	0.04257 ± 0.00115	0.04584 ± 0.00013
β 6.30 M i	5.26708 ± 0.02218	3.50938 ± 0.01723	$\cdots$	0.04128 ± 0.00039	0.04565 ± 0.00020
	5.27320 ± 0.10936	$[3.45729 \pm 0.11000]$	$\cdots$	0.04131 ± 0.00059	0.04623 ± 0.00038
β 6.72 M iii	7.88980 ± 0.08546	5.29637 ± 0.03357	2.45044 ± 0.06290	0.01866 ± 0.00190	0.02014 ± 0.00126
	7.85715 ± 0.14605	5.27694 ± 0.07599	$[2.12384 \pm 0.19803]$	0.01912 ± 0.00025	0.02067 ± 0.00028
β 6.72 M ii	7.92209 ± 0.05545	5.32775 ± 0.02521	2.45062 ± 0.07633	0.01880 ± 0.00074	0.02027 ± 0.00070
	7.93435 ± 0.13460	5.30683 ± 0.06247	$[2.12747 \pm 0.16083]$	0.01865 ± 0.00026	0.02020 ± 0.00021
β 6.72 M i	8.03302 ± 0.07694	5.38261 ± 0.02038	2.46825 ± 0.07423	0.01790 ± 0.00071	0.01940 ± 0.00094
	8.00053 ± 0.16195	5.38097 ± 0.07864	$[2.14853 \pm 0.18989]$	0.01810 ± 0.00025	0.01970 ± 0.00022
β 7.00 M iii	10.55417 ± 0.38163	7.06784 ± 0.12644	3.19097 ± 0.13449	0.01041 ± 0.00186	0.01106 ± 0.00226
	10.58371 ± 0.10773	7.06499 ± 0.08959	3.10774 ± 0.03702	0.01035 ± 0.00025	0.01105 ± 0.00040
β 7.00 M i	10.72634 ± 0.15351	7.16677 ± 0.08142	3.20894 ± 0.14144	0.01024 ± 0.00070	0.01093 ± 0.00066
	10.81068 ± 0.11230	7.18318 ± 0.10637	3.13717 ± 0.06911	0.00992 ± 0.00022	0.01066 ± 0.00027
β 7.28 M iii	13.58998 ± 0.28745	9.26165 ± 0.12521	4.21509 ± 0.02629	0.00668 ± 0.00066	0.00700 ± 0.00067
	13.93468 ± 0.27129	9.38512 ± 0.10500	4.21051 ± 0.08218	0.00613 ± 0.00028	0.00647 ± 0.00023

TABLE VI. Coefficients of the Allton fits, Eq. (3.7). For each of r_0/a or r_1/a, the first of the two rows shows bare results, while the second one shows smeared results.

Linear in am_{tot}					
	C_{00}	C_{01}	$C_{20}/10^5$	$D_2/10^3$	χ^2_{red}
r_0/a	21.94181 ± 1.68077	0.08587 ± 0.02668	1.08538 ± 0.49989	2.86204 ± 1.48991	$6.03305/8 = 0.75413$
	20.50314 ± 2.06333	0.10875 ± 0.03774	0.36230 ± 1.13404	0.57839 ± 3.37576	$1.30035/8 = 0.16254$
r_1/a	34.72718 ± 1.76851	0.08556 ± 0.02828	3.13605 ± 2.24815	5.78128 ± 4.79208	$1.24069/7 = 0.17724$
	32.21438 ± 2.83572	0.12787 ± 0.05211	3.04080 ± 2.67043	5.77559 ± 5.62018	$0.43440/7 = 0.06206$
Quadratic in am_{tot}					
	C_{00}	C_{02}	$C_{20}/10^5$	$D_2/10^3$	χ^2_{red}
r_0/a	25.82044 ± 0.53306	0.15358 ± 0.04626	1.28496 ± 0.54074	5.02550 ± 1.69661	$3.70085/8 = 0.46261$
	25.59835 ± 0.46671	0.18195 ± 0.06659	0.26569 ± 1.27393	2.03565 ± 3.54790	$1.49736/8 = 0.18717$
r_1/a	38.65447 ± 0.74486	0.15049 ± 0.05064	3.28647 ± 2.38685	7.10549 ± 5.08679	$1.01596/7 = 0.14514$
	38.05123 ± 0.77302	0.22051 ± 0.09517	3.41874 ± 2.93632	8.03369 ± 6.03171	$0.49725/7 = 0.07104$

TABLE VII. r_i/a, $i = 0, 1$, and $\sqrt{r_0^2\sigma}$ for all ensembles with the different choices of A using the smoothened r_0/a from the Allton fits. The values in brackets stem from the Allton fits, but we do not have a direct determination. The first of each row is for bare links, the second one for smeared links. Entries marked as "…" indicate that the fit was not possible.

Ensemble	r_0/a	r_1/a	$\sqrt{\sigma r_0^2}$ $(A = A_{r_0})$	$\sqrt{\sigma r_0^2}$ $(A = \pi/12)$
l3248f211b580m00235m0647m831	3.09673 ± 0.01204	…	1.07061 ± 0.01013	1.11805 ± 0.00666
	3.01140 ± 0.07614	…	1.00569 ± 0.04979	1.09112 ± 0.03185
l3264f211b600m00507m0507m628	3.83628 ± 0.00856	2.56244 ± 0.02403	1.05509 ± 0.01812	1.11634 ± 0.00299
	3.79648 ± 0.03130	2.56593 ± 0.02591	1.05822 ± 0.03509	1.11882 ± 0.01302
l4864f211b600m00184m0507m628	3.84897 ± 0.00986	2.56725 ± 0.02304	1.04899 ± 0.01895	1.11173 ± 0.00293
	3.81537 ± 0.03320	2.57260 ± 0.02423	1.05150 ± 0.02777	1.11832 ± 0.01383
l3296f211b630m0074m037m440	5.19001 ± 0.01869	3.48020 ± 0.01224	1.07091 ± 0.00853	1.12073 ± 0.00641
	5.17709 ± 0.03704	3.47017 ± 0.01736	1.06741 ± 0.01007	1.12328 ± 0.00816
l4896f211b630m00363m0363m430	5.24553 ± 0.01325	3.50231 ± 0.01153	1.07022 ± 0.00878	1.12227 ± 0.00396
	5.25407 ± 0.04198	3.50118 ± 0.01247	1.08402 ± 0.01702	1.12492 ± 0.00914
l6496f211b630m0012m0363m432	5.25416 ± 0.01396	3.50572 ± 0.01203	1.06745 ± 0.00573	1.12265 ± 0.00389
	5.26608 ± 0.04551	3.50598 ± 0.01362	1.07037 ± 0.01202	1.13231 ± 0.01081
l48144f211b672m0048m024m286	7.86707 ± 0.04293	5.30732 ± 0.02156	1.07467 ± 0.05516	1.11633 ± 0.03541
	7.86948 ± 0.08455	5.28136 ± 0.04660	1.08820 ± 0.01372	1.13151 ± 0.01430
l64144f211b672m0024m024m286	7.89244 ± 0.03821	5.31806 ± 0.01868	1.08215 ± 0.02194	1.12375 ± 0.02018
	7.90203 ± 0.07380	5.29661 ± 0.04068	1.07905 ± 0.01252	1.12321 ± 0.01195
l96192f211b672m0008m022m260	8.05163 ± 0.03896	5.38486 ± 0.01662	1.07731 ± 0.02207	1.12140 ± 0.02783
	8.10762 ± 0.04793	5.39212 ± 0.02820	1.09084 ± 0.00982	1.13805 ± 0.00929
l64192f211b700m00316m0158m188	10.57092 ± 0.07717	7.08912 ± 0.03450	1.07880 ± 0.09674	1.11155 ± 0.11400
	10.63795 ± 0.06414	7.10727 ± 0.04002	1.08239 ± 0.01456	1.11827 ± 0.02148
l144288f211b700m000569m01555m1827	10.64095 ± 0.09157	7.11895 ± 0.03886	1.07678 ± 0.03771	1.11245 ± 0.03490
	10.72618 ± 0.07495	7.15068 ± 0.04681	1.06813 ± 0.01416	1.10769 ± 0.01581
l96288f211b728m00223m01115m1316	13.90017 ± 0.15482	9.31454 ± 0.08267	1.13621 ± 0.05777	1.16337 ± 0.05728
	14.00094 ± 0.12505	9.37267 ± 0.08271	1.09633 ± 0.02682	1.12639 ± 0.02226

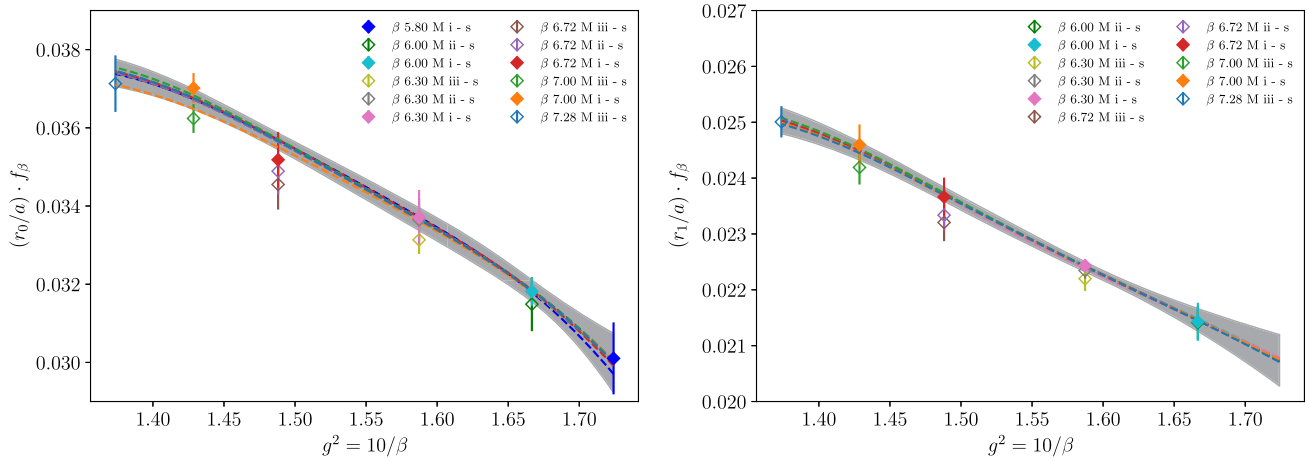

FIG. 29. The potential scales r_i/a, $i = 0, 1$ multiplied by the two-loop β-function, f_β as in Eq. (3.8), for all ensembles (indicated by colors) and smeared links. Any further details about the plot can be found in the caption of the corresponding figure for bare links in Fig. 9 in Sec. III C.

smeared-link data, in particular, for r_0/r_1 and r_1/r_2 in Fig. 31, for $a_{f_{p4s}} r_0/a$ and $a_{f_{p4s}} r_1/a$ in Fig. 32, or for $\sqrt{\sigma r_0^2}$ with two different coefficients for the Coulomb term in Fig. 33.

We provide further information regarding the distribution of errors from the different continuum extrapolations, in particular, for r_0/r_1 and r_1/r_2 in Fig. 34, for $a_{f_{p4s}} r_0/a$ and $a_{f_{p4s}} r_1/a$ in Fig. 35, or for $\sqrt{\sigma r_0^2}$ with two different coefficients for the Coulomb term in Fig. 36. We show the histogram of the Hessian regression errors together with the error estimate from the width of the central values' histogram and, in further panels, correlation plots between the central values and the regression errors. In the case of r_0/r_1, 64 instances in the left-most bin are due to fits with zero degree of freedom (where we use zero for the error). In all three cases among r_0/r_1, $a_{f_{p4s}} r_0/a$, and $a_{f_{p4s}} r_1/a$ we see a fairly sharp drop of the error distribution beyond the bin containing our error estimate. While there is no obvious correlation between central values and regression errors for r_0/r_1, there are correlations between larger regression errors and larger central values for $a_{f_{p4s}} r_0/a$ and $a_{f_{p4s}} r_1/a$. For r_1/r_2, this is quite different. Our error estimate is significantly larger than the majority of regression errors. Although all regressions with large errors correspond to high central values, not all regressions with central values entail large errors. Lastly, for the string

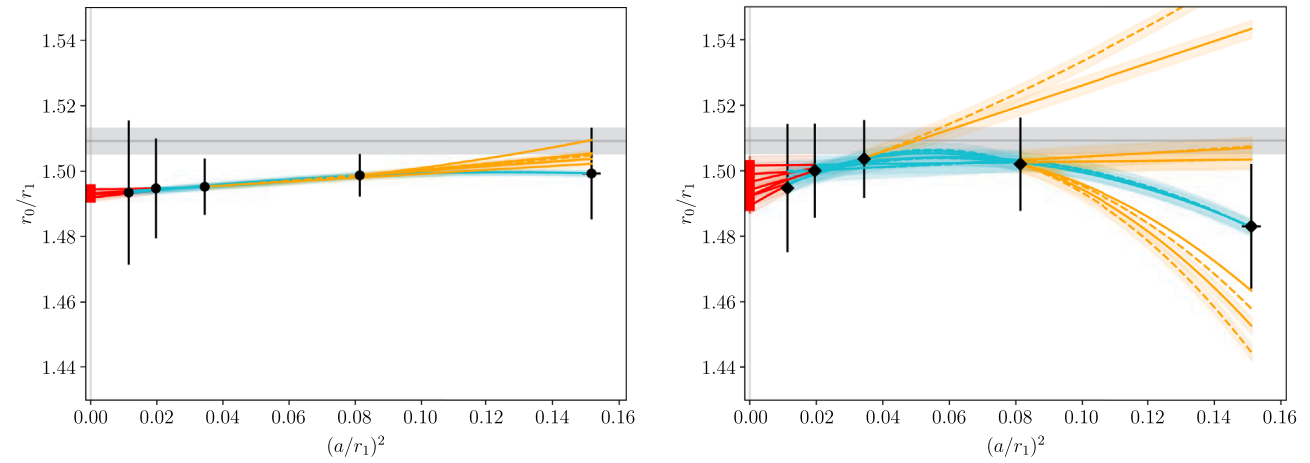

FIG. 30. Continuum extrapolation of the parametrization of r_0/r_1 evaluated at the physical m_l/m_s-ratio for $6.0 \leq \beta \leq 7.28$ as a function of $(a/r_1)^2$. The black points show the bare-link data (left) and the smeared-link data (right) with the corresponding continuum results shown in red. The lines and bands show the fit curves and errors, within the fit range in cyan, as extrapolations towards the continuum or coarser lattices in red/orange, respectively. The gray solid line and band indicate the HotQCD result in $(2 + 1)$-flavor QCD [16]. Note that the weighted average is absent in this figure since it is the same that is already shown in the corresponding panels for extrapolation as a function of $(a/r_0)^2$ in Fig. 11 in Sec. IV A.

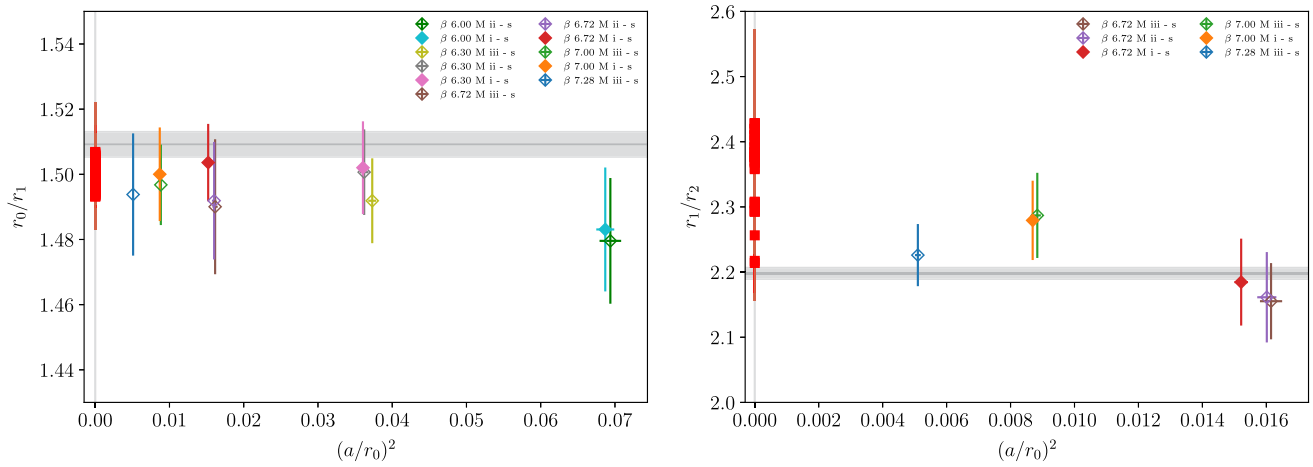

FIG. 31. Continuum results (red) and smoothened data (other colors) for the ratios r_0/r_1 or r_1/r_2 are shown in the left or right columns, respectively, as functions of $(a/r_0)^2$, using smeared-link data. The gray solid line and band show the $(2+1)$-flavor QCD reference values [11,16]. The corresponding plot for bare links is shown in Fig. 13 in Sec. IV.

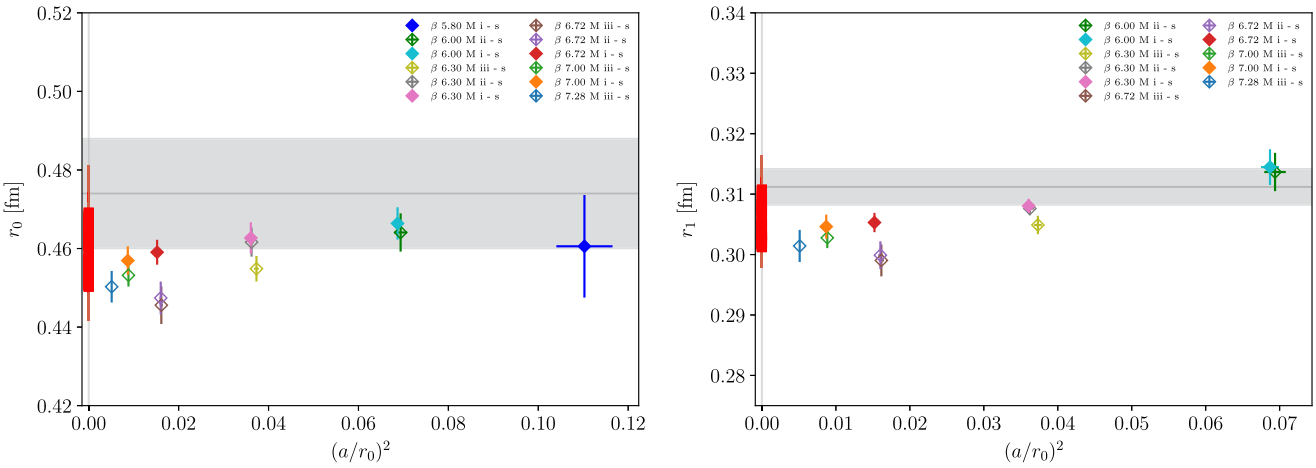

FIG. 32. Continuum results (red) and smoothened data (other colors) for $a_{f_{p4s}} r_{0,1}/a$ are shown in the left or right columns, respectively, as functions of $(a/r_0)^2$, using bare links. The gray solid line and band show the published $(2+1+1)$-flavor QCD values [25,34] for r_0 and r_1, respectively. The corresponding plots for bare links are shown in Fig. 15 in Sec. IV.

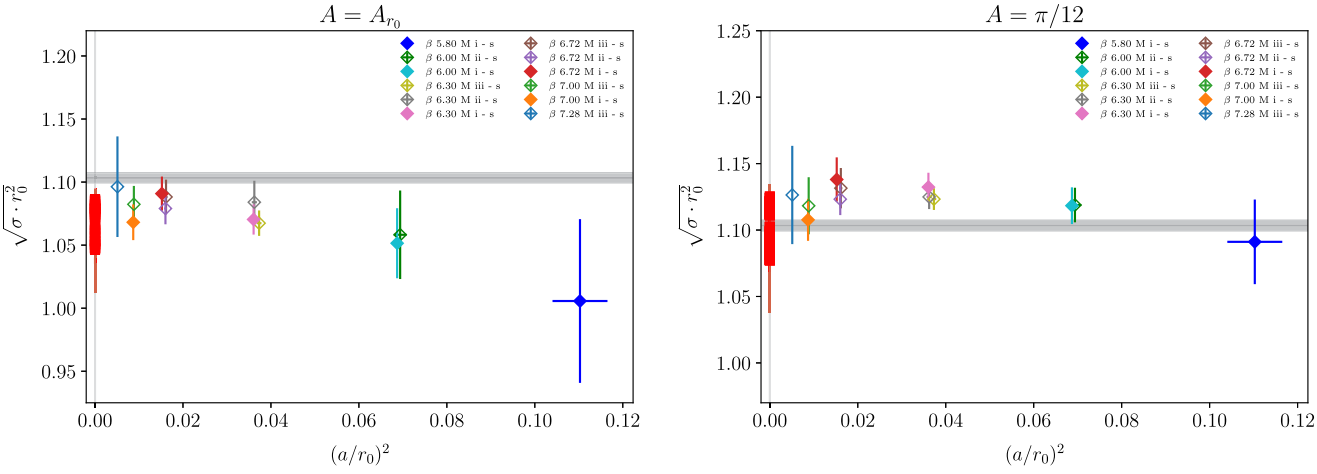

FIG. 33. Continuum results (red) and smoothened data (other colors) for $\sqrt{\sigma r_0^2}$ assuming two different coefficients A for the Coulomb term are shown in the left or right columns, respectively, as functions of $(a/r_0)^2$, using smeared links. The gray solid line and band show the published $(2+1)$-flavor QCD value [14]. The corresponding plots for bare links are shown in Fig. 16 in Sec. IV.

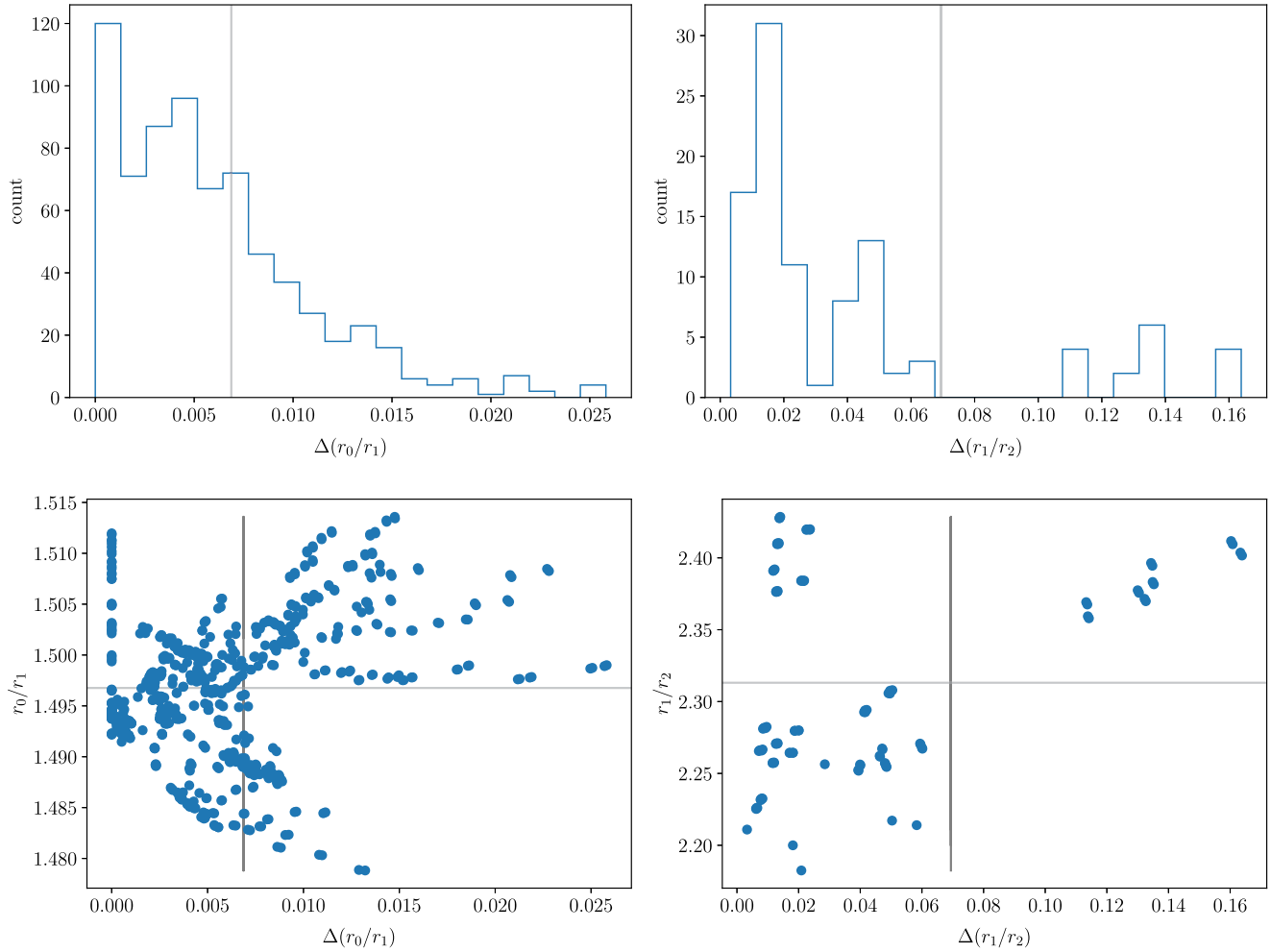

FIG. 34. Distribution of the errors (top) and correlation plots between central values and regression errors (bottom) for the ratios r_0/r_1 and r_1/r_2, respectively. The gray lines indicate our error and central value also shown in the histogram Fig. 14.

tension our error estimate is marginally larger than the bulk of the distribution of errors, and there is no clear pattern of correlation between the central value and the regression error.

APPENDIX C: PERTURBATIVE QCD FORMULAS

In this appendix, we collect various formulas obtained in perturbative QCD that are used in Sec. V. Appendix C 1 contains the perturbative expansion coefficients for the force in the case of massless quarks, Appendix C 2 provides the one- and two-loop corrections due to a massive charm quark, and in Appendix C 3 one may find the definitions of some special functions showing up in Appendix C 2.

1. Coefficients in the force and coupling at two loops

The one- and two-loop coefficients, a_i, appearing in Eqs. (5.6) and (5.7) have been computed in Refs. [110,135–138] and the three-loop coefficients, which go beyond our accuracy, in Refs. [139–142]:

$$a_1^{(N_f)} = \frac{31C_A}{9} - \frac{10}{9}N_f, \tag{C1}$$

$$a_2^{(N_f)} = \left(\frac{4343}{162} + 4\pi^2 - \frac{\pi^4}{4} + \frac{22}{3}\zeta_3\right)C_A^2 - \left(\frac{899}{81} + \frac{28}{3}\zeta_3\right)C_A N_f - \left(\frac{55}{6} - 8\zeta_3\right)C_F N_f + \frac{100}{81}N_f^2, \tag{C2}$$

$$a_3^L = \frac{16\pi^2}{3}C_A^3, \tag{C3}$$

where $C_A = N_c = 3$, and $C_F = (N_c^2 - 1)/(2N_c) = 4/3$. Note that $\zeta_n \equiv \zeta(n) = \sum_{i=1}^{\infty} 1/i^n$ is the Riemann zeta function. The logarithmic terms affecting the static force and potential are most conveniently extracted in an effective field theory framework [4,5,143], as discussed in Sec. V, and

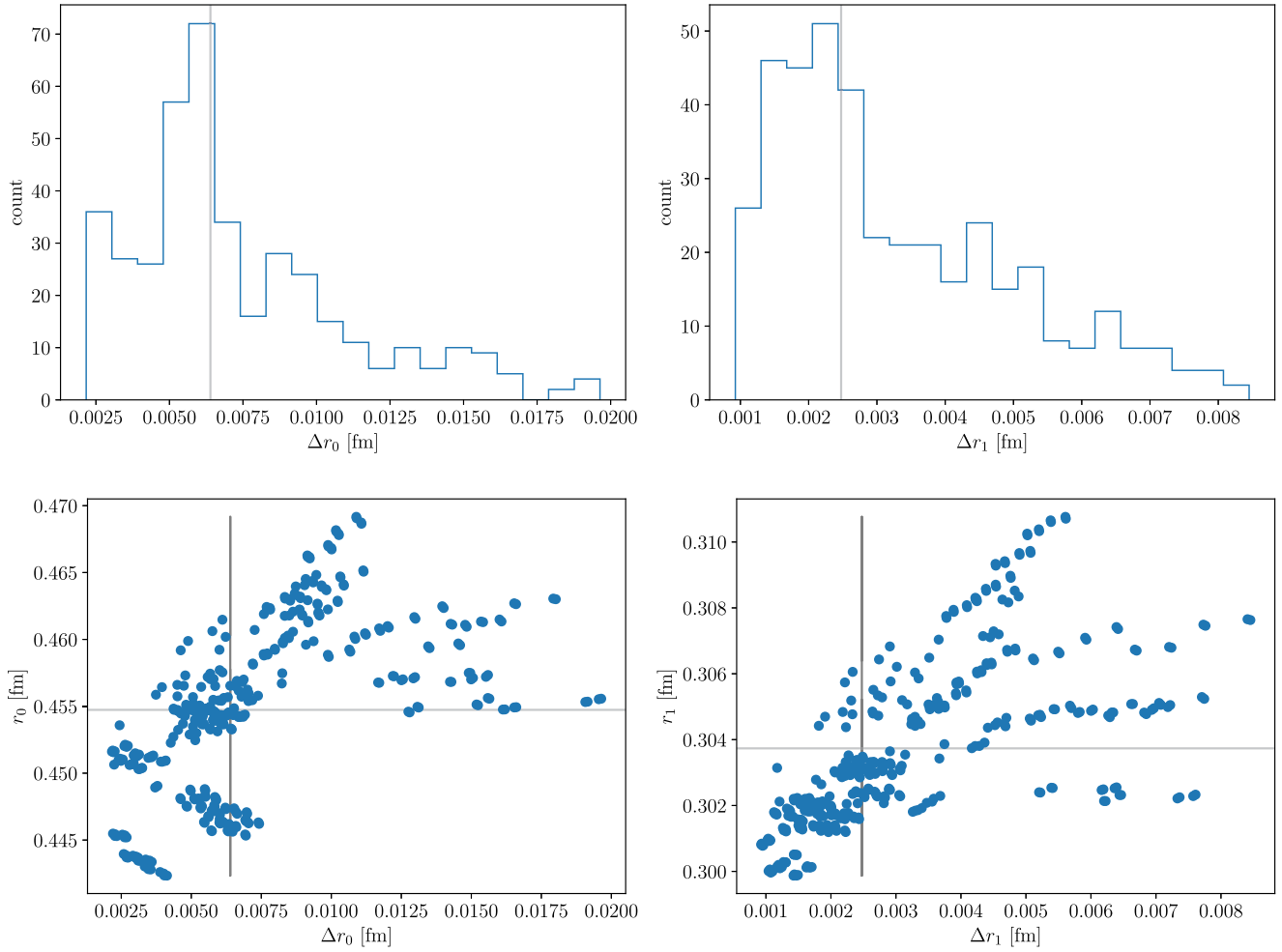

FIG. 35. Distribution of the errors (top) and correlation plots between central values and regression errors (bottom) for the scales r_0 and r_1, respectively. The gray lines indicate our error and central value also shown in the histogram Fig. 17.

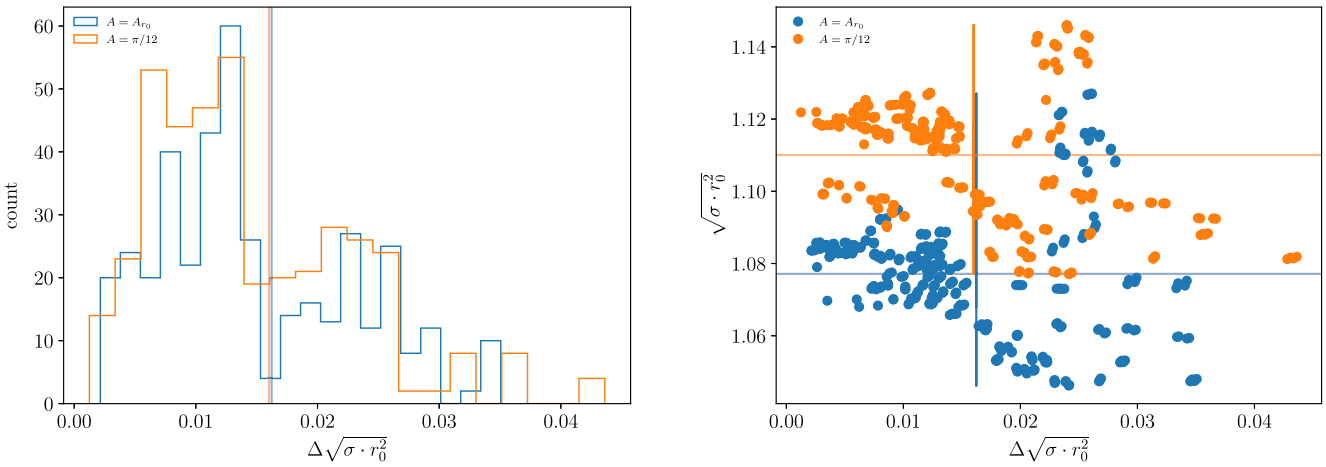

FIG. 36. Distribution of the errors (left) and correlation plots between central values and regression errors (right) for the string tension $\sqrt{\sigma r_0^2}$ for the two different choices of the Coulomb parameter, respectively. The lines indicate our errors and central values, respectively, also shown in the histogram Fig. 18.

have been computed and resummed to all orders at N^{2}LL and N^{3}LL accuracy in Refs. [4,112,113,144,145].

The running of the strong coupling $\alpha_s^{(N_f)}(\mu)$ is determined by the β-function. The first two coefficients of the β-function, $\beta_{1,2}$, are scheme independent and given by

$$\beta_0^{(N_f)} = \frac{11}{3}C_A - \frac{2}{3}N_f, \tag{C4}$$

$$\beta_1^{(N_f)} = \frac{34}{3}C_A^2 - \frac{10}{3}C_A N_f - 2C_F N_f. \tag{C5}$$

The coupling $\alpha_s^{(N_f)}(\mu)$ with N_f massless flavors is related to $\alpha_s^{(N_f-1)}(\mu)$ with $N_f - 1$ massless flavors via

$$\alpha_s^{(N_f+1)}(\mu) = \alpha_s^{(N_f)}(\mu)\left\{1 + \sum_{n=1}^{\infty}[\alpha_s^{(N_f)}(\mu)]^n\left[\sum_{l=0}^{n} c_{nl}\ln^l\left(\frac{\mu^2}{m^2}\right)\right]\right\}. \tag{C6}$$

Following [118] (see Refs. [146,147] for the four-loop decoupling), we have for the first terms

$$c_{11} = \frac{1}{6\pi}, \qquad c_{10} = 0, \tag{C7}$$

$$c_{22} = \frac{1}{36\pi^2}, \qquad c_{21} = \frac{19}{24\pi^2}, \qquad c_{20} = -\frac{11}{72\pi^2}, \tag{C8}$$

when m is the $\overline{\rm MS}$ mass renormalized at the $\overline{\rm MS}$ mass scale: $m = m^{\overline{\rm MS}}(m^{\overline{\rm MS}})$.[22]

2. Finite-mass corrections

Adding the effect of a quark of mass m to N_f massless flavors modifies the order α_s^N term in the static potential from $V^{(N_f),[N]}$ into

$$V_m^{(N_f),[N]} = V^{(N_f),[N]} + \delta V_m^{(N_f),[N]}. \tag{C9}$$

The correction due to the quark of finite mass m is known up to two-loop accuracy. The $O(\alpha_s^2)$ corrections have been computed in Refs. [114–117,148]. At $O(\alpha_s^3)$, the correction was computed first in momentum space in [115]. The Fourier transform was performed (the coordinate-space potential was studied using different integral representations in [115]) and $\delta V_m^{(N_f),[3]}(r)$ was obtained also in one-parameter integral form in [116,117]. Many of the original references contain misprints; corrected formulas can be found in Ref. [118].

At one-loop accuracy, the finite mass correction to the static potential reads

$$\delta V_m^{(N_f),[2]}(r,\nu) = -\frac{C_F\alpha_s^{(N_f)}(\nu)}{r}\frac{\alpha_s^{(N_f)}(\nu)}{3\pi}\int_1^\infty dx\, f(x)e^{-2mrx}, \tag{C10}$$

where $f(x) = \sqrt{x^2-1}/x^2(1+1/2x^2)$. At two-loop accuracy, the finite mass correction to the static potential is given by

$$\begin{aligned}\delta V_m^{(N_f),[3]}(r,\nu) = -\frac{C_F\alpha_s^{(N_f)}}{r}\left(\frac{\alpha_s^{(N_f)}}{3\pi}\right)^2 \times \Bigg\{&\left[9\pi^2(c_{20} - 2\ln(mr)(c_{21} - 2c_{22}\ln(mr))) - \ln^2(mr) + \frac{57}{4}\ln(mr) + \frac{11}{8}\right] \\ &+ \frac{57}{4}[f_1\Gamma(0, 2f_2 mr) + b_1\Gamma(0, 2b_2 mr)] + \left[-2\ln(mr) - \frac{5}{3}N_f + \frac{83}{6}\right]\int_1^\infty dx\, f(x)e^{-2mrx} \\ &+ \left(\frac{33}{2} - N_f\right)\int_1^\infty dx\, f(x)(e^{-2mrx}\,\mathrm{Ei}(2mrx) + e^{2mrx}\,\mathrm{Ei}(-2mrx) - 2\ln(2mrx)) \\ &- \int_1^\infty dx\, f(x)e^{-2mrx}\left(\frac{1}{x^2} + 2\ln(2x) + 8mrx + f(x)x\ln\frac{x-\sqrt{x^2-1}}{x+\sqrt{x^2-1}}\right)\Bigg\},\end{aligned} \tag{C11}$$

[22] In the PDG [99] and in Refs. [146,147] the coefficient c_{21} reads $11/(24\pi^2)$ because there the $\overline{\rm MS}$ mass m in the decoupling relation (C6) is taken at the renormalization scale μ. We follow Ref. [118] and understand the $\overline{\rm MS}$ mass m in Eq. (C6) as computed at the $\overline{\rm MS}$ mass scale.

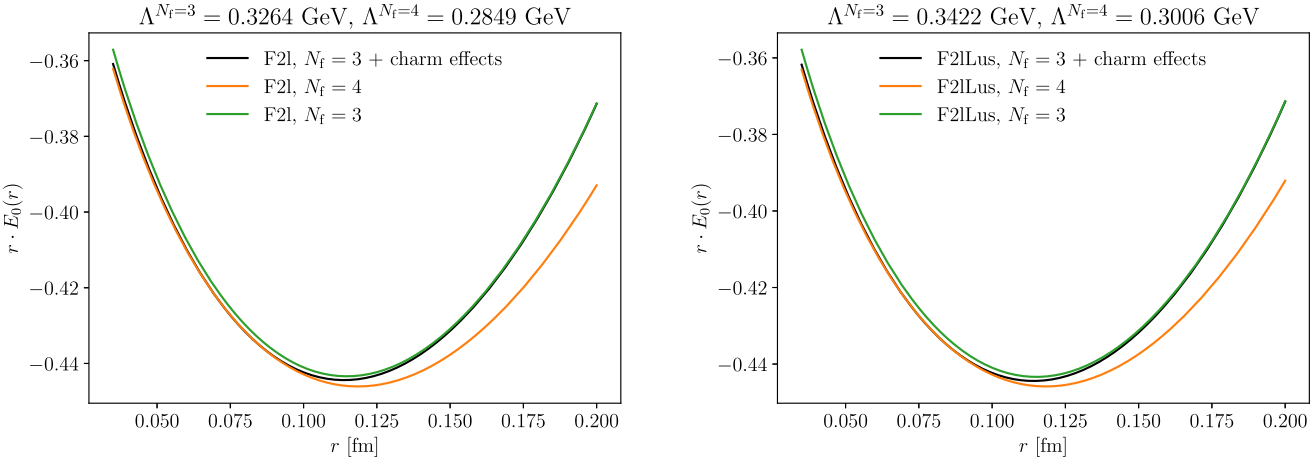

FIG. 37. Left: static energy obtained from integrating the static force at two loops, Eq. (5.6), for $N_f = 4$ (orange curve), $N_f = 3$ (green curve), and for $N_f = 3$ plus the two-loop charm-mass correction using $m_c^{\overline{MS}}(m_c^{\overline{MS}}) = 1.28$ GeV (black curve); all curves using three-loop running of α_s. The $N_f = 4$ curve has been matched to the $N_f = 3$ plus the two-loop charm-mass correction curve at 0.08 fm by shifting the static energy by a constant. Right: like left but with the static force computed at N^{2}LL accuracy, Eq. (5.7).

where[23]

$$f_1 = \frac{\ln A - \ln b_2}{\ln f_2 - \ln b_2}, \qquad b_1 = \frac{\ln A - \ln f_2}{\ln b_2 - \ln f_2},$$
$$f_2 = 0.470 \pm 0.005, \qquad b_2 = 1.120 \pm 0.010,$$
$$\ln A = 161/228 + 13\zeta_3/19 - \ln 2. \tag{C12}$$

In Eq. (C11), Ei denotes the exponential-integral function and Γ with two arguments denotes the incomplete gamma function. Their definitions and some useful properties can be found in Appendix C 3. The mass m in the above formulas is the $\overline{\text{MS}}$ mass renormalized at the $\overline{\text{MS}}$ mass scale: $m = m^{\overline{\text{MS}}}(m^{\overline{\text{MS}}})$.[24]

Decoupling requires that

$$V_m^{(N_f),[N]}(r,\nu) \to V^{(N_f),[N]}(r,\nu), \quad \text{for } m \to \infty, \tag{C13}$$

and

$$V_m^{(N_f),[N]}(r,\nu) \to V^{(N_f+1),[N]}(r,\nu) + \mathrm{O}((\alpha_s^{(N_f)})^{N+1}), \quad \text{for } m \to 0. \tag{C14}$$

One can verify analytically from the above expressions that the expected decoupling conditions hold in the limits $m \to \infty$ and $m \to 0$ at one ($N = 2$) and two ($N = 3$) loops. For a numerical verification at two loops see Fig. 37. Since we use expressions with N_f flavors in the right-hand side of Eq. (C9), the decoupling (C13) is exact in the $m \to \infty$ limit. Hence, in Fig. 37 the $N_f = 3$ green curve overlaps exactly at large distances with the black curve obtained from the $N_f = 3$ static energy plus charm-mass corrections. In contrast, the decoupling in Eq. (C14) gets higher-order corrections when expressing the three flavor coupling in terms of the four flavor one. In order to account for these higher-order corrections, in Fig. 37 we have matched the $N_f = 4$ orange curve with the black one at 0.08 fm by adding a small constant to the static energy. The curves show the expected behavior, i.e., the curve with charm-mass effects interpolates smoothly between the $N_f = 4$ one at the short distances ($m_c \ll 1/r$) and the $N_f = 3$ one at large distances ($m_c \gg 1/r$).

3. Special functions

The exponential-integral function is given by

$$\mathrm{Ei}(x) = -\int_{-x}^{\infty} \mathrm{d}t \frac{\mathrm{e}^{-t}}{t} = \int_{-\infty}^{x} \mathrm{d}t \frac{\mathrm{e}^{t}}{t}, \tag{C15}$$

fulfilling (for $x > 0$) the relation

$$\mathrm{Ei}(-x) = -\mathrm{Ei}(1,x), \tag{C16}$$

where

$$\mathrm{Ei}(1,x) = \int_x^{\infty} \mathrm{d}t \frac{\mathrm{e}^{-t}}{t} = \int_1^{\infty} \mathrm{d}t \frac{\mathrm{e}^{-tx}}{t} = \int_0^{1} \mathrm{d}t \frac{\mathrm{e}^{-x/t}}{t}$$
$$= -\gamma_E - \ln(x) + \int_0^{x} \mathrm{d}t \frac{1-\mathrm{e}^{-t}}{t} \xrightarrow[x\to 0]{} -\gamma_E - \ln(x). \tag{C17}$$

[23]This parametrization matches the one from Ref. [117] when renaming $f \to c$ and $b \to d$.

[24]For the numerical evaluation of the above integrals, it is convenient to introduce the coordinate transformation $x \to 1/\sqrt{1-v^2}$, $\mathrm{d}x \to v(1-v^2)^{-3/2}\mathrm{d}v$, that transforms the integral boundaries from $(1,\infty)$ to $(0,1)$.

Note that $\mathrm{Ei}(1,x)$ is the $n=1$ case of the general E_n-function defined via

$$\mathrm{E}_n(x) \equiv \mathrm{Ei}(n,x) = \int_1^\infty \mathrm{d}t \frac{\mathrm{e}^{-xt}}{t^n} = x^{n-1}\Gamma(1-n,x). \tag{C18}$$

Γ with two arguments is the (upper) incomplete gamma function,

$$\Gamma(a,x) = \int_x^\infty \mathrm{d}t\, t^{a-1}\mathrm{e}^{-t} \underset{a\to 0}{\longrightarrow} \mathrm{Ei}(1,x). \tag{C19}$$

It can be expressed in terms of the regular gamma function and the lower incomplete gamma function as

$$\Gamma(a,x) = \Gamma(a) - \gamma(a,x), \tag{C20}$$

where

$$\gamma(a,x) = \frac{x^a}{a} + \sum_{k=1}^\infty \frac{(-1)^k}{k!(a+k)} x^{a+k}, \tag{C21}$$

such that

$$\Gamma(a,x) = \Gamma(a) - \frac{x^a}{a} - \sum_{k=1}^\infty \frac{(-1)^k}{k!(a+k)} x^{a+k} \underset{x\to 0}{\longrightarrow} -\frac{x^a}{a}, \quad \text{for } a<0. \tag{C22}$$

[1] K. G. Wilson, Confinement of quarks, Phys. Rev. D **10**, 2445 (1974).
[2] G. S. Bali, QCD forces and heavy quark bound states, Phys. Rep. **343**, 1 (2001).
[3] T. Appelquist, M. Dine, and I. J. Muzinich, The static limit of quantum chromodynamics, Phys. Rev. D **17**, 2074 (1978).
[4] N. Brambilla, A. Pineda, J. Soto, and A. Vairo, The infrared behavior of the static potential in perturbative QCD, Phys. Rev. D **60**, 091502 (1999).
[5] N. Brambilla, A. Pineda, J. Soto, and A. Vairo, Potential NRQCD: An effective theory for heavy quarkonium, Nucl. Phys. **B566**, 275 (2000).
[6] A. H. Hoang, M. C. Smith, T. Stelzer, and S. Willenbrock, Quarkonia and the pole mass, Phys. Rev. D **59**, 114014 (1999).
[7] A. Pineda, Heavy quarkonium and non-relativistic effective field theories, Ph.D. thesis, University of Barcelona, 1998.
[8] S. Necco and R. Sommer, The $N_\mathrm{f}=0$ heavy quark potential from short to intermediate distances, Nucl. Phys. **B622**, 328 (2002).
[9] R. Sommer, A new way to set the energy scale in lattice gauge theories and its applications to the static force and α_s in $SU(2)$ Yang-Mills theory, Nucl. Phys. **B411**, 839 (1994).
[10] C. W. Bernard, T. Burch, K. Orginos, D. Toussaint, T. A. DeGrand, C. E. DeTar, S. A. Gottlieb, U. M. Heller, J. E. Hetrick, and B. Sugar, The static quark potential in three-flavor QCD, Phys. Rev. D **62**, 034503 (2000).
[11] A. Bazavov, P. Petreczky, and J. H. Weber, Equation of state in $(2+1)$-flavor QCD at high temperatures, Phys. Rev. D **97**, 014510 (2018).
[12] C. Aubin, C. Bernard, C. DeTar, J. Osborn, S. Gottlieb, E. B. Gregory, D. Toussaint, U. M. Heller, J. E. Hetrick, and R. Sugar, Light hadrons with improved staggered quarks: Approaching the continuum limit, Phys. Rev. D **70**, 094505 (2004).
[13] M. Cheng *et al.*, The transition temperature in QCD, Phys. Rev. D **74**, 054507 (2006).
[14] M. Cheng *et al.*, The QCD equation of state with almost physical quark masses, Phys. Rev. D **77**, 014511 (2008).
[15] A. Bazavov *et al.*, The chiral and deconfinement aspects of the QCD transition, Phys. Rev. D **85**, 054503 (2012).
[16] A. Bazavov *et al.* (HotQCD Collaboration), Equation of state in $(2+1)$-flavor QCD, Phys. Rev. D **90**, 094503 (2014).
[17] A. Bazavov, N. Brambilla, X. Garcia i Tormo, P. Petreczky, J. Soto, A. Vairo, and J. H. Weber (TUMQCD Collaboration), Determination of the QCD coupling from the static energy and the free energy, Phys. Rev. D **100**, 114511 (2019).
[18] A. Bazavov *et al.* (MILC Collaboration), Scaling studies of QCD with the dynamical HISQ action, Phys. Rev. D **82**, 074501 (2010).
[19] A. Bazavov *et al.* (MILC Collaboration), Lattice QCD ensembles with four flavors of highly improved staggered quarks, Phys. Rev. D **87**, 054505 (2013).
[20] E. Follana, Q. Mason, C. Davies, K. Hornbostel, G. P. Lepage, J. Shigemitsu, H. Trottier, and K. Wong (HPQCD Collaboration), Highly improved staggered quarks on the lattice, with applications to charm physics, Phys. Rev. D **75**, 054502 (2007).
[21] K. Symanzik, Continuum limit and improved action in lattice theories 1: Principles and ϕ^4 theory, Nucl. Phys. **B226**, 187 (1983); Continuum limit and improved action in lattice theories 2: $O(N)$ Nonlinear sigma model in perturbation theory, Nucl. Phys. **B226**, 205 (1983).
[22] M. Lüscher and P. Weisz, On-shell improved lattice gauge theories, Commun. Math. Phys. **97**, 59 (1985); **98**, 433(E) (1985).

[23] M. Lüscher and P. Weisz, Computation of the action for on-shell improved lattice gauge theories at weak coupling, Phys. Lett. **158B**, 250 (1985); Efficient numerical techniques for perturbative lattice gauge theory computations, Nucl. Phys. **B266**, 309 (1986).

[24] Z. Hao, G. M. von Hippel, R. R. Horgan, Q. J. Mason, and H. D. Trottier, Unquenching effects on the coefficients of the Lüscher-Weisz action, Phys. Rev. D **76**, 034507 (2007); A. Hart, G. M. von Hippel, and R. R. Horgan (HPQCD Collaboration), Radiative corrections to the lattice gluon action for HISQ improved staggered quarks and the effect of such corrections on the static potential, Phys. Rev. D **79**, 074008 (2009).

[25] N. Carrasco *et al.* (European Twisted Mass Collaboration), Up, down, strange and charm quark masses with $N_f = 2+1+1$ twisted mass lattice QCD, Nucl. Phys. **B887**, 19 (2014).

[26] A. Bazavov *et al.* (Fermilab Lattice and MILC Collaborations), B- and D-meson leptonic decay constants from four-flavor lattice QCD, Phys. Rev. D **98**, 074512 (2018).

[27] E. B. Gregory *et al.* (HPQCD Collaboration), Precise B, B_s and B_c meson spectroscopy from full lattice QCD, Phys. Rev. D **83**, 014506 (2011).

[28] E. B. Gregory, A. C. Irving, C. M. Richards, and C. McNeile (UKQCD Collaboration), A study of the η and η' mesons with improved staggered fermions, Phys. Rev. D **86**, 014504 (2012).

[29] R. A. Briceño, H.-W. Lin, and D. R. Bolton, Charmed-Baryon spectroscopy from lattice QCD with $N_f = 2+1+1$ flavors, Phys. Rev. D **86**, 094504 (2012).

[30] R. J. Dowdall, C. T. H. Davies, T. C. Hammant, and R. R. Horgan (HPQCD Collaboration), Precise heavy-light meson masses and hyperfine splittings from lattice QCD including charm quarks in the sea, Phys. Rev. D **86**, 094510 (2012).

[31] C. Hughes, E. Eichten, and C. T. H. Davies, Searching for beauty-fully bound tetraquarks using lattice nonrelativistic QCD, Phys. Rev. D **97**, 054505 (2018).

[32] Y. Lin, A. S. Meyer, C. Hughes, A. S. Kronfeld, J. N. Simone, and A. Strelchenko (Fermilab Lattice Collaboration), nucleon mass with highly improved staggered quarks, Phys. Rev. D **103**, 034501 (2021).

[33] A. Bazavov *et al.* (MILC Collaboration), Leptonic Decay-Constant Ratio f_{K^+}/f_{π^+} from Lattice QCD with Physical Light Quarks, Phys. Rev. Lett. **110**, 172003 (2013).

[34] R. J. Dowdall, C. T. H. Davies, G. P. Lepage, and C. McNeile (HPQCD Collaboration), V_{us} from π and K decay constants in full lattice QCD with physical u, d, s, and c quarks, Phys. Rev. D **88**, 074504 (2013).

[35] R. J. Dowdall, C. T. H. Davies, R. R. Horgan, C. J. Monahan, and J. Shigemitsu (HPQCD Collaboration), B-Meson Decay Constants from Improved Lattice Nonrelativistic QCD with Physical u, d, s, and c Quarks, Phys. Rev. Lett. **110**, 222003 (2013).

[36] A. Bazavov *et al.* (Fermilab Lattice and MILC Collaborations), Charmed and light pseudoscalar meson decay constants from four-flavor lattice QCD with physical light quarks, Phys. Rev. D **90**, 074509 (2014).

[37] B. Colquhoun, C. T. H. Davies, R. J. Dowdall, J. Kettle, J. Koponen, G. P. Lepage, and A. T. Lytle (HPQCD Collaboration), B-meson decay constants: A more complete picture from full lattice QCD, Phys. Rev. D **91**, 114509 (2015).

[38] C. Hughes, C. T. H. Davies, and C. J. Monahan (HPQCD Collaboration), New methods for B meson decay constants and form factors from lattice NRQCD, Phys. Rev. D **97**, 054509 (2018).

[39] D. Hatton, C. T. H. Davies, G. P. Lepage, and A. T. Lytle (HPQCD Collaboration), Renormalization of the tensor current in lattice QCD and the J/ψ tensor decay constant, Phys. Rev. D **102**, 094509 (2020).

[40] C. McNeile, A. Bazavov, C. T. H. Davies, R. J. Dowdall, K. Hornbostel, G. P. Lepage, and H. D. Trottier, Direct determination of the strange and light quark condensates from full lattice QCD, Phys. Rev. D **87**, 034503 (2013).

[41] B. Chakraborty, C. T. H. Davies, G. C. Donald, R. J. Dowdall, J. Koponen, G. P. Lepage, and T. Teubner (HPQCD Collaboration), Strange and charm quark contributions to the anomalous magnetic moment of the muon, Phys. Rev. D **89**, 114501 (2014).

[42] B. Chakraborty, C. T. H. Davies, P. G. de Oliviera, J. Koponen, G. P. Lepage, and R. S. Van de Water (HPQCD Collaboration), The hadronic vacuum polarization contribution to a_μ from full lattice QCD, Phys. Rev. D **96**, 034516 (2017).

[43] B. Chakraborty *et al.* (Fermilab Lattice, HPQCD, and MILC Collaborations), Strong-Isospin-Breaking Correction to the Muon Anomalous Magnetic Moment from Lattice QCD at the Physical Point, Phys. Rev. Lett. **120**, 152001 (2018).

[44] C. T. H. Davies *et al.* (Fermilab Lattice, HPQCD, and MILC Collaboration), Hadronic-vacuum-polarization contribution to the muon's anomalous magnetic moment from four-flavor lattice QCD, Phys. Rev. D **101**, 034512 (2020).

[45] B. Chakraborty, C. T. H. Davies, B. Galloway, P. Knecht, J. Koponen, G. C. Donald, R. J. Dowdall, G. P. Lepage, and C. McNeile (HPQCD Collaboration), High-precision quark masses and QCD coupling from $N_f = 4$ lattice QCD, Phys. Rev. D **91**, 054508 (2015).

[46] A. Bazavov *et al.* (Fermilab Lattice, MILC, and TUMQCD Collaborations), Up-, down-, strange-, charm-, and bottom-quark masses from four-flavor lattice QCD, Phys. Rev. D **98**, 054517 (2018).

[47] A. T. Lytle, C. T. H. Davies, D. Hatton, G. P. Lepage, and C. Sturm (HPQCD Collaboration), Determination of quark masses from $N_f = 4$ lattice QCD and the RI-SMOM intermediate scheme, Phys. Rev. D **98**, 014513 (2018).

[48] C. Hughes, R. J. Dowdall, C. T. H. Davies, R. R. Horgan, G. von Hippel, and M. Wingate (HPQCD Collaboration), Hindered M1 radiative decay of $\Upsilon(2S)$ from lattice NRQCD, Phys. Rev. D **92**, 094501 (2015).

[49] J. Koponen, F. Bursa, C. T. H. Davies, R. J. Dowdall, and G. P. Lepage (HPQCD Collaboration), Size of the pion from full lattice QCD with physical u, d, s, and c quarks, Phys. Rev. D **93**, 054503 (2016).

[50] J. Koponen, A. C. Zimermmane-Santos, C. T. H. Davies, G. P. Lepage, and A. T. Lytle (HPQCD Collaboration), Pseudoscalar meson electromagnetic form factor at high Q^2 from full lattice QCD, Phys. Rev. D **96**, 054501 (2017).

[51] A. Bazavov *et al.* (Fermilab Lattice and MILC Collaborations), Determination of $|V_{us}|$ from a Lattice-QCD Calculation of the $K \to \pi \ell \nu$ Semileptonic Form Factor with Physical Quark Masses, Phys. Rev. Lett. **112**, 112001 (2014).

[52] A. Bazavov *et al.* (Fermilab Lattice and MILC Collaborations), $|V_{us}|$ from $K_{\ell 3}$ decay and four-flavor lattice QCD, Phys. Rev. D **99**, 114509 (2019).

[53] J. Harrison, C. Davies, and M. Wingate (HPQCD Collaboration), Lattice QCD calculation of the $B_{(s)} \to D^*_{(s)} \ell \nu$ form factors at zero recoil and implications for $|V_{cb}|$, Phys. Rev. D **97**, 054502 (2018).

[54] E. McLean, C. T. H. Davies, A. T. Lytle, and J. Koponen, Lattice QCD form factor for $B_s \to D_s^* \ell \nu$ at zero recoil with non-perturbative current renormalisation, Phys. Rev. D **99**, 114512 (2019).

[55] E. McLean, C. T. H. Davies, J. Koponen, and A. T. Lytle, $B_s \to D_s \ell \nu$ Form factors for the full q^2 range from lattice QCD with non-perturbatively normalized currents, Phys. Rev. D **101**, 074513 (2020).

[56] R. J. Dowdall, C. T. H. Davies, R. R. Horgan, G. P. Lepage, C. J. Monahan, J. Shigemitsu, and M. Wingate, Neutral B-meson mixing from full lattice QCD at the physical point, Phys. Rev. D **100**, 094508 (2019).

[57] C. T. H. Davies, J. Harrison, G. P. Lepage, C. J. Monahan, J. Shigemitsu, and M. Wingate (HPQCD Collaboration), Lattice QCD Matrix Elements for the $B_s^0 - \bar{B}_s^0$ Width Difference Beyond Leading Order, Phys. Rev. Lett. **124**, 082001 (2020).

[58] L. J. Cooper, C. T. H. Davies, J. Harrison, J. Komijani, and M. Wingate (HPQCD Collaboration), $B_c \to B_{s(d)}$ form factors from lattice QCD, Phys. Rev. D **102**, 014513 (2020).

[59] J. Harrison, C. T. H. Davies, and A. Lytle (HPQCD Collaboration), $B_c \to J/\psi$ form factors for the full q^2 range from lattice QCD, Phys. Rev. D **102**, 094518 (2020).

[60] R. Baron *et al.* (ETM Collaboration), Light hadrons from lattice QCD with light (u, d), strange and charm dynamical quarks, J. High Energy Phys. 06 (2010) 111.

[61] R. Baron *et al.* (ETM Collaboration), Computing K and D meson masses with $N_f = 2 + 1 + 1$ twisted mass lattice QCD, Comput. Phys. Commun. **182**, 299 (2011).

[62] K. Ottnad, C. Michael, S. Reker, C. Urbach, C. Michael, S. Reker, and C. Urbach (ETM Collaboration), η and η' mesons from $N_f = 2 + 1 + 1$ twisted mass lattice QCD, J. High Energy Phys. 11 (2012) 048.

[63] D. d'Enterria *et al.*, The strong coupling constant: State of the art and the decade ahead, arXiv:2203.08271.

[64] S. Necco and R. Sommer, Testing perturbation theory on the $N_f = 0$ static quark potential, Phys. Lett. B **523**, 135 (2001).

[65] A. Pineda, The static potential: Lattice versus perturbation theory in a renormalon based approach, J. Phys. G **29**, 371 (2003).

[66] N. Brambilla, X. Garcia i Tormo, J. Soto, and A. Vairo, Precision Determination of $r_0 \Lambda_{\overline{\rm MS}}$ from the QCD Static Energy, Phys. Rev. Lett. **105**, 212001 (2010); **108**, 269903(E) (2012).

[67] A. Bazavov, N. Brambilla, X. Garcia i Tormo, P. Petreczky, J. Soto, and A. Vairo, Determination of α_s from the QCD static energy, Phys. Rev. D **86**, 114031 (2012).

[68] A. Bazavov, N. Brambilla, X. Garcia i Tormo, P. Petreczky, J. Soto, and A. Vairo, Determination of α_s from the QCD static energy: An update, Phys. Rev. D **90**, 074038 (2014); **101**, 119902(E) (2020).

[69] H. Takaura, T. Kaneko, Y. Kiyo, and Y. Sumino, Determination of α_s from static QCD potential with renormalon subtraction, Phys. Lett. B **789**, 598 (2019).

[70] C. Ayala, X. Lobregat, and A. Pineda, Determination of $\alpha(M_Z)$ from an hyperasymptotic approximation to the energy of a static quark-antiquark pair, J. High Energy Phys. 09 (2020) 016.

[71] S. Cali, F. Knechtli, T. Korzec, and H. Panagopoulos, Charm quark effects on the strong coupling extracted from the static force, EPJ Web Conf. **175**, 10002 (2018).

[72] M. Dalla Brida, R. Höllwieser, F. Knechtli, T. Korzec, A. Ramos, and R. Sommer (ALPHA Collaboration), Nonperturbative renormalization by decoupling, Phys. Lett. B **807**, 135571 (2020).

[73] S. Steinbeißer, N. Brambilla, R. L. Delgado, A. S. Kronfeld, V. Leino, P. Petreczky, A. Vairo, and J. H. Weber (TUMQCD Collaboration), The static energy in $(2 + 1 + 1)$-flavor QCD, Proc. Sci. LATTICE2021 (**2022**) 521 [arXiv:2111.02288].

[74] J. H. Weber, A. Bazavov, and P. Petreczky, Equation of state in $(2 + 1)$-flavor QCD at high temperatures, Proc. Sci. Confinement2018 (**2019**) 166 [arXiv:1811.12902].

[75] G. P. Lepage and P. B. Mackenzie, On the viability of lattice perturbation theory, Phys. Rev. D **48**, 2250 (1993).

[76] C. T. H. Davies, E. Follana, I. D. Kendall, G. P. Lepage, and C. McNeile (HPQCD Collaboration), Precise determination of the lattice spacing in full lattice QCD, Phys. Rev. D **81**, 034506 (2010).

[77] A. Bazavov *et al.*, Simulations with dynamical HISQ quarks, Proc. Sci. LATTICE2010 (**2010**) 320 [arXiv:1012.1265].

[78] MILC Collaboration (private communication).

[79] A. Hasenfratz and F. Knechtli, Flavor symmetry and the static potential with hypercubic blocking, Phys. Rev. D **64**, 034504 (2001).

[80] C. Michael and A. McKerrell, Fitting correlated hadron mass spectrum data, Phys. Rev. D **51**, 3745 (1995).

[81] R Core Team, *R: A Language and Environment for Statistical Computing* (R Foundation for Statistical Computing, Vienna, Austria, 2022).

[82] J. Pinheiro, D. Bates, S. DebRoy, D. Sarkar, S. Heisterkamp, B. V. Willigen, and J. Ranke, *NLME: Linear and Nonlinear Mixed Effects Models*, R package version 3.1-157 (R Core Team, 2022).

[83] K. J. Juge, J. Kuti, and C. Morningstar, Fine Structure of the QCD String Spectrum, Phys. Rev. Lett. **90**, 161601 (2003); C. Morningstar (private communication).

[84] D. Bala, O. Kaczmarek, R. Larsen, S. Mukherjee, G. Parkar, P. Petreczky, A. Rothkopf, and J. H. Weber (HotQCD Collaboration), Static quark-antiquark interactions at nonzero temperature from lattice QCD, Phys. Rev. D **105**, 054513 (2022).

[85] A. Bazavov *et al.* (Fermilab Lattice and MILC Collaborations), $B^0_{(s)}$-mixing matrix elements from lattice QCD for the Standard Model and beyond, Phys. Rev. D **93**, 113016 (2016).

[86] See Supplemental Material at http://link.aps.org/supplemental/10.1103/PhysRevD.107.074503 for machine-readable covariance matrices and human-readable lists of various fit results.

[87] A. Bazavov *et al.* (MILC Collaboration), Results for light pseudoscalar mesons, Proc. Sci. LATTICE2010 (**2010**) 074 [arXiv:1012.0868].

[88] C. R. Allton, Lattice Monte Carlo data versus perturbation theory, arXiv:hep-lat/9610016.

[89] A. Bazavov *et al.* (MILC Collaboration), Nonperturbative QCD simulations with $(2+1)$-flavors of improved staggered quarks, Rev. Mod. Phys. **82**, 1349 (2010).

[90] A. Hart, G. M. von Hippel, R. R. Horgan, and L. C. Storoni, Automatically generating Feynman rules for improved lattice field theories, J. Comput. Phys. **209**, 340 (2005).

[91] A. Hart, G. M. von Hippel, R. R. Horgan, and E. H. Muller, Automated generation of lattice QCD Feynman rules, Comput. Phys. Commun. **180**, 2698 (2009).

[92] G. M. von Hippel, V. Leino, and S. Steinbeißer (TUMQCD Collaboration), Report No. TUM-EFT 171/22 (to be published).

[93] A. Bazavov, N. Brambilla, P. Petreczky, A. Vairo, and J. H. Weber (TUMQCD Collaboration), Color screening in $(2+1)$-flavor QCD, Phys. Rev. D **98**, 054511 (2018).

[94] J. Komijani, P. Petreczky, and J. H. Weber, Strong coupling constant and quark masses from lattice QCD, Prog. Part. Nucl. Phys. **113**, 103788 (2020).

[95] M. Lüscher, Symmetry breaking aspects of the roughening transition in gauge theories, Nucl. Phys. **B180**, 317 (1981).

[96] Y. Aoki *et al.*, FLAG review 2021, Eur. Phys. J. C **82**, 869 (2022).

[97] P. T. Boggs and J. E. Rogers, Orthogonal distance regression, Contemp. Math. **112**, 183 (1990).

[98] M. Gell-Mann, R. J. Oakes, and B. Renner, Behavior of current divergences under $SU(3) \times SU(3)$, Phys. Rev. **175**, 2195 (1968).

[99] P. A. Zyla *et al.* (Particle Data Group), Review of particle physics, Prog. Theor. Exp. Phys. **2020**, 083C01 (2020).

[100] H. Akaike, A new look at the statistical model identification, IEEE Trans. Autom. Control **19**, 716 (1974).

[101] J. M. Cavanaugh, Unifying the derivations for the Akaike and corrected Akaike information criteria, Stat. Probab. Lett. **33**, 201 (1997).

[102] W. I. Jay and E. T. Neil, Bayesian model averaging for analysis of lattice field theory results, Phys. Rev. D **103**, 114502 (2021).

[103] Y. Aoki *et al.* (RBC and UKQCD Collaborations), Continuum limit physics from $(2+1)$-flavor domain wall QCD, Phys. Rev. D **83**, 074508 (2011).

[104] Y. Aoki, S. Borsanyi, S. Durr, Z. Fodor, S. D. Katz, S. Krieg, and K. K. Szabo, The QCD transition temperature: Results with physical masses in the continuum limit II, J. High Energy Phys. 06 (2009) 088.

[105] A. Gray, I. Allison, C. T. H. Davies, E. Dalgic, G. P. Lepage, J. Shigemitsu, and M. Wingate, The Υ spectrum and m_b from full lattice QCD, Phys. Rev. D **72**, 094507 (2005).

[106] S. Aoki *et al.* (PACS-CS Collaboration), $(2+1)$-flavor lattice QCD toward the physical point, Phys. Rev. D **79**, 034503 (2009).

[107] Y.-B. Yang *et al.*, Charm and strange quark masses and f_{D_s} from overlap fermions, Phys. Rev. D **92**, 034517 (2015).

[108] R. J. Dowdall *et al.* (HPQCD Collaboration), The upsilon spectrum and the determination of the lattice spacing from lattice QCD including charm quarks in the sea, Phys. Rev. D **85**, 054509 (2012).

[109] L. Susskind, Coarse grained quantum chromodynamics, in *Ecole d'Ete de Physique Theorique: Weak and Electromagnetic Interactions at High Energy*, edited by R. Balian and C. Llewellyn Smith (North Holland, Amsterdam, 1976).

[110] W. Fischler, Quark-antiquark potential in QCD, Nucl. Phys. **B129**, 157 (1977).

[111] L. S. Brown and W. I. Weisberger, Remarks on the static potential in quantum chromodynamics, Phys. Rev. D **20**, 3239 (1979).

[112] A. Pineda and J. Soto, The renormalization group improvement of the QCD static potentials, Phys. Lett. B **495**, 323 (2000).

[113] N. Brambilla, A. Vairo, X. Garcia i Tormo, and J. Soto, The QCD static energy at N^3LL, Phys. Rev. D **80**, 034016 (2009).

[114] D. Eiras and J. Soto, Effective field theory approach to pionium, Phys. Rev. D **61**, 114027 (2000).

[115] M. Melles, The static QCD potential in coordinate space with quark masses through two loops, Phys. Rev. D **62**, 074019 (2000).

[116] M. Melles, Two loop mass effects in the static position space QCD potential, Nucl. Phys. B, Proc. Suppl. **96**, 472 (2001).

[117] A. H. Hoang, Bottom quark mass from Υ mesons: Charm mass effects, arXiv:hep-ph/0008102.

[118] S. Recksiegel and Y. Sumino, Perturbative QCD potential, renormalon cancellation and phenomenological potentials, Phys. Rev. D **65**, 054018 (2002).

[119] K. G. Chetyrkin, J. H. Kühn, and M. Steinhauser, RunDec: A mathematica package for running and decoupling of the strong coupling and quark masses, Comput. Phys. Commun. **133**, 43 (2000).

[120] B. Schmidt and M. Steinhauser, CRunDec: A C++ package for running and decoupling of the strong coupling and quark masses, Comput. Phys. Commun. **183**, 1845 (2012).

[121] F. Herren and M. Steinhauser, Version 3 of RunDec and CRunDec, Comput. Phys. Commun. **224**, 333 (2018).

[122] H. Takaura, T. Kaneko, Y. Kiyo, and Y. Sumino, Determination of α_s from static QCD potential: OPE with renormalon subtraction and lattice QCD, J. High Energy Phys. 04 (2019) 155.

[123] www.origins-cluster.de.

[124] G. Van Rossum and F. L. Drake, *Python 3 Reference Manual* (CreateSpace, Scotts Valley, CA, 2009).

[125] T. E. Oliphant, Python for scientific computing, Comput. Sci. Eng. **9**, 10 (2007).

[126] K. J. Millman and M. Aivazis, Python for scientists and engineers, Comput. Sci. Eng. **13**, 9 (2011).
[127] P. Lepage, C. Gohlke, and D. Hackett, gplepage/gvar: GVAR (2022), 10.5281/zenodo.6350630.
[128] J. D. Hunter, Matplotlib: A 2D graphics environment, Comput. Sci. Eng. **9**, 90 (2007).
[129] T. E. Oliphant, *A Guide to NumPy* (Trelgol Publishing USA, 2006), Vol. 1.
[130] S. van der Walt, S. C. Colbert, and G. Varoquaux, The NumPy array: A structure for efficient numerical computation, Comput. Sci. Eng. **13**, 22 (2011).
[131] C. R. Harris *et al.*, Array programming with NumPy, Nature (London) **585**, 357 (2020).
[132] The Pandas Development Team, pandas-dev/pandas: PANDAS (2020), 10.5281/zenodo.3509134.
[133] Wes McKinney, Data structures for statistical computing in Python, in *Proceedings of the 9th Python in Science Conference*, edited by Stéfan van der Walt and Jarrod Millman (2010), pp. 56–61, 10.25080/Majora-92bf1922-00a.
[134] P. Virtanen, R. Gommers, T. E. Oliphant *et al.*, SciPy 1.0: Fundamental algorithms for scientific computing in Python, Nat. Methods **17**, 261 (2020).
[135] A. Billoire, How heavy must quarks be in order to build Coulombic $q\bar{q}$ bound states?, Phys. Lett. **92B**, 343 (1980).
[136] M. Peter, The Static Quark-Antiquark Potential in QCD to Three Loops, Phys. Rev. Lett. **78**, 602 (1997).
[137] M. Peter, The static potential in QCD: A full two-loop calculation, Nucl. Phys. **B501**, 471 (1997).
[138] Y. Schröder, The static potential in QCD to two loops, Phys. Lett. B **447**, 321 (1999).
[139] A. V. Smirnov, V. A. Smirnov, and M. Steinhauser, Fermionic contributions to the three-loop static potential, Phys. Lett. B **668**, 293 (2008).
[140] C. Anzai, Y. Kiyo, and Y. Sumino, Static QCD Potential at Three-Loop Order, Phys. Rev. Lett. **104**, 112003 (2010).
[141] A. V. Smirnov, V. A. Smirnov, and M. Steinhauser, Three-Loop Static Potential, Phys. Rev. Lett. **104**, 112002 (2010).
[142] R. N. Lee, A. V. Smirnov, V. A. Smirnov, and M. Steinhauser, Analytic three-loop static potential, Phys. Rev. D **94**, 054029 (2016).
[143] N. Brambilla, A. Pineda, J. Soto, and A. Vairo, Effective field theories for heavy quarkonium, Rev. Mod. Phys. **77**, 1423 (2005).
[144] B. A. Kniehl and A. A. Penin, Ultrasoft effects in heavy quarkonium physics, Nucl. Phys. **B563**, 200 (1999).
[145] N. Brambilla, X. Garcia i Tormo, J. Soto, and A. Vairo, The logarithmic contribution to the QCD static energy at N^4LO, Phys. Lett. B **647**, 185 (2007).
[146] K. G. Chetyrkin, J. H. Kühn, and C. Sturm, QCD decoupling at four loops, Nucl. Phys. **B744**, 121 (2006).
[147] Y. Schröder and M. Steinhauser, Four-loop decoupling relations for the strong coupling, J. High Energy Phys. 01 (2006) 051.
[148] D. Eiras and J. Soto, Light fermion finite mass effects in non-relativistic bound states, Phys. Lett. B **491**, 101 (2000).